Schriftenreihe des Energie-Forschungszentrums Niedersachsen

efzn
Energie-Forschungszentrum
Niedersachsen

TU Clausthal

Analysis of the potential, challenges and feasibility of converting an existing underground porous gas storage to hydrogen storage

Christian Truitt Lüddeke
Promotion an der Technischen Universität Clausthal

Band 88

Cuvillier Verlag Göttingen

Schriftenreihe des Energie-Forschungszentrums Niedersachsen (EFZN)
Band 88

Das EFZN ist ein gemeinsames wissenschaftliches Zentrum der Universitäten:

Technische Universität Braunschweig

TU Clausthal

GEORG-AUGUST-UNIVERSITÄT GÖTTINGEN IN PUBLICA COMMODA SEIT 1737

Leibniz Universität Hannover

Carl von Ossietzky Universität Oldenburg

Analysis of the potential, challenges and feasibility of converting an existing underground porous gas storage to hydrogen storage

Doctoral Thesis
(Dissertation)

to be awarded the degree
Doctor of Engineering (Dr.-Ing.)

submitted by

Christian Truitt Lüddeke

approved by the Faculty of Engineering and
Economics at Clausthal University of Technology,

Date of oral examination
July 29, 2026

Impressum

Reihe: Schriftenreihe des Energie-Forschungszentrums Niedersachsen, Bd. 88
Titel des Werkes: Analysis of the potential, challenges and feasibility of converting an existing underground porous gas storage to hydrogen storage
Autor: Christian Truitt Lüddeke

Cuvillier Verlag GmbH
Nonnenstieg 8
37075 Göttingen
Telefon: 0049-551-547240
Webseite: www.cuvillier.de
E-Mail: info@cuvillier.de

Bibliografische Informationen der Deutschen Nationalbibliothek
Die Deutsche Nationalbibliothek verzeichnet diese Publikation in der Deutschen Nationalbibliografie; detaillierte bibliografische Daten sind im Internet über http://dnb.dnb.de abrufbar.

1. Auflage, Göttingen. 2026
Zugl.: Technischen Universität Clausthal, Diss., 2026

Dean	Prof. Dr.-Ing. Armin Lohrengel
Chairperson of the Board of Examiners	Prof. Dr.-Ing. habil. Philip Jaeger
Supervising tutor	Prof. Dr. mont. Leonhard Ganzer
Reviewer	Prof. Dr. Martin Sauter

Tag der mündlichen Prüfung: 29.07.2026

Diese Publikation wurde durch Mittel aus dem Publikationsfonds NiedersachsenOPEN unterstützt, der von zukunft.niedersachsen finanziert wird.

Gedruckt auf umweltfreundlichem, säurefreiem Papier aus nachhaltiger Forstwirtschaft.

ISSN	2943-8276 (Print)
ISSN	3053-8815 (Online)
ISBN	978-3-68952-606-1
eISBN	978-3-68952-607-8
ORCID	0000-0002-9102-0626
ISNI	0000000530796633
DOI	10.61061/ISBN_ 9783689526061

Contents

List of Figures vii
List of Tables viii

Nomenclature **ix**

List of Acronyms **xii**

1 Introduction **1**
1.1 Hydrogen demand and storage capacity 2
1.1.1 Underground Hydrogen Storage 6
1.1.2 Subsurface methanation 9
1.2 Motivation and scope of thesis 9

2 Literature overview and state-of-the-art **13**
2.1 State-of-the-art of subsurface gas storage in Germany 13
2.1.1 Subsurface hydrogen storage potential in the United States 17
2.2 Microbiology in porous subsurface formations 18
2.2.1 Microbial growth and life cycle 20
2.3 Bio-reactive transport process modeling in porous media 26
2.4 Storage and Well Integrity 29
2.4.1 Geological integrity 32
2.4.2 Technical integrity 35

3 Microbial growth experiments coupled with gas chromatographic measurements and numerical modeling **45**
3.1 Microbial species and culture media 45

3.2 Experimental devices and setup 46
3.2.1 Gas-liquid handling system 47
3.2.2 Microchip and holder system 48
3.2.3 Heating and data acquisition system 50
3.2.4 Image acquisition system and processing method 52
3.2.5 Gas analysis system 56
3.3 Experimental procedure 57
3.3.1 Experimental results 59
3.4 Numerical modeling of microbial growth in micromodels 71
3.5 Results and discussion 77
3.5.1 Determination of Representative Elementary Area (Representative elementary area (REA)) . 77
3.5.2 Correlation of experimental and simulation results 80
3.5.3 Calibrated microbial kinetic parameters 87
3.6 Summary 93

4 Examination of existing subsurface natural gas and prospective hydrogen storage capacity and productivity 96
4.1 Aspects to consider during a conversion 96
4.2 Gas characteristics 96
4.2.1 Subsurface working gas volume calculations . 104
4.2.2 Deliverability and withdrawal performance . 106
4.3 Static model description and storage pressure calculations 111
4.4 Results and discussion 117

4.4.1 Storage capacities between an existing UGS compared to a prospective UHS 117
4.4.2 Natural gas and hydrogen deliverability . . . 119
4.5 Conclusions 138

5 Simulation of the conversion of an existing UGS to a prospective UHS 141
5.1 Simulation approach 142
5.1.1 Development of subsurface storage conversion schedule 144
5.2 Results and discussion 147
5.2.1 Conversion and a one-year storage operation without microbial activity 148
5.2.2 Conversion and a one-year storage operation considering biochemical reactions 152
5.2.3 Volumetric comparison of the two storage cases 156
5.2.4 Impact of microbial kinetic parameters 159
5.3 Summary 161

6 Conclusion 164

Appendix 191

List of Figures

1.1 Hydrogen demand in the European Union in 2050 [35] 3
1.2 Projected hydrogen energy stored capacity in 2030 in the European Union [99] (the pie chart values indicate every subsurface storage type's relative percentage in each country) 5

2.1 Underground gas storage sites in Germany [59] 15
2.2 Microbial growth behavior in its various phases ([39, 72]) 21
2.3 Potential gas leakage pathways from a storage rock (adapted from Katz and Lee (1990) [54]) 30
2.4 Possible leakage pathways for gas from the storage rock into the well or into overlying formations (plugged well) [47, 87] 36
2.5 Double barrier system of an operating underground gas storage well in porous media (adapted from [13]) 38

3.1 Experimental microfluidic setup 47
3.2 Schematic structure of the linear circle micromodel used 50
3.3 Image processing method developed within MATLAB 54
3.4 Visual depiction of the measured gas components and their concentrations in the micro gas chromatograph 57
3.5 Microbial values and methane measured in the gas chromatograph 61

3.6 Microbial number and methane concentration over time at 40 °C 63
3.7 Microbial cell number and methane development at standard temperature 66
3.8 Methane concentration development at 62 °C 67
3.9 Numerical model of the linear circle microchip during the injection of the gas mixture (elements displaying the porosity ϕ) 72
3.10 Representative elementary area of the microchip . . . 78
3.11 Areas of investigation (green rectangles) examined, each with the size of the representative elementary area 79
3.12 Matched experimental and numerical development of the microbial cell count and the methane production 81
3.13 Matched experimental and numerical development of the microbial cell count and the methane production (40 °C) 83
3.14 Matched experimental and numerical development of the microbial cell count and the methane measured (25 °C) 85
3.15 Matched experimental and numerical development of the microbial cell values and the methane production (62 °C) 86

4.1 Curves of the compressibility factors for both methane and hydrogen (T = 65°C (338.15 K)) 101
4.2 Development of viscosity and density for hydrogen and natural gas as pressure changes (T = 65°C (338.15 K)) 103

4.3 Curves of the compressibility factors for both methane and hydrogen at p_{min} = 80 bar and p_{max} = 160 bar (T=65°C (338.15 K)) 106
4.4 Storage deliverability profile of an exemplary subsurface gas storage site (adapted from Plaat, 2009 [84]) 109
4.5 Overview of the porous storage layer (indicated permeability in x direction) 114
4.6 Locations of the storage wells (top view) 115
4.7 Comparison of stored working gas volumes and respective energy content (adapted after Lüddeke et al. (2026) [68]) 118
4.8 Storage deliverability of natural gas and hydrogen and produced cumulative working gas volume over time [68] 120
4.9 Fraction of produced working gas volumes for hydrogen and natural gas [68] 121
4.10 Pressure development during the seasonal production process for both storage cases 123
4.11 Sensitivity analyses of different storage pressures on the withdrawal rates [68] 124
4.12 Sensitivity analyses of different bottom-hole pressures on the withdrawal rates [68] 127
4.13 Influence of skin (2) on the flow rates [68] 129
4.14 Production curves of the pseudo gas at altered gas characteristics [68] 132

5.1 Operational rates spanning one year (injection = 100% hydrogen, production = stored gas) 146

5.2 11-year schedule (Ten-year replacement and one subsequent storage cycle) 147
5.3 Distribution of hydrogen and methane fractions after completion of the schedule 148
5.4 H_2 and CH_4 flux development 150
5.5 Produced gas stream composition 150
5.6 Composition of the stored gas 151
5.7 Distribution of hydrogen and methane fractions after completion of the schedule 153
5.8 Microbial density at its peak value and after 11 years 154
5.9 Hydrogen consumption rate and microbial density during the conversion schedule 155
5.10 Ten-year replacement schedule considering the presence and the absence of microbial reactions 157
5.11 One-year subsurface operation cycle 158

A.1 Setup of the heating device, the used components and the used component-computer communication ports (COM) 192
A.2 Digital interface of the LabView control panel to insert and control temperature, observe dynamic parameters and to record them into a specific file 193

List of Tables

2.1 Screening criteria to select a suitable subsurface hydrogen storage site based on findings by HyStories . 43

3.1 Numerically initialized parameters 73
3.2 Matched modeled parameters for the best replication with the experimental results 88

4.1 Gaseous characteristics between hydrogen and methane 98
4.2 Storage site model geological parameters 112
4.3 Initial states of the site for each storage case 113
4.4 Final flow rates in Sm^3/h in a natural gas and a hydrogen scenario at various storage pressures 125
4.5 Cumulative withdrawn volumes in $10^9\ \mathrm{Sm}^3$ in a natural gas and a hydrogen scenario at various storage pressures 126
4.6 Final flow rates in Sm^3/h at various bottom-hole flowing pressures 128
4.7 Cumulative withdrawn volumes in $10^9\ \mathrm{Sm}^3$ at various bottom-hole flowing pressures 128

Nomenclature

Greek Symbols

Symbol	Description	Dimensions	Units
α	half-saturation constant	-	-
Γ	boundary	-	-
γ	stoichiometric relationship	-	-
λ	mobility	$M^{-1}*L^{3}*T$	$1/Pa*s$
μl	microliter	L^{3}	10^{-6} L
ϕ	porosity	-	-
Ψ^{decay}	microbial decay term	T^{-1}	$1/s$
Ψ^{growth}	microbial growth term	T^{-1}	$1/s$
$\Psi^{\text{growth}}_{\text{max}}$	microbial maximum growth rate	T^{-1}	$1/s$
ρ_{m}	molar density	$N*L^{-3}$	$\frac{\text{mole}}{\text{m}^3}$
ρ	density	$M*L^{-3}$	$\frac{\text{kg}}{\text{m}^3}$
φ	fugacity coefficient	-	-
μ	viscosity	$M*L^{-1}*T^{-1}$	Pa*s

Roman Symbols

Symbol	Description	Dimensions	Units
V_{m}	molar volume	$L^{3}*N^{-1}$	$\frac{\text{m}^3}{\text{mol}}$
V_{WG}	working gas volume	L^{3}	m^{3}
C^{im}	immobile microbial concentration	-	-

C^{mm}	mobile microbial concentration	-	-
p_e	reservoir pressure	$M*L^{-1}*T^{-2}$	bar, Pa
p_{wf}	well flowing pressure	$M*L^{-1}*T^{-2}$	bar, Pa
A	area	L^2	m^2
b	decay rate	T^{-1}	$\frac{1}{s}$
c	concentration	-	-
D	diffusion/dispersion	L^2*T^{-1}	$\frac{m^2}{s}$
e	dry-out coefficient	T^{-1}	$\frac{1}{s}$
f	dry-out term	T^{-1}	$\frac{1}{s}$
h	height	L	m
j	gas or liquid phase	-	-
k	permeability	L^2	m^2, Darcy
L	limit	-	-
m	maintenance rate	T^{-1}	$\frac{1}{s}$
n	microbial cell number	-	1
q	flux	L^3*T^{-1},N^1*T^{-1}	$\frac{mol}{s}$
R	universal gas constant	$M^1*L^2*T^{-2}*K^{-1}*N^{-1}$	$\frac{J}{mol*K}$
r	radius	L^1	m
S	saturation	-	-
s	skin	-	-
T	temperature	K	K
TG	total gas	L^3	m^3
V	volume	L^3	m^3

Y	yield	-	-
z	compressibility factor	–	–

List of Acronyms

AOI	area of investigation
CH_4	methane
CO_2	carbon dioxide
EoS	Equation of State
GWh	Gigawatthours
H_2	hydrogen
ID	inner diameter
ITO	indium tin oxide
MPa	Megapascal
Mt	million tonnes
NG	natural gas
OD	outer diameter
PR	Peng-Robinson

REA	representative elementary area
TWh	Terrawatthours
UHS	underground hydrogen storage
UMR	underground methanation reactor

Abstract

The energy transition is a long-term strategy aimed at developing renewable energy sources, especially wind and solar power, and achieving carbon neutrality by 2045. As these renewable energies are heavily dependent on weather and climate conditions, the production of electricity might follow different patterns than the energy demand. To balance these fluctuations and ensure sufficient available energy, large-scale energy storage facilities are necessary. Converting existing porous storage sites to hydrogen is a viable option to achieve this goal. The conversion to a future underground hydrogen storage (UHS) site is associated with many challenges, which require a fundamental analysis to facilitate the development of hydrogen storage in the porous subsurface. Understanding the prospective extraction behavior of hydrogen from the subsurface and determining its total storage volume and capacity under the influence of various pressure conditions is a vital aspect to be examined, as well as the influence of biochemical reactions induced by microorganisms.

One of the critical uncertainties is the potential microbial activity in the presence of H_2 and CO_2. Microbial growth experiments using methanogenic archaea in a H_2-CO_2 environment inside a quasi-two-dimensional micromodel was studied. The observation of the microbial number and the methane production over time was conducted at three different temperatures. The Double-Monod model describing the microbial growth patterns was extended by a space-limiting factor, which considered the limited pore space available for microbial growth. To obtain the kinetic growth parameters, a

numerical model replicating the laboratory micromodel was created in DuMu^X and a history matching procedure was carried out by adapting the maximum growth, maintenance, decay rates and the yield.

Using a field-scale subsurface porous storage model, two hypothetical storage cases (natural gas and hydrogen) were modeled and a gas withdrawal procedure was simulated. To assess the influence of individual gas characteristics, a pseudo gas was developed with the initial properties of natural gas. Individually, the compressibility factor, the molar mass and the viscosity were switched to the hydrogen values and the development of the flow rates was compared. The influence of different storage and bottom-hole flowing pressures and skin factors were also modeled and analyzed. Additionally, a long-term energy demand pattern based on a carbon-neutral scenario was developed and implemented in DuMu^X to model a 10-year conversion period with a subsequent one-year hydrogen storage cycle. This was carried out for an abiotic and for a biochemically active storage case.

The combination of visual microbial observation and the gas chromatographic measurements of methane provides a useful tool to connect the microbial cell value and methane produced. The temperature has an evident influence on the kinetic parameters and on the methane peak value. The numerical model, extended by the space-limiting factor, provides an acceptable match with the experimental results. Examining the storage capacities and deliverabilities, a hydrogen-containing porous media has a significantly smaller energy content compared to natural gas. In addition, the deliverability of hydrogen begins decreasing much earlier than nat-

ural gas and this storage volume is depleted much quicker. The large-scale influence of microbes on a hydrogen storage scenario leads to a small fraction of hydrogen being converted to methane, with the highest conversion rate at the beginning of hydrogen injection. However, no significant negative long-term impact can be derived from the microbial activity.

The aim of my work was to investigate the key challenges associated with hydrogen storage, focusing on storage capacity, withdrawal behavior and biochemical processes in the porous subsurface. Hydrogen has lower storage volumes in the subsurface, leading to a reduced stored energy content. The extraction of hydrogen occurs more rapidly and depletes the storage site quicker compared to natural gas. The microbial analysis reveals that temperature influences the methanogenic cell growth and hydrogen consumption, but they have a very marginal impact on the hydrogen quantity. In the long run, microbial effects do not profoundly alter the gas composition, and do not impede the development of subsurface porous hydrogen storage. My research supports the notion that subsurface hydrogen storage has a strong potential as an important future energy storage option.

Zusammenfassung

Die Energiewende, bei der insbesondere die Entwicklung von Solar- und Windenergie vorangetrieben wird, soll langfristig zur Klimaneutralität bis 2045 beitragen. Da diese erneuerbaren Energien maßgeblich von Wetter- und Umweltbedingungen beeinflusst werden, kann die Erzeugung von erneuerbarem Strom nicht immer zeitgleich den voraussichtlichen Strombedarf decken. Um diese Schwankungen auszugleichen und um eine zuverlässige Verfügbarkeit von Energie zu gewährleisten sind große Speichermöglichkeiten notwendig. Die Umwidmung bestehender poröser Untertagespeicher zu Wasserstoffspeicher ist hierzu eine vielversprechende Möglichkeit. Die Umwidmung ist mit vielen Herausforderungen verbunden, die eine detaillierte Untersuchung notwendig machen, um einen Wasserstoffspeicher zu errichten. Das voraussichtliche Entnahmeverhalten von H_2 aus dem porösen Speicher und die potenzielle Speicherkapazität sind neben den mikrobiellen Prozessen, die in einer Wasserstoffumgebung stattfinden können, wichtige Kriterien, die für eine erfolgreiche H_2-Speicherung unerlässlich sind.

Ein entsprechender wichtiger Aspekt sind potenzielle mikrobiologische Aktivitäten im Untergrund im Beisein von H_2-CO_2. Mikrobielle Wachstumsexperimente an methanogenen Archaeen und einem Gemisch aus H_2 und CO_2 wurden in einem quasi zwei dimensionalen Mikromodell durchgeführt. Dabei wurden im Verlauf die mikrobielle Anzahl und die Produktion von Methan bei drei unterschiedlichen Temperaturen untersucht. Das Double-Monod Modell, welches das mikrobielle Wachstumsverhalten beschreibt, wurde

mit einem Raumbegrenzungsfaktor erweitert, um das begrenzte Volumen zu berücksichtigen. Ein numerisches Modell, welches die Laborversuche nachstellt, wurde in DuMu^X erstellt, um Mithilfe eines History-Matching-Verfahrens die kinetischen Parameter zu Wachstums-, Maintenance-, Sterberate und Yield zu ermitteln.

Mithilfe eines untertägigen porösen Feldmodells wurden zwei Speicherszenarien (Erdgas und Wasserstoff) abgebildet und jeweils ein Entnahmeprozess simuliert. Um den Einfluss einzelner Gasparameter genauer zu analysieren, wurde ein Pseudo-Gas definiert, welches zunächst alle Gaseigenschaften von Methan hat. Mit jeder weiteren Simulation wurden einzeln die Parameter Kompressibilitätsfaktor, molare Masse und Viskosität zu den Werten von Wasserstoff gewechselt und der Einfluss auf die Entnahmeraten wurde verglichen. Verschiedene Fließdrücke und Skin-Werte wurden mit berücksichtigt. Ein langfristiges Speicherszenario, basierend auf einer jährlichen Energiebedarfskurve, wurde in DuMu^X eingepflegt und in einem Umwidmungszeitraum von 10 Jahren mit einem anschließenden einjährigen Speicherzyklus simuliert. Dies geschah für einen abiotischen Speicher und einem Speicher mit mikrobieller Aktivität.

Die zeitgleiche visuelle Observation der mikrobiellen Dichte mit der Messung der Gaszusammensetzung ist eine sehr nützliche Methode, um die mikrobielle Anzahl mit dem produzierten Methan zu koppeln. Die Wachstumsparameter und das produzierte Methan sind von der Temperatur abhängig. Das numerische Modell, welches mit einem Raumbegrenzungsfaktor erweitert wurde, erzielt einen guten Abgleich mit den experimentellen Versuchen. Beim Vergleich der Speicherkapazitäten und Entnahmeraten zeigt sich, dass

ein Wasserstoffspeicher eine geringere Energiemenge hat als ein Erdgasspeicher. Zusätzlich nimmt die H_2-Entnahmerate ab und der Speicher wird in kürzerer Zeit entleert. Der mikrobielle Einfluss auf einer großen Skala führt zu einem geringen Anteil an umgesetztem H_2, mit der größten Umsetzungsrate zu Beginn der H_2-Einspeisung. Langfristig ist kein großflächiger, negativer, mikrobieller Einfluss auf einen H_2-Speicher zu erwarten.

Die durchgeführten Arbeiten gewährten einen Einblick in die Speicherkapazitäten von Wasserstoff, den Produktionsraten und den biochemischen Reaktionen zwischen Wasserstoff und Mikroben im porösen Untergrund. Wasserstoff weist ein geringeres Speichervolumen auf, welches zu einer geringeren Speicherkapazität führt. Die Entnahme von Wasserstoff führt zu einer schnelleren Entleerung des Speichers im Vergleich zu Erdgas. Die mikrobiellen Analysen zeigen, dass Zellenwachstum und Wasserstoffverbrauch von der Temperatur beeinflusst werden, dies geschieht und bleibt auf einem relativ niedrigen Niveau und das wirkt sich minimal auf den Wasserstoff aus. Langfristig ist keine tiefgreifende Veränderung der Gaszusammensetzung zu erwarten und dies beeinträchtigt nicht die Entwicklung von untertägigen, porösen Wasserstoffspeichern. Die durchgeführten Untersuchungen unterstützen die Vorstellung, dass die untertägige Wasserstoffspeicherung ein großes Potenzial als Energiespeicher aufweist.

Acknowledgement

I would like to thank Prof. Dr. Leonhard Ganzer for giving me the unique opportunity to pursue my PhD at the Institute of Subsurface Energy Systems at Clausthal University of Technology and for his continuous, valuable support during my scientific work. I would also like to thank Prof. Dr. Martin Sauter for reviewing my work, providing insightful feedback and for the collaboration in the research project TEN.efzn.
I want to thank Dr.-Ing. Birger Hagemann for his important guidance and the close cooperation throughout the years.
My thanks also goes out to Prof. Michael Hou and the many talks we have had on hydrogen, conventional energies and the energy future.
I am very grateful to my parents and to my family, who unwaveringly stood by me. I am very grateful to my best friend, Hedye Mobaraki, who permanently encourages me to keep striving, and whose deep and warm friendship has shaped me.
I would also like to thank Dr.-Ing. Sebastian Hogeweg, Dr.-Ing Julia Michelsen and Dr.-Ing. Calvin Gaol for the outstanding collaboration and many discussions during the times working together on hydrogen and sharing many memories. I also want to thank Michael Luczak and Manfred Stövesand for their help in developing and constructing the experimental setup which I used for the laboratory experiments and for giving valuable feedback on experimental procedures and equipment. My gratitude also goes to all current, former and retired colleagues in the entire ITE with whom I have worked together and to all my friends around the globe.

Chapter 1

Introduction

In recent years, climate change has become a topic of growing public interest. Many new policies and multilateral agreements have been implemented to reduce the reliance on fossil fuels and to promote the development and use of renewable energy sources. Many countries have established frameworks and guidelines based on the agreements to enable a transition to sustainable sources. The Paris Climate Accord from 2015 set a target to limit the global increase in temperature to 1.5 °C above the levels from the pre-industrial era [76].

The development of renewable energies is primarily focused on the expansion of capacities of solar and wind power, followed by hydropower and nuclear power. The total global solar power is estimated to be approximately 35 PJ, and wind will be nearly 20 PJ by 2050 in the Net-Zero-Emissions scenarios, according to the IEA's World Energy Outlook [49]. A serious drawback of renewable energy sources is their dependency on weather conditions, with a high electricity generation expected during the summer and windy days. This can lead to imbalances between the produced quantities and the actual energy demand. To bridge these gaps and ensure a sufficient amount of energy supply, large-scale energy storage opportunities are necessary. The surplus renewable energy can be converted to other energy carriers, such as hydrogen and ammonia. These products are part of the Power-To-X conversion process, where the X denotes the target energy that is generated.

Hydrogen is gaining significant attention as a chemical energy carrier. The federal government has emphasized its importance in the National Hydrogen Strategy. It is considered a substantial pillar to achieve carbon neutrality by 2045 and also regarded as an energy carrier that can be used to generate electricity or it is immediately used in industrial processes [4, 28, 74]. In 2021, the world demand for hydrogen (H_2) stood at nearly 94 million tonnes (Mt) [48]. The demand forecast for clean hydrogen is dependent on national efforts and technologies to achieve carbon neutrality. When net-zero emissions are to be achieved globally by 2050 and the global increase in temperature is to be kept below 1.8 °C, the annual demand for clean hydrogen can range between 585 and nearly 620 Mt per year by 2050 [34, 86].

1.1 Hydrogen demand and storage capacity

The Federal Government and National Hydrogen Council in Germany estimate the domestic demand to range between 56 to 110 Terrawatthours (TWh) by 2030 [75, 103], with the current hydrogen consumption at around 55 TWh. Other studies have calculated similar values concerning the hydrogen demand in the coming years. A recent study by the BDI conducted in 2021 determined the needed hydrogen to be approximately 240 TWh for all industrial and social sectors (industry, housing, traffic, agriculture) in Germany by 2045 [11]. Another analysis, the EU-funded HyUsPRe project, concluded that the demand in Germany could reach even 1000 TWh by 2050 [35, 37]. Further studies have calculated that the total hydrogen demand in Germany in all examined sectors and industries might

range between 250 to 280 TWh by 2050 [57]. Since the European Commission has recognized hydrogen as an essential component of the Green New Deal to reduce emissions in the Member States, much investigation has been directed towards assessing the subsurface storage potential of hydrogen across the continent. The estimated increase in hydrogen demand could reach $4000\,\mathrm{TWh}$ in Europe by 2050. Regional demands vary significantly (c.f. Figure 1.1).

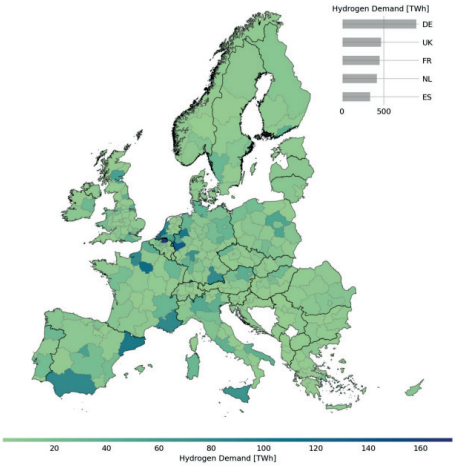

Figure 1.1: Hydrogen demand in the European Union in 2050 [35]

Most of the expected hydrogen demand is projected to be in Central and Western Europe, with the highest local demands forecasted to be in industrial and densely populated areas. Therefore, efficient and large-scale energy storage opportunities are necessary. For many decades, natural gas has been stored in subsurface facilities in times of low demand and was extracted in the colder winter season.

Using those existing facilities is a viable option to store hydrogen in the long run. The most common subsurface storage options are:

- Salt caverns: These are mined or leached large hollow spaces in embedded salt formations, surrounded by a nearly-impermeable salt layer. Due to the vast hollow spaces, salt caverns can operate at a high performance, with short-term high deliverability rates designed to meet temporary peak demands. Salt caverns can also operate at numerous cycles per year and are usually assembled in aggregations of numerous caverns in a field [101].
- Porous formations: The most common subsurface porous storage sites are former hydrocarbon reservoirs. These formations have extensive natural geology and proven structural trapping mechanisms, ensured by the overlying sealing caprock. The stored gas medium is kept inside the porous media and is prevented from migrating into shallower formations. Compared to salt caverns, porous media have larger sizes, which can store a larger volumetric amount of gas. Porous storages have low flow velocities and reduced deliverabilities, making them suitable to meet stable basic demands [101].

Recent studies have estimated the total working gas capacity of hydrogen in existing storage sites to be approximately $260\,\mathrm{TWh}$ across the member states in 2030, assuming all available existing storage facilities are converted. Including non-member EU states, this value is at $349\,\mathrm{TWh}$ (Figure 1.2). The anticipated high storage demand underscores the necessity to use existing storage sites for future hydrogen storage operations.

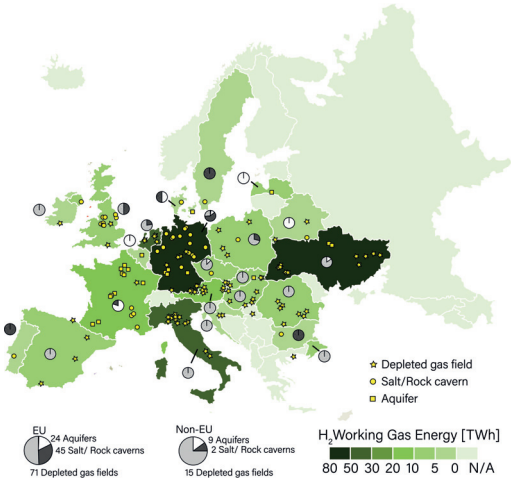

Figure 1.2: Projected hydrogen energy stored capacity in 2030 in the European Union [99] (the pie chart values indicate every subsurface storage type's relative percentage in each country)

Existing porous storage sites (depleted gas or oil reservoirs) possess the largest capacities to store hydrogen, followed by salt or rock caverns. Another type of porous storage site, aquifers, are also considered potential hydrogen storage sites and these could store nearly one-fifth of the entire capacity. The storage sites are distributed all across the European Union, with Germany having the largest hydrogen energy storage capacity (nearly 71 TWh), assuming that all existing storage sites are converted. This value was obtained by using available storage data from public institutions and hydrogen properties (geometrical volume and the density of hydrogen). Another assumption was that the energy of hydrogen is one-quarter of methane and that Germany has nearly one-third of

the EU storage capacities [99].

1.1.1. Underground Hydrogen Storage

A result of the increasing necessity to develop long-term storage opportunities for hydrogen in the subsurface is a large number of projects investigating the feasibility of injecting hydrogen into and withdrawing it from the subsurface. Apart from the benefits, which include the use of already existing surface and subsurface facilities and the leveraging of available infrastructure, many challenges facing underground hydrogen storage (UHS) continue to be analyzed. These include integrity issues, geochemical or biochemical reactions or the mixing processes of various gases. This review of past subsurface hydrogen storage tests focuses primarily on the storage of hydrogen in porous formations. The first experience with the injection of hydrogen into the subsurface were gained during the storage of town gas in Ketzin (Germany), Lobodice (Czech Republic) and Beynes (France), beginning in the 1960-ies. Town gas was a gaseous mixture containing H_2, CH_4, CO_2 and nitrogen which was injected into an aquifer for temporary storage. Laboratory analyses have revealed a decrease in the hydrogen and an increase in the methane concentration during the storage period. These changes in the gas composition were attributed to microbial reactions, induced by methanogenic archaea [102]. These microbes consume hydrogen and carbon dioxide to produce methane and water [12, 71].

In the 1970-ies, the first underground hydrogen storage projects were designed and put into operation. In Europe, the first subsurface hydrogen storage test began in Teesside, UK, in 1972 in salt caverns and is still operational with a total storage capacity of

nearly 19 t. Larger storage sites (Clemens Terminal) were developed in Texas in 1983 [50]. In the past 10 to 15 years, a large number of research projects focused their investigation on the analysis and feasibility of future hydrogen storage in porous media. A large number of EU consortium projects tackled issues, such as geochemical, microbial risks and deliverability challenges, to improve characterization and developing risk mitigation measures. In the EU projects HyUSPRe (2021-2024) and HyStories (2021-2023), the geochemistry, microbiology and various mixing processes between two gases were analyzed in laboratory experiments. The obtained results were tuned and upscaled to field-scale models to simulate large-scale underground hydrogen storage scenarios. The results improved understanding of the potential challenges and risks associated with hydrogen storage. They also mapped the expected demand, storage capacities, and the forecasted levelized costs of hydrogen storage [14]. Additionally, the geological characteristics of existing gas storage sites were used to draft recommendations that assist in assessing the feasibility of an existing site as a hydrogen storage facility [8].

Another pilot field scale test in a porous formation to store hydrogen was performed in Argentina as part of the company HyChico. Hydrogen was injected with natural gas into a sandstone porous media, shut in for three months and then the gas was withdrawn. The objectives were to analyze the reservoir behavior containing hydrogen and to observe the integrity of the overlying caprock. A subsequent pilot test was designed to analyze methanation processes in the same storage constellation [83].

A field trial in a porous reservoir began in 2013 in Austria as a part in the project Underground Sun Storage until 2017. This project consisted of numerous working packages, which included examining the flow behavior of hydrogen and methane in storage rock samples, the microbial characterization of the formation water, analyzing material integrity in the presence of hydrogen and conducting field trials by injecting 10% of hydrogen in a total volume of $1.22 \times 10^6\,\mathrm{Sm}^3$ into the porous storage site. After a shut-in period of three months, the withdrawn gas composition revealed that 82% of hydrogen was withdrawn and the rest remained in the subsurface. No compromise of the storage site was detected [3]. A follow-up project (Underground Sun Storage 2030) concluded that large-scale subsurface hydrogen storage was feasible on a commercial basis [42].

Extensive investigation of technical and geological integrity of subsurface storage sites has also been carried out. In the project HyInteger (2016-2019), the implications of hydrogen and other gas mixtures in the porous subsurface on existing well cement sheaths at reservoir conditions were analyzed in laboratory experiments. The flow of gas through the porous media and the integrity of the structure in the presence of hydrogen in the long-run was evaluated and used for cyclic hydrogen storage simulations [31]. Hydrogen diffusion experiments on pure porous storage rock samples and caprock layers have been performed between 2021-2025 to assess the geological integrity of a storage site to contain hydrogen. The results of the experiments were processed to develop a numerical simulation model to replicate the laboratory works and to predict

the reservoir sealability [40]. These diffusion experiments have been extended in a follow-up project (TEN.efzn), which investigates hydrogen diffusion processes through intermediate rock layers consisting of multiple stratigraphic formations [30].

1.1.2. Subsurface methanation

Microbial species, such as methanogenic archaea, by consuming hydrogen and carbon dioxide and producing methane and water (ratio H_2:CH_4 4:1), post one of the most significant challenges to UHS in porous media [38, 102]. Microbes live in the aqueous phase inside the storage site, and accelerate their metabolism when they come into contact with hydrogen and carbon dioxide. According to the Sabatier reaction, hydrogen and carbon dioxide are consumed and methane is produced, which indicates a decrease in hydrogen. In a pure UHS scenario, this would be a disadvantage to the storage efficiency. If the purpose is to develop an underground methanation reactor (UMR), this microbial conversion process forms the basis for this concept. This idea was introduced by Strobel et al. (2020), in which the conversion of hydrogen to methane is intentional, and has a volumetric energy content nearly three times larger than hydrogen. The deliberate methane production results in a higher energy content and provides an important contribution in the energy transition [96].

1.2 Motivation and scope of thesis

The need for large-scale energy storage opportunities to have a sufficient supply available during times of low production of renewable

electricity is obvious. So far, the storage of hydrogen in salt caverns has been extensively assessed and investigated. Associated projects have reached a high maturity level with field-scale pilot tests underway in Northern Germany. For instance, a salt cavern in the region Etzel has been filled with $1 \times 10^6\,\mathrm{Sm}^3$ of hydrogen [27]. Another field test is ongoing at the storage site Krummhörn, where a new cavern was leached and filled with $500.000\,\mathrm{Sm}^3$ of hydrogen. Extensive investigations on material compatibility and geological and technical integrity towards H_2 have been successfully performed [43]. In recent years, the utilization of subsurface porous storage sites to achieve this objective has received increased attention. Their large storage capacities, their contribution to the energy base load, their availability and gas storage operational history load make them suitable candidates for large-scale hydrogen storage. Past projects have focused on analyzing the total available capacity and the potential biochemical and geochemical challenges. Different well patterns designed for the cyclic operation have been analyzed in simulations to obtain an optimal well placement strategy to maximize the full-scale deliverability of a storage site. Further analysis also used available existing natural gas withdrawal data to predict the potential hydrogen withdrawal rates from an identical storage site through nodal analysis [52]. However, a big gap remains between the effects of individual gas properties on the withdrawal rates for natural gas and hydrogen. The extent to which gas properties could influence the magnitude of a withdrawal value and its duration also remains unclear. Considering biochemical processes, different microbial development models have been formulated in literature and simulated at large field scales. Replicating microbial cell growth behavior was conducted either in batch experiments

through pressure measurements or through the visual computation of the microbial number in pore-scale images [97, 98]. A precise experimental quantification of produced methane by methanogenesis has not yet been performed and would provide essential input to the quantitative impact of biochemical processes.

The mentioned challenges and uncertainties are predominantly tied to hydrogen inside porous media. For this reason, the work performed in this thesis focuses on hydrogen storage in subsurface porous formations. To address these uncertainties, the following work was conducted, which is described in the following chapters of this thesis:

- Chapter 2 provides a literature overview of the most relevant characteristics affecting the integrity of underground gas storage sites in porous media and the challenges that are faced when hydrogen is to be stored. In addition, circumstances affecting subsurface extraction processes and biochemical reactions in porous media in the presence of hydrogen are presented. These aspects are highlighted using performed and ongoing investigations into the microbial reactions in laboratory experiments, at a field scale and the impact on storage efficiency.
- In Chapter 3, microbial experiments using methanogenic archaea and a gaseous hydrogen-carbon dioxide mixture (80%-20%) in a quasi-two-dimensional micromodel are conducted at various temperatures (25, 40 and 62°C). The analysis of the microbial number and gas measurements over time are performed simultaneously. In the open-source numerical sim-

ulator DuMu^{X}, a numerical model is developed to replicate the micromodel experiments. History matching is performed to obtain microbial kinetic parameters.

- In Chapter 4, a hypothetical storage model is used to analyze gas withdrawal performance of hydrogen and natural gas. To analyze the effect of individual properties on the respective withdrawal performance, a pseudo gas is initialized with methane properties. To analyze the effect of individual characteristics, the respective property is replaced by the hydrogen equivalent. The rate development of this pseudo gas is compared to the pure hydrogen and natural gas rate development and the effects of each property on the withdrawal rates are analyzed. Using this method, the influence of the compressibility factor, molar mass and viscosity are analyzed.
- In Chapter 5, a field-scale analysis is undertaken on the grid from Chapter 4 to simulate a gas replacement process and storage cycle based on a predefined schedule (a ten-year replacement period and a full one-year storage cycle). Two scenarios are considered: the first one assumes no biochemical reactions and the second one assumes microbial reactions based on parameters obtained from the micromodel experiments. The development of the hydrogen and methane energy content in both cases is compared.
- Chapter 6 summarizes the conclusions of the conducted work and the takeaways.

Chapter 2

Literature overview and state-of-the-art

The possibility to store gas in a porous subsurface is a significant contribution to long-term energy supply security. As the focus shifts towards hydrogen, its flow in porous rocks is being closely investigated to gain a better understanding of the flow patterns. If hydrogen had previously not been injected into an operational subsurface gas storage site, it will interact with gases and liquids present in the porous space, thus increasing the necessity to evaluate interactions between the hydrogen and residual components. This is particularly important as existing porous storage sites are being considered to store hydrogen in the long run. Apart from the flow and mixing behavior, hydrogen can also induce microbiological reactions. This chapter provides a review of the multiphase hydrodynamics, microbiological reactions with hydrogen in the porous subsurface and the various aspects of geological and technical integrity that need to be examined to assess the suitability of an existing storage facility to store hydrogen.

2.1 State-of-the-art of subsurface gas storage in Germany

Germany has a large number of different underground storage sites, which are currently storing natural gas. There are 43 underground storage locations, out of which 14 are subsurface porous reservoirs, and 29 are cavern locations. Most cavern storage locations consist

of multiple single caverns, totaling 269 single caverns. Most of the porous storage formations are depleted gas reservoirs, which initially produced natural gas before being repurposed for subsurface gas storage. The following Figure 2.1 shows the location of the storage sites in Germany in 2024.

Porous storage sites are the dominant storage formations in the south and salt caverns are dominant in the north of the country (Figure 2.1). The current total working gas volume for natural gas is nearly $23 \cdot 10^9\ \mathrm{Sm}^3$, equivalent to nearly 253 TWh. Lower Saxony has the most subsurface storage sites, including both caverns and porous media. Europe's largest porous storage site, Rehden, is also located in Lower Saxony, with a working gas volume of nearly $4 \times 10^9\ \mathrm{Sm}^3$. Most caverns are also located close to the coast in the north. In the state of Saxony-Anhalt, there is a combined storage site, operating caverns and one pore storage site (Bad Lauchstädt). Less caverns are available in the south. Simultaneously, the number of porous storages increases. The largest number of pore storage sites is in the states of Baden-Württemberg and Bavaria, with a smaller stored volume than in the storage sites in the north.

The use of these existing storage possibilities has been in the spotlight when large-scale hydrogen storage opportunities are considered. Initially, the examination of hydrogen storage feasibility was performed with salt caverns. Uniper, a German energy storage and provider, began a field test at the cavern storage site Krummhörn. In this field operation, a new cavern with a geometrical volume of $3000\,\mathrm{Sm}^3$, capable of storing up to 1.8 Gigawatthours (GWh) of hydrogen, was leached. The goals were to test the storage feasibility containing $100\,\%$ of hydrogen, analyze the material integrity,

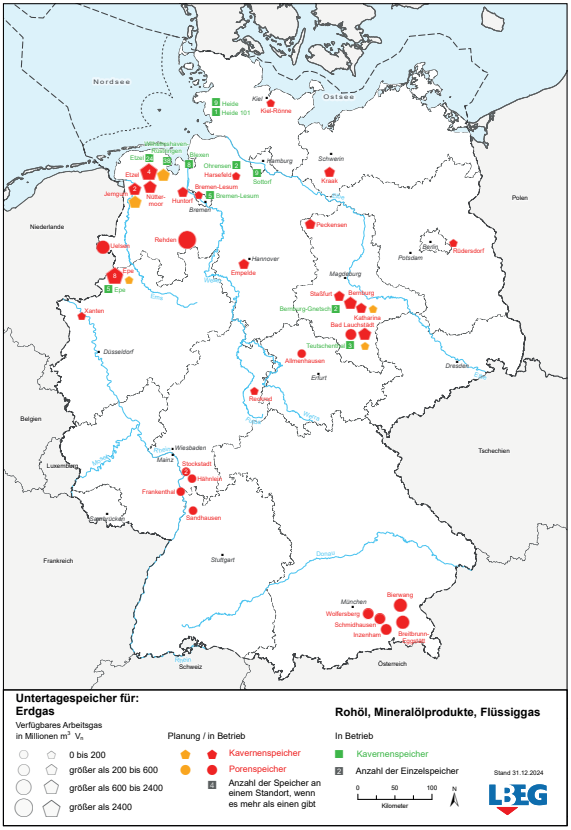

Anlage 12: Übersichtskarte der Untertagespeicher für Erdgas, Rohöl, Mineralölprodukte und Flüssiggas.

Figure 2.1: Underground gas storage sites in Germany [59]

compatibility towards hydrogen and certify repurposed pipelines to transport pure hydrogen. The most recent state of the project is the installation of surface equipment in preparation for the official storage test [43]. A similar operation is being conducted at the salt cavern in Etzel. This salt cavern is being repurposed to store pure hydrogen, using the available technologies and equipment. Its location at a vital transition point for natural gas is also being investigated how the connecting pipeline network can be integrated into an international hydrogen economy at the North Sea coast [27].

The examination of hydrogen storage in subsurface porous storage sites has only gained traction in recent years. The completion of the Underground Sun Conversion and the Underground Sun Storage projects marked a significant milestone in this area [3, 42]. In 2022, hydrogen admixed to natural gas in fractions of 5, 10 and 20 % started being injected into an existing porous storage site in Bavaria, Germany. After a shut-in period of three months, the stored gas was produced and gas chromatographic measurements were conducted. The results are integrated in a reservoir simulation model to assist in predicting future UHS operations [46].

The total subsurface storage potential of hydrogen is divided into the respective quantities that can be stored in salt caverns and in porous media in Germany. In these assumptions, depleted gas fields currently operating as natural gas storage are the considered porous formations. By 2050, 31 existing salt caverns and 4 pore storage sites are considered feasible to store hydrogen, totaling nearly 32 TWh storage capacity. Additional 40 salt caverns would need to be commissioned to increase the total storage capacity to the expected 71 to 73 TWh. In this scenario, the pore storage sites would account

for just 2 TWh of H_2 storage capacity [10]. If all operating pore storages and salt caverns were converted, this available storage potential would be approximately 50 TWh. The storage potential of pore storages varies between 2 and 25 TWh, depending on their hydrogen storage feasibility [23].

2.1.1. Subsurface hydrogen storage potential in the United States

Deng et al. (2025) examined the potential of converting an existing subsurface gas storage site to store hydrogen and compared it to the feasibility of doing the same with a depleted gas reservoir. They concluded that using an existing storage site would be nearly three times as feasible than a depleted reservoir and that it offered a more long-term stable perspective of storing hydrogen [18]. A similar approach was used to determine the feasibility of the storage sites in the United States. Using existing sites would mean a decrease of nearly $75\,\%$ in working gas. Yet most of the storage sites could maintain the deliverability if hydrogen were added to the natural gas blend. Thus, a large number of storage sites could be used to store hydrogen, despite the potential challenges [58]. A closer examination of depleted gas fields in the state of California indicated a potential storage capacity of more than 203 million tonnes of H_2 in ten selected porous storage sites. Nearly $75\,\%$ of it could be reconverted back to electricity, a sufficient amount for the north of the state [77].

2.2 Microbiology in porous subsurface formations

Contrary to microorganisms at the surface, the cultures encountered in the porous rocks are subjected to confined space and a significant limit in the availability of nutrients. Compared to the earth's surface, between 12 and $20\,\%$ of the world's biomass is found in the subsurface [5, 93]. The most common microbial organisms encountered in underground gas storage can be classified into three different types: bacteria, eukarya and archaea [69]. The cells have the following main components in their structure: ribosomes, cytoplasm, chromosomes, nucleoid, plasma membrane and cell wall. Prokaryotes are microorganisms which do not have a nuclear membrane surrounding its nucleus and one single chromosome. This is different to the group of eukaryotes, which have a membrane surrounding the nucleus and a greater number of chromosomes. Eukaryotes are cells within plants and humans [70, 80]. In general, prokaryotic cells rarely possess organelles with membranes.

Bacteria and archaea both belong to the prokaryotic species, which do not have a single nucleus, while eukarya have nuclei and mitochondria. Bacteria have cell walls made out of peptidoglycan while the archaea cell walls do not contain it. Cell walls containing peptidoglycan are very robust and serve as an excellent barrier to changes in osmotic pressure [81]. Bacteria can be found in many diverse environments, while archaea is predominantly present in subsurface systems, including many in extreme conditions, such as high temperatures and pressures. Most archaea are between 1 to 10 μm large [69].

Cell division is the process of microbial reproduction. Initially, the

chromosome inside the cell divides itself, followed by a cell growth, attaining its double size. When the cell reaches its final size, its center begins to split into two separate cells, marking the end of cell division [69]. The process of chromosome duplication and cell division requires energy input and a carbon source for this bio-reactive process. In the case of a UHS, hydrogen can be used as an electron donor for the microbes while carbon gases, such as CO_2, serve as a carbon source [96].

Different species of microbes might induce different types of reactions in conditions favorable to their metabolism. The biggest groups of microbes are the methanogenic and the sulfate-reducing microbes. According to the reaction described by Sabatier et al. (1913), in the presence of hydrogen and carbon dioxide, methanogenic archaea consume these two gases and produce methane and water as shown in the following Equation 2.1.

$$4H_2 + CO_2 \rightarrow CH_4 + 2H_2O \tag{2.1}$$

Equation 2.1 indicates consumption of hydrogen, leading to a decrease in the quantity of hydrogen and an increase in methane.

Apart from methanogenic archaea, sulfate-reducing bacteria, homoacetogenesis and iron-reducing bacteria are other common bioreactive processes involving hydrogen. These reactions consume hydrogen and produce various products as shown in the following Equations 2.2 to 2.4 [36].

- Another very common biochemical reaction encountered in the subsurface induced by microbes is the sulfate reduction in

which bacteria consume hydrogen and in liquid-dissolved sulfate (SO_4). The products of the sulfate reduction reaction are hydrogen sulfide (H_2S) and water, according to the following Equation 2.2:

$$5H_2 + SO_4 \rightarrow H_2S + 2H_2O \tag{2.2}$$

- Carbon dioxide and hydrogen can also trigger homoacetogenic reactions:

$$2CO_2 + 4H_2 \rightarrow CH_3OOH + 2H_2O \tag{2.3}$$

- Iron reducing bacteria consume H_2 for the following reaction:

$$3\ Fe_2^{III}O_3 + H_2 \rightarrow 2\ Fe_3^{II}O_4 + H_2O \tag{2.4}$$

2.2.1. Microbial growth and life cycle

Microbes usually accumulate forming populations with a large cell number. This accumulation of microbes in large numbers is also referred to as biomass. The unit for biomass can be absolute numbers, however, a more common used unit is cells per volume, e.g. $[\frac{\text{cells}}{\text{ml}}]$ or $[\frac{\text{cells}}{\text{m}^3}]$.

The most common method to investigate microbial growth in the presence of the necessary substrates and at set environmental conditions (pressure, temperature, salinity, etc.) are predominantly performed in laboratory batch reactor experiments. In those experiments, the initial microbial number is quantified. Then the species

is inserted into the batch container, along with the relevant nutrients and substrates, securely sealed, and custom laboratory conditions are applied. The microbial number is then observed with time. The overall derived microbial growth curve and the behavior is depicted in Figure 2.2.

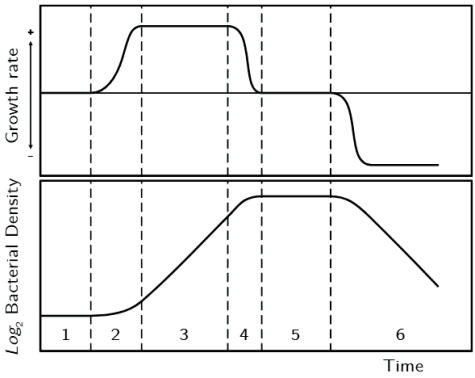

Figure 2.2: Microbial growth behavior in its various phases ([39, 72])

The microbial life cycle and the respective growth rates are distinguished into six different phases. Each phase has its own specifics which characterize the microbial life cycle:

1. Lag phase: No net growth in the microbial cell number occurs. The average cell number remains stable and the cell metabolism maintains the basic functions of the cells.

$$\frac{\partial n}{\partial t} = 0 \tag{2.5}$$

2. Acceleration phase: In this stage, the cells have adapted to the new environmental conditions. The metabolism accelerates,

the cells begin to grow and multiply in number [72].

$$0 < \frac{\partial n}{\partial t} \leq \psi_{max}^{growth} n \tag{2.6}$$

3. Exponential growth phase: The microbial metabolism is at its highest rate, corresponding to the maximum growth rate and largest increase in the population number:

$$\frac{\partial n}{\partial t} = \psi_{max}^{growth} n \tag{2.7}$$

4. Deceleration phase: The growth rate and population number begin to decrease due to depletion of substrates and nutrients [72].

$$0 < \frac{\partial n}{\partial t} \leq \psi_{max}^{growth} n \tag{2.8}$$

5. Stationary phase: The population growth ceases at a maximum microbial density; the growth falls into an equilibrium with the declining cell number [17].

$$\frac{\partial n}{\partial t} = 0 \tag{2.9}$$

6. Decay phase: The overall microbial population enters a decline phase due to complete absence of substrates. The microbial metabolism is no longer sustained and the process of dying microbial numbers becomes dominant.

$$\frac{\partial n}{\partial t} < 0 \tag{2.10}$$

To better comprehend microbial growth, mathematical models have been developed to describe this behavior. Most models were developed considering substrate-limiting conditions. Even though this is considered the main restricting factor, other growth-limiting influences have to be taken into consideration, for instance, limited space availability or a maximum mass-transfer.

One of the most common mathematical models is the Monod model, which describes the cell growth function as dependent on a single substrate [72] (Equation 2.11)

$$\psi^{growth} = \psi^{growth}_{max} \cdot \left(\frac{c^S}{\alpha + c^S} \right) \tag{2.11}$$

Here, ψ^{growth} and $\psi^{\text{growth}}_{\text{max}}$ are the growth rate and maximum growth rate $[\frac{1}{\text{s}}]$, c is the liquid concentration of the substrate S and α is the half-velocity coefficient.

For many microbial species, activating their metabolism requires more than one substrate, e.g. methanogenesis. Therefore, this model has been extended to the Double-Monod model to account for at least two substrates (Equation 2.12).

$$\psi^{growth} = \psi^{growth}_{max} \cdot \left(\frac{c^{S1}_w}{\alpha_{S1} + c^{S1}_w} \right) \cdot \left(\frac{c^{S2}_w}{\alpha_{S2} + c^{S2}_w} \right) \tag{2.12}$$

In addition, Hagemann (2018) proposed a newly developed formulation for the decay term to account for the decrease in the microbial

number [36]. Two different terms were proposed with b serving as the decay coefficient:

1. A constant decay: $\psi^{\mathrm{decay}} = \mathrm{b}$
2. A linear decay function dependent on the microbial number: $\psi^{\mathrm{decay}} = \mathrm{b} \cdot \mathrm{n}$

Coupling the decay with the growth term results in the following microbial behavior function:

$$\frac{\partial n}{\partial t} = \left(\psi^{growth} - \psi^{decay}\right) \cdot n \tag{2.13}$$

Most hands-on investigations of methanogenesis and other microbial processes have been conducted in laboratory experiments at scales between a couple of centimeters to a few millimeters. A multidisciplinary project CliMb (2019-2022) investigated the methanogenesis at a pore-scale in micromodels. The development of the microbial number over time was observed. The biochemical reaction parameters were determined numerically by matching the observed cell development with a growth model, which is a function of two gaseous substrates [98]. In batch experiments conducted by Strobel et al. (2023), the methanogenic archaea suspended in the liquid phase was pressurized with a hydrogen-carbon dioxide mixture to a value of 2 bar. In the course of the experiment, the decrease in pressure was observed and used for further parametrization of the numerical microbial reaction equation. The batch experiments clearly indicated microbial activity through the recorded pressure decline [97]. In another micromodel experiment, Liu et al. (2023) investigated the hydrogen consumption rate of sulfate-reducing mi-

crobes and the change in wettability in the pores. They concluded that during sulphate-reduction, the wettability of the pores changed slightly, potentially facilitating hydrogen injection and flow, while bioclogging and hydrogen losses through consumption adversely affected the storage of hydrogen [63]. Bio-clogging caused by microbial population has been investigated in Eddaoui et al. (2021) by modeling the microbial attachment to the pore walls of a conceptual model. Restrictions in the multiphase flow process, in particular upward hydrogen migration, was observed. However, the injected gas also penetrated into the reservoir in a more radial shape [25]. Shojaee et al. (2024) modeled the impact of methanogenic activity coupled with geochemical reactions in brine. They concluded that the composition of the formation water significantly influenced microbial activity and that hydrogen loss is the highest in high dolomite concentrations. The levels of reservoir pressure and pH impacted biochemical and geochemical activity, serving as preliminary indicators of reaction potential [92]. Effiong et al. (2026) analyzed methanogenic and sulfate-reducing reactions and examined the strongest reaction at various levels of the respective nutrient availability, using a cyclic operation method (injection of substrates - shut-in - production). Essential factors governing the reactions were the cell density, the duration of the idle phase and the storage pressure. Overall, microbial activity had its strongest impact during the static period and resulted in a reduction in hydrogen quantity. Especially, an unlimited availability of substrates intensified competition between the two reactions and increased the production of H_2S and CH_4. This process was accelerated by higher pressures and prolonged idle phases, both when the reactions were analyzed individually or combined [26].

2.3 Bio-reactive transport process modeling in porous media

The flow of gases, substrates and the transport of microbial species is divided into numerous coupled processes. The physicochemical processes are dispersion, diffusion and advection. The bio-reactive processes are microbial cell growth, decay, chemotaxis and metabolism [73]. Combining all these processes at different scales results in dynamic models integrating phase flow at large and microbial cell development at very small scales.

The overall formulation of the transport of gas through porous media is commonly described with the advection-dispersion-reaction equation, consisting of advection, diffusion and dispersion, which is shown in the following Equation 2.14:

$$\frac{\partial c}{\partial t} = \nabla \cdot (\mathbf{D}\, \nabla c) - \nabla \cdot (\mathbf{v}\, c) + R \tag{2.14}$$

where c is the concentration, D is the dispersive/diffusive coefficient, v is the advective parameter, and R is the source term.

The advection describes the transport of substrates along the flow direction at a larger scale (Darcy scale). This flow behavior of the phase through porous media is described by Darcy's Law, which is dependent on permeability and pressure gradient (Equation 2.15). The subscript j indicates the gas (g) or liquid phase (l).

$$u_j = -\frac{K}{\mu_j} (\nabla P - \rho_j g) \tag{2.15}$$

Here, $\mathrm{u_j}$ is the velocity [$\frac{\mathrm{m}}{\mathrm{s}}$], μ_j is the viscosity [$\mathrm{Pa \cdot s}$], K is the absolute permeability [m^2], g is the gravity acceleration [$\frac{\mathrm{m}}{\mathrm{s}^2}$] and ρ_j is the density [$\frac{\mathrm{kg}}{\mathrm{m}^3}$].

The dispersive/diffusive coefficient can be separated into molecular diffusion and gas mixing. This is shown in the following Equation 2.16:

$$D_j^\kappa = -\rho_j(D_{diff} + D_{disp})\nabla c \tag{2.16}$$

Here, $\mathrm{D_{diff}}$ is the diffusion coefficient [$\frac{\mathrm{m}^2}{\mathrm{s}}$], $\mathrm{D_{disp}}$ is the dispersive coefficient [$\frac{\mathrm{m}^2}{\mathrm{s}}$] and $\nabla \mathrm{c}$ describes the concentration gradient in mol. In this equation, the most important part describing the solute transport is governed by the dispersion of the solute through the porous media.

The source term R describes different types of flow-unrelated processes, through which substrates or solutes can be introduced into the system and impact the overall storage term. Chemical reactions that can be induced by microbial species coming into contact with the substrates can act as such a source term. The microbial metabolism consumes available substrates and reduces their quantities. In return, new components are produced and added to the storage term. These reactions are termed bio-reactive processes as they are of microbial origin. The growth of microbes is described with the previously mentioned Double-Monod model (c.f. Equation 2.12). At a Darcy scale, the microbes can accumulate as a volume (e.g. biofilms, structured) or in unstructured models (suspended free microbes). The focus is placed on unstructured models which

usually are in liquid phases, mobile and can attach and detach themselves from porous surfaces. The attachment and detachment process of mobile and immobile microbes can be written in the following way (Equations 2.17 and 2.18) [73]:

$$\frac{\partial C^{mm}}{\partial t} = -K_f C^{mm} + K_r C^{im} \tag{2.17}$$

$$\frac{\partial C^{im}}{\partial t} = K_f C^{mm} - K_r C^{im} \tag{2.18}$$

with K_f and K_r being the attachment and detachment rate [$\frac{1}{s}$], C^{mm} and C^{im} as the mobile and immobile microbial concentrations.

The general microbial growth behavior is characterized by the Double-Monod model [72]. This behavior also applies to the two structures in which microbial cultures can thrive. The growth of immobile and mobile structures can be modelled the following ways [73] (Equations 2.19 and 2.20):

$$\frac{\partial C^{mm}}{\partial t} = \mu_{mm}\, C^{mm} \left\{ \frac{C^S}{K^S + C^S} \right\} \tag{2.19}$$

$$\frac{\partial C^{im}}{\partial t} = \mu_{im}\, C^{im} \left\{ \frac{C^S}{K^S + C^S} \right\} \tag{2.20}$$

with μ_{im} and μ_{mm} as the growth rates for the immobile and mobile structures [$\frac{1}{s}$].

The consumption of substrates and production of new gases through these biochemical processes is a function of the microbial popula-

tion, kinetic parameters and reservoir properties. The conversion of the substrates (biochemical reaction) is proportional to microbial growth, as shown in Equation 2.21:

$$q_{bio}^{\kappa} = \phi \frac{\psi_{growth} \gamma^{\kappa}}{Y} S_w n \tag{2.21}$$

Here, ϕ is the porosity, γ^{κ} is the stoichiometric coefficient for each component κ involved in the reaction, Y is the yield $[\frac{1}{\text{mole}}]$ and S_w is the liquid saturation. Yield states the microbial amount produced relative to the consumption of one mole of a substrate.

2.4 Storage and Well Integrity

Integrity describes the ability of a storage site to store a gaseous medium in designed quantities, to contain it and to prevent it from escaping. The operation of a current underground gas storage site (UGS) is possible only when its integrity has been assessed and ensured. As the operation of a UGS has been performed for many years and it is supposed to be ensured for many decades to come, it is vital to conduct an assessment of its integrity if it is considered to be used as a UHS.
Integrity can be classified into two principal categories: geological and technical integrity. The geological integrity pertains to the capability of the geological setting to safely store and maintain the stored medium inside the pore space below a sealing caprock (in aquifers or porous media) or within the void space surrounded by an impermeable salt formation (salt caverns). The technical integrity describes the compatibility of the wells and the completion material

with the stored gas, and the well's ability to withstand elevated fluctuating temperatures, pressures and bio- and geochemical reactions. The assurance of integrity is to prevent any kind of losses of the stored medium through the geological layers or through the technical components. The main leakage pathways in a porous storage formation are depicted schematically in Figure 2.3.

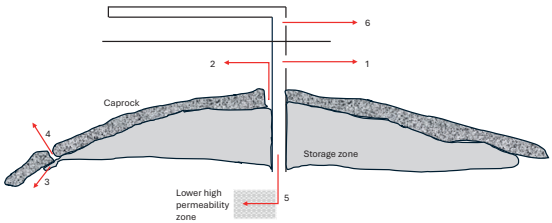

Figure 2.3: Potential gas leakage pathways from a storage rock (adapted from Katz and Lee (1990) [54])

1. **Joints:** The casing, tubing, packers and seals are subject to pressure and temperature variations over time, as the storage cycles continue. Fatigue development and degradation are significant influencing factors on the material. These effects might be more substantial when hydrogen is used as the stored gas, causing embrittlement and potentially corrosive substances. Corrosion and embrittlement challenge the integrity of the available structure, potentially developing cracks and gas migration pathways.

2. **Cavities in the cement layer:** The cement provides the structural stability to the entire well and its tools, and keeps it in place to operate safely. The cement layer around the wellbore

also acts as an artificial impermeable barrier and prevents the stored medium from escaping. Bio- and geochemical reactions triggered by hydrogen can alter the tensile and compressive strength of the cement, potentially developing structural openings and resulting in a loss of stored hydrogen.

3. **Spill points:** These points are critical areas of the storage site where the stored medium might leak across a lowest point in the caprock.

4. **Caprock:** In previous storage operations, the caprock has served as a sealing barrier preventing the stored natural gas from escaping. As hydrogen is to be stored, its small molecular size and increased reactivity with other minerals could breach the caprock's integrity. The exceeding of capillary threshold pressure, the geochemical alteration of the caprock and cavities large enough to enable upward hydrogen migration are uncertainties pertaining to the caprock.

5. **Downward migration:** Geological features such as fractures and faults direct the gas to move along a geological structure. Connecting faults can also deviate the flowing direction. It is essential to understand these features to predict and control the subsurface gas flow through porous media.

6. **Pipelines and valves:** The alterations in storage and production conditions over time noticeably impact the surface components by putting different levels of stress on those, leading to degradation, fatigue and potential development of cracks. To mitigate these possibilities, the selection of appropriate materials and constant inspection can reduce the likelihood of

the development of leakages.

Examining the geological structure and the technical installation is critical to detecting the migration pathways for gas. State and national regulations and frameworks require these precise examinations and proof that the geological and technical structure are capable of maintaining the stored gas within the porous media. The applicable framework within the European Union are the European Norms (EN) 1918 1-3 [19, 20, 21]. These frameworks impose safety standards and applications to subsurface gas storage in aquifers, oil- and gas fields and leached salt caverns. In Germany, these frameworks also apply, along with guidance recommendations provided by the State Mining Authority for Mining, Energy and Geology (LBEG) of Lower Saxony. The European Standards describe that the design of the storage operation should not compromise safety standards, or pose potential threats to the environment or the public and it should control fluid and gas migration processes. The safety evaluation encompasses the reservoir, the conditions of the fluids within the porous media, sealing caprock, storage quantities and well capacities. The frameworks and guidelines also provide instructions on the well layout, the components' suitability to contain the stored gases within the storage site, and appropriate monitoring strategies for subsurface gas storage facilities.

2.4.1. Geological integrity

The safe storage and containment of gas is ensured by the caprock and storage rock. The storage rock is a porous rock in which the gas is being stored. The caprock is the overlying rock layer, which is a dense, compact zone of a nearly impermeable rock, which forms

a barrier and prevents the upward migration of fluids and gases from the storage rock. Common types of porous storage rock are sandstone and carbonates. Caprocks are predominantly clay, shale or salt layers [1]. In each rock type or at the boundaries between the rock layers, a close analysis of potential geochemical or biochemical interactions, fluid migration or pressure development needs to be performed in order to adequately assess the stability and integrity of the layers.

Storage Rock

The storage rock is found in predominantly porous reservoirs, which were discovered as either oil or gas reservoirs. After depletion, many were converted to a subsurface gas storage site. In this subchapter, the types of storage rock and some of their characteristics will be mentioned which are critical to ensuring their integrity and stability.

The most common type of storage rock is sandstone. Sandstone consists mainly of a mixture of fine and coarsely-grained quartz (SiO_2). Porous reservoirs have sufficiently high values in porosity and permeability to store fluids and gases and to let them migrate through the layers. For instance, Zhou et al. (2022) reported average values of 10.8% for low porosity, 15.8% for medium and 31.5 % for high porosity sandstone [111].

In the German state of Lower Saxony, sandstone is the most common storage rock. This sandstone is classified as the Bunter Sandstein, which covers nearly the entire area in Northern Germany in depths ranging between 1100 and 3500 meters, with locally deviating depths. This formation is characterized by elevated

temperatures, porosities and permeabilities ranging between 18 and $20\,\%$ and 125 to 250 mD, respectively. Many previous and active gas fields were and are located in this formation [2, 78].

Caprock

Caprock integrity assessment addresses the rock layer over the storage rock which provides a natural barrier to prevent the stored gas from escaping the storage rock. The ideal caprock is compact and has porosity and permeability values ranging close to zero. The most common types of caprocks found in Northern Germany are salt layers and rötpelit. Salt layers mostly belong to the Zechstein layer and the rötpelit are clay layers which might also contain some anhydrite. Additionally, salt has the characteristic that it can flow. This means that any changes in stresses in the caverns might cause a slight change in the entire structure of the salt layer. The salt layer will not retain its original position in the long run. This will lead to a salt movement towards the cavern and a reduction in storage volume, a so-called creep convergence. The analysis of the caprock and the respective overburden layer should focus on the lithology, the hydraulic and petrophysical characteristics, the capillary threshold pressure, fracture gradients and the thickness [19, 20]. Another common type of caprock is shale. Porosity within caprocks can range from 0.04 to nearly 0.9 % in salts and between 0.11 to occasionally 4% in shales. Permeability values in shale can range from $3.8 \times 10^{-2}\,\mathrm{mD}$ to $9 \times 10^{-6}\,\mathrm{mD}$ and down to nearly $1 \times 10^{-8}\,\mathrm{mD}$ in salts [61, 104, 109].

2.4.2. Technical integrity

Technical integrity pertains to the storage wells used for injection and production operations into and out of the storage rocks. Over time, these wells have been subject to many different pressure and temperature levels. Years of operation have impacted the well material. After many years of cyclic operation, numerous gas production and injection processes, and the exertion of various pressure levels on the material and the technical equipment, the material changes its structure. This can compromise its sealability and might provide pathways for gas leakage out of the storage site. Inadequate cement plug lengths can increase the leakage rate by 60 %, with a majority of failures occuring in casing and at wellheads [55]. These leaks might develop through the well casing, cement or between the casing and cement and between the formation and the cement. An overview of some of the potential gas migration pathways from the storage site into the well and through its components is shown in Figure 2.4.

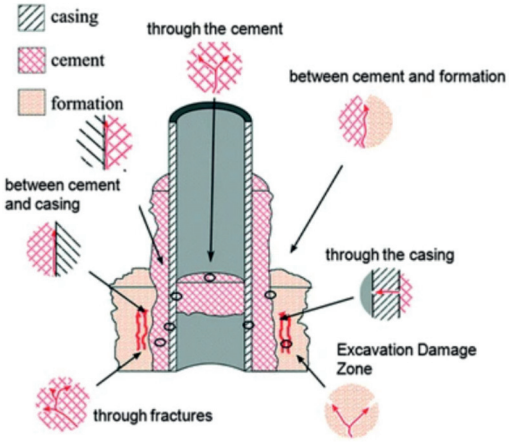

Figure 2.4: Possible leakage pathways for gas from the storage rock into the well or into overlying formations (plugged well) [47, 87]

- **Through the cement:** The cement provides a layer of stabilization around the casing and tubing to keep the well within its position during the storage operation. The cement also provides a sealing barrier in the drilled hole to maintain the gas inside the storage site. Most cement layers have been designed to keep the elements of natural gas in the storage formation, in particular methane and ethane. Due to the smaller molecular size of hydrogen, the cavities within the cement might be larger and wider and enable the migration of hydrogen through the cement layers. The integrity of the cement might also be compromised by bio- or geochemical reactions between hydrogen and other elements (e.g., hydrogen sulphide) or bacteria, causing embrittlement or corrosion.
- **Between cement and casing / between cement and forma-**

tion: The interface between cement and casing might weaken the binding forces during the operational years leading to cement shrinkage. When these binding forces decline, cavities along the interface might form, enabling pathways for the stored gas to migrate out of the storage site. Similar processes might affect the bond between the cement and the formation. The aging of the cement, its exposure to pressure changes and potential bio- and geochemical reactions could also provide leakage pathways between the formation and the cement layer.

- **Through the casing:** The exposure to hydrogen might cause hydrogen embrittlement on the casing surfaces, significantly compromising the technical component integrity of the casing. The available casing has also been selected for the storage operation with natural gas, meeting these specific needs designed for gas storage site. As the casing material has microscopic gaps and minimal fractures, hydrogen might migrate through these and escape the storage site.
- **Through fractures:** Fractures and fissures within the storage and the caprock always pose a certain risk to the structural integrity of the storage site.

The material of the well is the biggest concern to operators when the integrity of the well for upcoming storage seasons is considered or the possibility of storing hydrogen is taken into account. Therefore, the German Association of Energy and Geology (BVEG) has proposed a dual-barrier-system for every available gas storage well. The following Figure 2.5 depicts the recommended double-barrier-

system for a well at open-flow potential.

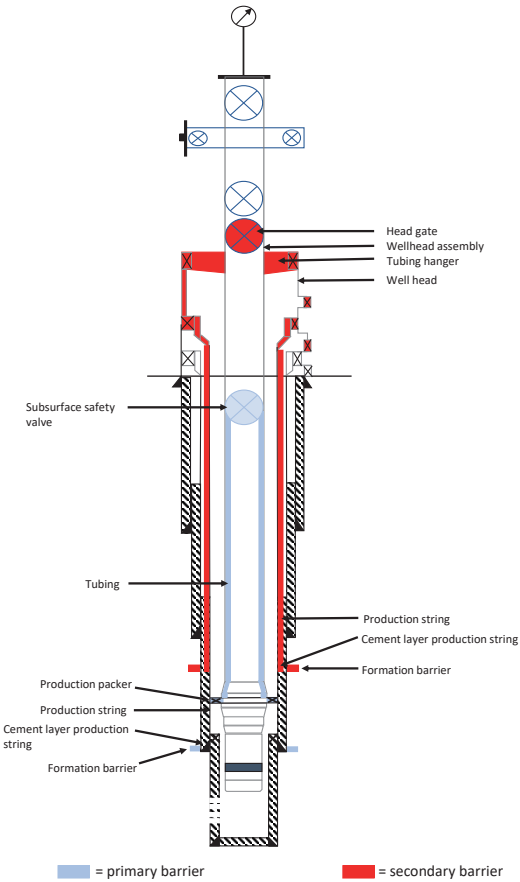

Figure 2.5: Double barrier system of an operating underground gas storage well in porous media (adapted from [13])

The compatibility of the well materials when exposed to hydrogen still requires precise evaluation. The prevention of potential hydrogen leakage through its components remains a partially unresolved issue. For these reasons, examining the technical layout for its suitability to contain hydrogen is essential.

Experiments by Hussain et al. (2022) [45] and Iorio et al. (2022) [108] have investigated how the compressive strength of a cement plug changes when it is exposed to hydrogen compared to a plug that has not been exposed to it. Hussain et al. (2022) prepared two different types of cement, one wet and one dry. Each cement specimen was divided into four equal parts. Parts two to three were exposed to hydrogen at different time lengths. The first part was not exposed to the gas. Afterwards, X-Ray CT pictures of the cross-sections were taken, and the compressive strengths of all parts were measured. The results showed that the cement samples exposed to hydrogen had a lower compressive strength and an increased plastic viscosity. Some of the hydrogen got trapped within the cement samples as bubbles, reducing the cement stability and having an impact on the surrounding facilities. This pertained to both the dry and the wet samples [45].
It is also critical to investigate how existing older samples react in the presence of hydrogen. Such experiments were performed by Iorio et al. (2022) and Boersheim et al. (2019). Iorio et al. (2022) prepared two batches of cement; the first was a slurry consisting of API class G cement, the second one contained a class G cement with an additional 35 % of silica. These samples were cured for 28 days and the exposure to hydrogen was performed at dry conditions, the

temperature was set to 90 °C and the pressure value was 150 bar. Porosity and permeability measurements were done before and after the exposure to hydrogen. The permeability measurements indicated that the values for both batches after hydrogen exposure were very close to the initial dry conditions. This indicated no significant mechanical impact on the cured cement samples. Furthermore, the resulting compressive strength tests revealed that the cement of the batch containing pure cement had a reduced compressive strength. The second cement batch (containing silica) appeared to have an increased compressive strength [108]. This indicated that the compressive strength of the pure cement sample altered more than that of the mixture sample containing silica.
The goal of the conducted autoclave experiments in Boersheim et al. (2019) was to determine the effects of fluids present in UGS on material steels and cement, predominantly commonly used in gas storage technology [7]. Samples of used steels, in this case steel grades N80, P110, K55, J55, and cement samples of API Class G were assembled with a sandstone to a composite core. This core represented the connection area between the reservoir, the cement, and the steel casing. It was placed into an autoclave, which was flooded with synthetic brine. In the autoclave, characteristic reservoir temperatures and pressures were set that acted on the core (80 °C, 50 bar). Permeability and porosity measurements before and after the autoclave experiments were done. The measurements of the composite cores revealed a reduction in porosity and permeability during the autoclave experiments. There is still much uncertainty surrounding the changes in permeability and porosity in the composite cores. The most common theory is that the precipitation of salt minerals occurs in the pore throats. Another

one hints at the possibility that hydrogen interacts with minerals, like sulfur, leading to pore clogging. This is also supported by a clear increase in the pH-value of the samples. Simultaneously, the permeability of the class G cement increased while its porosity decreased. Boersheim also measured the tensile strength of the different types of steels before and after the exposure to hydrogen in the autoclave. It was noted that no visible hydrogen embrittlement was noticed on the samples and the tensile strength of the samples remained unchanged. The experiments also measured the change in the components in the reservoir brine fluid before and after the exposure to hydrogen. A slight increase in chrome and iron was detected in comparison to the initial condition before the exposure to hydrogen. The concentration changes of these materials could reveal a slight change in the steel composition with time [7]. A degradation in steel and cements in the presence of CO_2 and H_2S was noticed in the work conducted by Jun et al. (2026). While corrosive gases degrade the quality of cement (Class G, Class H, Portland cement) and hydrogen embrittlement contributes to the degradation of steel, hydrogen-saturated solutions can prolong the stability of the cement [51].

Depending on the respective storage site and its characteristics, bioreactive processes impact the material compatibility with hydrogen and the resulting products. Hydrogenotrophic reactions, especially sulfate-reduction (Equation 2.2), is a very critical concern for the technical stability, as it can affect the cement sheath, elastomers, packer and the pipeline steel [105]. Hydrogen sulphide is a corrosive and at a concentration as low as 2-5 ppm, it may already

lead to headaches. The critical level of exposure to hydrogen sulphide is at a concentration of 100 ppm which might be lethal if the exposure time exceeds 48 hours [106]. Furthermore, it might also induce and promote corrosion to material and also embrittlement. According to Ugarte and Salehi (2022), an appropriate selection for future UHS operations are low to intermediate strength steels with high-strength steels being more susceptible to embrittlement. Austenitic steels have intermediate strength, and therefore are more resistant towards H_2 diffusivity and to fatigue. Concerning the cement, the authors also recommend class G with low quartz concentrations, the inclusion of silica, and to maintain a low ratio of water-to-cement. The specific site characteristics, diffusion potential, corrosion and embrittlement resistance are driving issues which need to be addressed in the selection of well material [105], [66].

The analysis of geological and well integrity has been a key objective for many research institutions and projects. Using existing subsurface gas storage locations and the years of successful cyclic storage operations have provided valuable information on determining the suitability of the available storage locations to potentially store hydrogen. In the recent EU-wide project "HyStories", gas storage sites throughout Europe and the most recent studies on bio- and geochemical interactions between microbes, minerals and hydrogen were screened. These efforts led to the development of a handbook containing criteria that is recommended to be followed for screening a potential storage site for its suitability to store hydrogen. These criteria pertain to the analysis of geological and reservoir conditions and the most important aspects and determined critical values are listed in Table 2.1.

Table 2.1: Screening criteria to select a suitable subsurface hydrogen storage site based on findings by HyStories

Parameter	Value
Minimum to maximum depth of the reservoir top	500 - 2500 meters
Closed impermeable storage area	$\geq 0.3\ \mathrm{km}^2$
Minimum effective porosity	carbonates $5\,\%$, sandstone $10\,\%$
Minimum permeability	carbonates $10\,\mathrm{mD}$, sandstone $50\,\mathrm{mD}$
Preferred rock mineralogy and types	homogeneous carbonate, sandstone, impurities are not desired
Available in-situ reservoir fluid	depleted gas field preferred
Initial reservoir temperature and aquifer influence	known information to assess potential reactions

The overview developed in HyStories has shown that numerous factors must be considered, ranging from geological and tectonic assessments to reservoir analysis. The presented criteria in Table 2.1 are only some of the most important parameters that have been investigated. For each potential storage site to be converted, an individual examination has to be carried out and individual and

site-specific aspects need to be considered.

Chapter 3

Microbial growth experiments coupled with gas chromatographic measurements and numerical modeling

Currently, there is still a lack of complete understanding how microbial processes influence the storage of hydrogen during a shut-in and dynamic storage operational period. In this part, a similar experimental procedure as described in Strobel et al. (2021) is introduced [95]. A gas mixture containing 80% hydrogen and 20% carbon dioxide (CO_2) is injected into a micromodel which is saturated with a liquid mixture consisting of methanogenic archaea and a nutrient medium, which provides the relevant nutrients for microbial growth. One essential difference to the setup presented in [95] is that in the experiments presented in this chapter, the gas mixture is constantly injected into the micromodel at a very low flow rate ($\mu\mathrm{l}/\mathrm{min}$). Additionally, a micro gas chromatograph is installed behind a backpressure regulator connected to the outlet and measures the composition of the outflowing gas.

3.1 Microbial species and culture media

The microbial species used for these experiments were hydrogenotrophic methanogenic archaea of the strain methanococcus thermolithotrophicus (DSM 2095). This methanogenic species is precisely analyzed and described in Huber et al. (1982) [44].

Methanococcus thermolithotrophicus is a prokaryotic species that thrives in high-temperature and relatively salty sediments. Its optimal growth parameters are: temperature = 65 °C, salt concentration = 4 % and pH = 7 [98]. To establish an environment with sufficient nutrients and to facilitate conditions for microbial growth, a culture medium is necessary. A culture medium contains vital irons, extracts and other ingredients which act as additional nutrients for the microbes. Samples of the methanogenic archaea strain and cultural medium were provided by the microbiological service company Microbify GmbH. The cultural medium has a similar consistency to the media (DSMZ 141) provided by the German Collection of Microbes and Cell cultures (Deutsche Sammlung von Mikroorganismen und Zellkulturen), but it has a lower content of organic components. This modification of the culture medium was made to facilitate the growth of the methanococcus thermolithotrophicus species. As a reduction component, sodium sulfite and slightly higher concentrations of iron, nickel and sulfur as tracer elements are included.

3.2 Experimental devices and setup

The designed experimental setup consists of the following primary systems: the gas-liquid handling, the microchip, the image acquisition and the gas analysis system. The three systems and their structures are pictured in the following Figure 3.1 and described in the subsequent paragraphs. The technical sketch of the entire setup with the naming of all external components is shown in Appendix A.1.

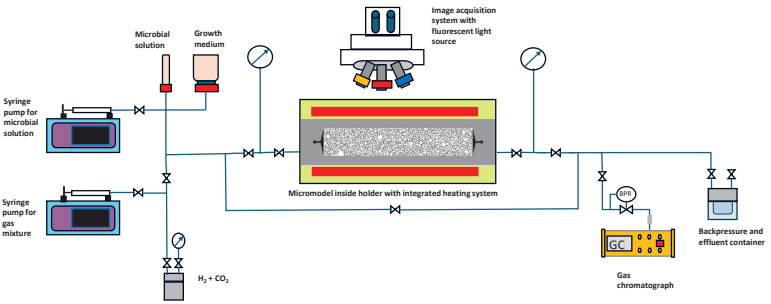

Figure 3.1: Experimental microfluidic setup

3.2.1. Gas-liquid handling system

The components of the gas-liquid handling system ensure that both a liquid and a gas phase can be transferred in sterile and anaerobic conditions. This system consists of steel containers, microfluidic flow lines, valves, syringes, and syringe pumps. The three steel containers used are high-pressure containers with a resistance of up to nearly 100 bar. One is used to apply backpressure to the system by using purified nitrogen. Another steel container is used to apply the same level of pressure to the backpressure regulator in order to control the flow of gas through it to the micro gas chromatograph. Two low-rate syringe pumps (Harvard Pumps Series 11 Elite, Harvard Apparatus Ltd.) are used to inject either the liquid or gas into the system at very precise flow rates. The liquid phase contained a nutrient-microbial mixture (ratio 50%-50%). Glass syringes (Hamilton Class C1010) are used to contain and inject the liquid into the flow lines (ID: 0.5 mm, OD: 1/16”, Polyetheretherketone (PEEK)

material), which ensure extremely low gas diffusivity through the material. The flow lines are connected with two-way PEEK valves (Upchurch Scientific). In front of and behind the micromodel, two highly sensitive absolute pressure sensors (Elveflow) are installed to monitor and observe the changes in the system pressure.

3.2.2. Microchip and holder system

The microchip system consists of a micromodel holder, which contains a micromodel (microchip), an integrated heating and data acquisition system. The material of the holder is polyetheretherketone (PEEK), which was selected for its properties. PEEK material has a density of $1.32\,\mathrm{g/cm^3}$ and an elastic modulus of $3600\,\mathrm{Megapascal(MPa)}$, making it extremely resistant to deformation. The heat conductivity of PEEK is very low ($0.25\mathrm{W/K\cdot m}$), making it a good insulator, which is an advantage for the micromodel experiments. These are conducted at high temperatures and the maximum applicable temperature that it can withstand, without deformation, is nearly 240 °C [85]. On the left and the right side, the micromodel holder has drilled holes with a thread diameter and a smaller 1/16 ″ diameter, through which the fluid and gas can flow. In the void space in the central part of the holder, a rectangular indium tin oxide (ITO) coated glass plate is placed, which is a component of the heating system. This ITO glass is transparent and has good electric conductivity (length= 38mm, width= 55mm, height = 3.3 mm) [79]. On the long edges of the ITO-plate, two L-shaped brass forms are glued to them. They serve as electric conduits from one set of springs to the other set. These springs are located on the upper and lower frame of the holder, which maintain

the ITO-plate and the microchip in place. On the in- and outlet sides of the holder are two horizontal threads with a length of 9 mm each. On each side below the in- and outlet of the micromodel, a circular notch with a width of approximately 2.5 mm is carved into the holder. An o-ring shaped gasket (inner diameter (ID): 0.74 mm, outer diameter (OD): 1.02 mm, Manufacturer: DuPont Kalrez) is fitted inside these notches, which provides a seal to the in- and outlet openings of the microchip, and enables a steady in- and outflow of gas through the microchip. The actual microchip is placed on top of the ITO-plate. An outer black metal frame, which covers the outer PEEK frame of the holder, is tightened with four screws. This outer frame holds the micromodel in its position directly over the out- and inlet channels, and maintains the sealing capacity of the chip. This plate is placed on four springs, which provide an electric current and a certain temperature to the plate. Two temperature sensors, which measure the temperature of this plate, are attached to it.

The other major component of this system is the micromodel, also referred to as microchip. This microchip is inserted into the micromodel holder and fixed with screws. The micromodel is made of borosilicate glass-silicon-borosilicate glass layers. Small holes on every side of the micromodel either act as an inlet or an outlet for the flowing medium. The microchip is a quasi two-dimensional model with a length of 5 centimeters, a width of 9 millimeters and a height between the two glass layers of 50 micrometers (µm). The gap between the upper and lower glass layers contains the internal porous structure, which is made of silicon. Silicon has been chosen due to its high resistance to many different liquids, even corrosive

ones. The internal structure can either be an artificial one which is made of circles of different sizes and pore throats with different widths, or it can be a two-dimensional replication of a real core sample. An example of the latter structure has been described in Gaol et al. (2020) and Lüddeke et al. (2022) for liquid immiscible displacement experiments [32, 67]. An example of the former micromodel, which is used in the performed experiments, is depicted in Figure 3.2.

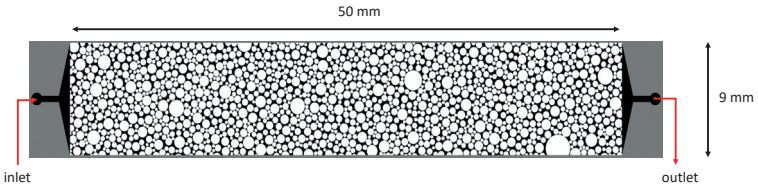

Figure 3.2: Schematic structure of the linear circle micromodel used

The depicted linear-circle micromodel has an internal structure which consists of various circles with different radii and pores of different throat sizes between them. The average porosity is approximately 0.28. The average determined permeability of the microchip is about 6 Darcy. The non-uniform pattern of the different pore radii should provide a non-constant resistance towards the flowing medium. Different flow velocities of the medium within the model could be the consequence.

3.2.3. Heating and data acquisition system

The proposed experimental process requires a constant elevated temperature to the microchip to enable and control the growth of the

microbes. The heating system also needs to be reliable and include safety features to prevent overheating or other malfunctions, which could cause damage or pose other hazards to the equipment and the operators. Therefore, a heating coupled with a data acquisition system was developed by the ITE to combine all necessary safety features and recording framework into one application. The electric current from the brass frames across the ITO plate is provided by an electric module constructed by National Instruments. On the lower side of the ITO plate, located just slightly above and below the micromodel, two temperature sensors are attached, measuring the respective real temperature in the microchip. One sensor is set as the primary sensor, which provides the target value according to which a temperature sensor device, also constructed by National Instruments, analyzes the value and provides this information to the electric regulating device.

The control and setting of the temperature and the collection of experimental data (pressure and temperature) require a reliable, quick graphical interface. A program in LabView was developed which includes all functions that are relevant to the general procedure of the experiment, especially the setting and regulation of the temperature of the ITO-plate, the observation of pressure values at the in- and outlet, and the control of syringe pump flow rates. The values shown in this program are the pressure values in the in- and outlet channels of the micromodel, the temperature values in the sensors, the set temperature, the flow rate in the syringe pump and the pressure applied to the backpressure regulator. Another function enables the activation and deactivation of the heating system and the setting of the target temperature. The interface

is equipped with a warning function: Any malfunction of the electric current or circuit from the power socket is indicated with an intermediate flashing red light. All the measured parameters and values can be stored in one common file. The interface of this heating control and data acquisition system is shown in Appendix A.2.

3.2.4. Image acquisition system and processing method

The holder with the fixed micromodel is placed below a microscope (Axio Imager.Z2m Carl Zeiss), equipped with four different objective lenses (5x, 10x, 20x, 40x). The microscope has a high-resolution camera (Axiocam 305 MRc), which can acquire images of different magnifications and in different light sources. The five-fold magnification lens is used to assemble a picture of the entire microchip. The largest magnification lens (40x) is used when enlarged images of selected pores inside the micromodel are examined. The magnification power of 40 is used to count the number of microbes. Various light sources (Halogen Reflected Light and Transmitted Light) are available to observe static micromodel characteristics and saturation changes inside the pores of the micromodel. The setup also includes a fluorescent light generator (Visitron Systems HXP 120). With the fluorescent light, the activity of the microbes can be observed clearly and their numbers can be determined. During the experiments, the camera takes pictures at a five-fold magnification and a forty-fold magnification lens. Using the microscope software ZEN, the five-fold magnified images are assembled into one picture depicting the entire microchip.

In MATLAB, an image processing code was developed to analyze the images of the microchip for the development of the microbial number and the areas of microbial activity. To visualize the microbes and enable the count, the processing code also includes the coloring of the processed images to enhance their visibility. The image processing method is sketched in the following Figure 3.3.

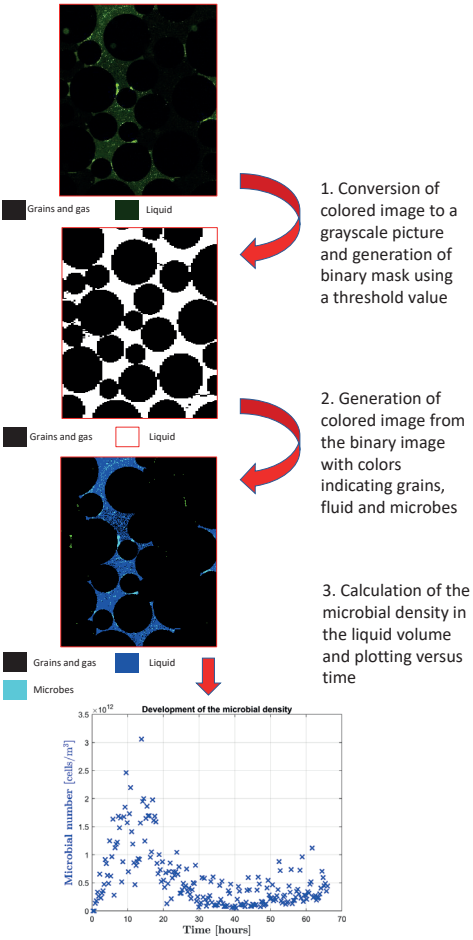

Figure 3.3: Image processing method developed within MATLAB

The input images into the processing code are the raw image pictures before the first step in Figure 3.3 is executed. The grains are

depicted dark, while the pores are shown in a bright green color. The pores are filled with the medium-microbial mixture, which contains enzymes that are activated in the presence of fluorescent light [22]. The gaseous phase is depicted in a darker color, distinguishable from the grains. The first step of the image processing method is to create a lithographic mask of the micromodel used (Step 1). The mask contains all circular grains, which are considered permanent components which are subtracted from the calculation of the microbial number. After subtracting the lithographic mask from the images, only the pore channels remain as void spaces.

In Step 2, the image processing tool separates the raw image into its red, green and blue colors. The use of the green color spectrum is vital for the counting of the microbial number. In the green fluorescence, due to the activated enzyme inside the microbes, the microbial organisms will shine in a very bright green color inside the liquid. Gas will appear as a dark area in the pore space. Using the Otsu's threshold method, an average graythresh level is calculated which is applied to generate a binary image of the liquid phase inside the pores. Each pixel representing the pore space is analyzed to determine if the green graythresh value in every pixel is above or below the threshold value (1 pixel = 5 micrometers). If a pixel-dependent value is above the threshold value, then this pixel is considered to represent microbes. The entire picture is analyzed, and the total number of microbes is determined. Apart from the microbial number, the microbial density (number of cells per liquid volume) is also estimated.

The last stage (Step 3) of the image processing algorithm is to enhance the visibility of the image by selecting appropriate colors.

The final processed and colored image shows the grains colored in black, the liquid phase shown in blue, and microbes are colored in turquoise. Each determined value of the microbial density as it develops with time is plotted.

3.2.5. Gas analysis system

The gas analysis system consists of a micro gas chromatograph, which can accurately measure the gas composition at ultra-low flow rates as low as $10\ \mu\mathrm{l/min}$ (IGraphX). The device contains three inlets, one for the carrier gas and two for the sample gas. The two other gas inlets are selected based on the flow rates of the gas. One inlet containing a wider channel is used for flow rates greater than $100\ \mu\mathrm{l/min}$. The inlet for very low flow rates ($1 - 100\ \mu\mathrm{l/min}$) has been selected for these experiments. The carrier gas was 99.999% argon and the rest was methane. In the gas chromatograph software (GCManagerPro), the device operation and measurement parameters (measurement time, injection time) were set before the experiments commenced. During the experimental process, the gas compositions were continuously measured and analyzed.

The gas chromatograph was calibrated using two different available calibration gases. One calibration gas consisted of 0.5% methane and hydrogen, and the other one contained 0.05% of methane and hydrogen, the rest was argon. With these gases, very small concentrations of those two gases could be precisely detected in the measurements. A depiction of the graphical measurement results is depicted in Figure 3.4.

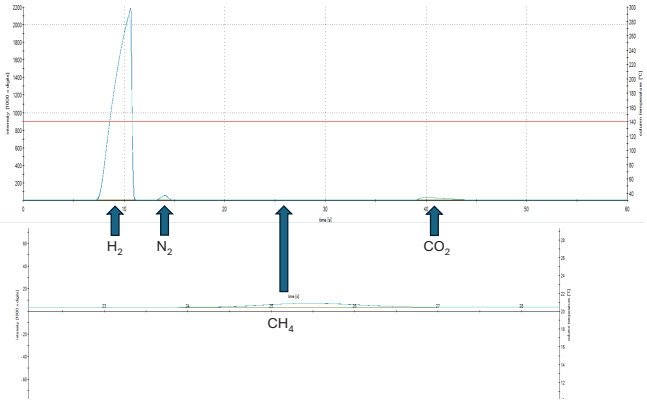

Figure 3.4: Visual depiction of the measured gas components and their concentrations in the micro gas chromatograph

The gas composition is plotted as the respective intensity of the gas versus the retention time, detected in the built-in separation column. The gas analysis in Figure 3.4 shows four distinct peaks, indicating four different gases and their respective intensities. The methane concentrations were calibrated at very low values, thereby providing precise values for this gas. Hydrogen is constantly injected at high concentrations (80%), leading to permanently high measured values. During the experiments, the gas analysis focused on the development of methane.

3.3 Experimental procedure

The first step of the preparation involves cleaning all flow lines and the micromodel thoroughly. Filtered, distilled water is injected

through the flow lines and the micromodel to remove remaining residue. Afterwards, isopropanol is injected to flush the water out of the flow lines and the micromodel as an organic matter disinfectant. In the last step, distilled water is injected again into the system to displace the isopropanol. The flushing procedure is completed at high flow rates of up to 100 $\mu\mathrm{l/min}$, the ultimate injection rate of water can also reach 200 $\mu\mathrm{l/min}$.

After completing the flushing procedure, nitrogen floods the flow lines from the backpressure/effluent container to remove the distilled water from the flow lines and microchip. Another purpose to flood the system with nitrogen is to remove oxygen. The next step involves filling two gas-tight steel syringes (Harvard 8 ml stainless steel syringe) with a pressurized hydrogen-carbon dioxide mixture. The gas mixture is initially in a 100-ml steel container, which is pressurized with wet H_2-CO_2 up to nearly 10 bar. The valves to the two steel syringes are opened and the wet H_2-CO_2 mixture is withdrawn from the gas bottle into the steel syringes.

After completing the withdrawal of gas from the steel container, the microbes and the medium need to be mixed in a glass syringe. First, $3\,\mathrm{ml}$ of the medium is withdrawn from a glass sample container into the glass syringe. Then $3\,\mathrm{ml}$ of microbes are withdrawn into the same glass syringe. The glass bottle containing the medium is slightly pressurized to nearly 2 bar(g). Ultimately, the liquid mixture contains $6\,\mathrm{ml}$ of medium and microbes. This entire process is performed in an oxygen-free environment by flushing and filling all lines with nitrogen. It is also used to control the withdrawal of nutrients and microbes from the viles.

In the next step, the medium-microbial mixture is injected into the micromodel to saturate it. The backpressure of the system is set to 5 bar(g). A rate of maximum 25 μl/min is chosen because higher rates could cause greater, potentially damaging shear stress to the microbes. The injection process lasts for about 5 hours. After attaining a one-phase saturation, the gaseous mixture is injected into the micromodel. The injection and the development of the two-phase saturation in the chip are observed under the microscope. Once the gas front reaches the outlet of the micromodel, the gas injection process continues for about 3 hours until the saturations of the liquid and gas stabilize. After achieving constant saturations, the valve connecting the flow line from the outlet to the backpressure/-effluent container is closed. The flow direction to the backpressure regulator and the micro gas chromatograph is opened and an injection rate of 2.8 μl/min is set. A long-time measurement in the gas chromatograph software is initialized. The microscope software is programmed to take fluorescence pictures of the entire micromodel and of certain selected positions in the chip. The selected positions are magnified with a 40x objective and aimed at a gas-liquid interface or a position in the vicinity.

3.3.1. Experimental results

The development of the microbial density and absolute cell number determined in MATLAB needed to be synchronized with the gas chromatographic measurement results. This procedure would tie the microbial cell number to the gas readings. Much of the literature has presented the microbial development in various units and scales, with a semilogarithmic plot being one of the most com-

monly used ones. This permits the depiction of large numbers and a clear distinction of the growth phases by identifying the shapes of the curves and relating the population development to the initial number [97, 98]. In the following paragraphs, the results of the experiments (absolute cell number and cell density) are graphically shown in logarithmic form. The logarithmic scale was selected to observe the changes in the large microbial number at every time step relative to the initial number and to distinguish between the characteristic microbial phases. This enables a more precise comparison and visualization of the microbial development. Showing the absolute cell number clearly portrayed the different growth phases, their magnitude and their duration. The four phases are clearly distinguishable, especially the growth and decay phase in the later stages of the experiment. For each experiment, the analyses of the microbial density and the produced methane were performed and reproduced in DuMu^{X} later. In the following paragraphs, first the results of the four experiments are presented and discussed. Later on, the numerical simulation results are presented and compared to the experimental values. The microbial number is depicted in two semi-logarithmic plots; the first plot indicates the absolute microbial number and the second plot represents the cell density as cells per liquid pore volume. Even though both the absolute microbial number and the microbial density were analyzed, the determination of the liquid saturations inside the pore space was associated with some uncertainties. These originate from the microscopic light settings. Over time, the light intensity varied slightly, thereby changing the contrast between the liquid and gas phases, thus making the interface less visible. Occasionally, the contrast could not be clearly distinguished. This lead to imprecise saturation values for

these images. The determination of the absolute microbial number was more precise as the reflection of the microbes remained clearly visible.

Experiment 1

The duration of the first experiment (T = 40 °C) was approximately 40 hours. The visually determined microbial number and the methane (CH_4) concentrations are shown in Figure 3.5.

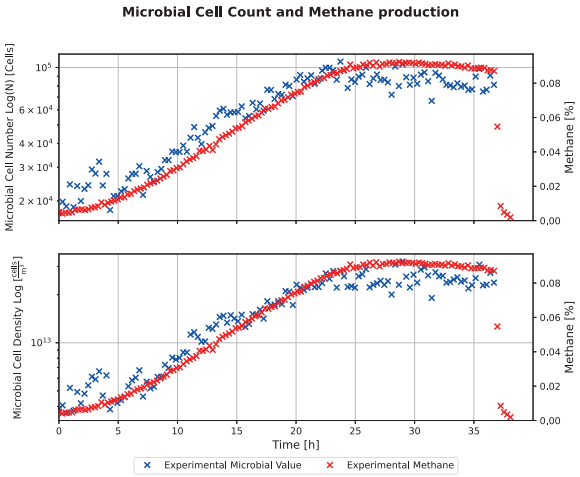

Figure 3.5: Microbial values and methane measured in the gas chromatograph

The gas measurements indicate that a very small increasing amount of methane is detected in the first five hours of the experiment. The initial methane concentration is nearly $0.001\,\mathrm{mol}\%$ and it increases to $0.015\,\%$. Then the methane curve has a constant linear increase until it begins to flatten out and reaches a maximum value of $0.09\,\%$

after nearly 26 hours. It maintains this quasi-stable maximum for about 5 hours before a very slow decline begins. Its final value during the gas injection process is nearly $0.085\,\mathrm{mol}\%$ when the gas injection stops.
The microbial number begins at approximately $2 \times 10^4\,\mathrm{cells}$ (approximate density $5 \times 10^{12}\,\mathrm{cells/m^3}$) and its mean remains stable during the first 6 hours. A subsequent increase in the absolute number is observed, which reaches a stationary maximum after nearly 25 hours ($2 \times 10^5\,\mathrm{cells}$ and $2.8 \times 10^{13}\,\mathrm{cells/m^3}$). This maximum value remains relatively stable during the rest of the experiment. Occasionally, some observed values oscillate around this median value. This can be related to certain artifacts or intermediate unstable light settings in the image, leading to a temporarily unclear image being analyzed. Nevertheless, the overall maximum mean microbial number and density values remain relatively stable.
A nearly parallel trend is noticed in Figure 3.5 between the microbial number and the measured methane. When the microbial number remains relatively stable in the initial hours, only a very small amount of methane is generated. Even though the initial microbial values appear to change minimally, a small degree of microbial activity seems very likely. As the microbial number increases, the methane values increase as well. Both curves reach a relatively stable maximum value and retain this level for approximately 5 hours before the methane values decrease.

Experiment 2

This experiment was also conducted at 40°C and lasted for nearly 5 days. In this procedure, the gas steel syringes were refilled twice with the fresh gas mixture. During the refilling, the micromodel

was closed in by closing the two-way valves at the in- and the outlet. The development of the experimental microbial density and gas concentration is shown in Figure 3.6.

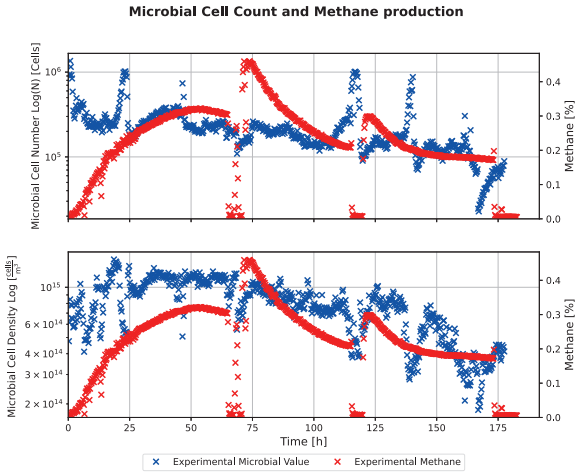

Figure 3.6: Microbial number and methane concentration over time at 40 °C

The CH_4 measurements at the beginning of the experiment indicate neither a lag period nor a temporarily stable low gas concentration. Instead, the gas concentration initially begins to increase slowly, followed by a sharp increase. This concentration growth begins to reduce after nearly 30 hours and reaches a maximum of nearly $0.32\,\%$ after 50 hours, after which a steady decline in the concentration follows. Between 65 and 70 hours, and 115 and 120 hours, the injection was paused for the refilling of fresh H_2-CO_2 gas from the pressurized steel container into the syringes and the micromodel was closed off. After reopening the valves to the micromodel, the

gas concentration shows a temporary sharp increase, almost linearly up to a value of nearly $0.44\,\mathrm{mol\%}$. After the third filling and injection of the substrate gases into the micromodel, the peak methane value is nearly $0.3\,\mathrm{mol\%}$ and the decline begins almost instantaneously. In this third time frame, the decline flattens out during a longer period compared to the previous two phases. The final value is nearly $0.18\,\mathrm{mol\%}$.

If the intermediate refilling phases, during which the model was closed in, were excluded, the methane curve would show a constant decline. After reaching its peak value of nearly $0.32\,\mathrm{mol\%}$, the gas concentration declines constantly, passing through 0.21 and ultimately ending at $0.18\,\mathrm{mol\%}$ in the following 100 hours. The peaks at the beginning of the second and third injection phases can be explained by a temporarily higher pressure acting on the inlet of the backpressure regulator. This originates from the higher pressure level inside the pressurized steel container. This elevated inlet pressure temporarily leads to an increase in the quantitative gas outflow into the gas chromatograph, culminating in a higher measured fraction of gas and an increase in the pressure acting on the backpressure regulator. This level decreases as the gas pressure inside the system reduces with the outflow and the flow of gas through the regulator subsides to its stabilized condition.

The development of the microbial number reveals that there is no lag phase and that the development is very volatile. Immediately, the values begin to change from the initial values of nearly $2 \times 10^6\,\mathrm{cells}$ ($4.5 \times 10^{14}\,\mathrm{cells/m^3}$) to about $2.5 \times 10^6\,\mathrm{cells}$ ($1 \times 10^{15}\,\mathrm{cells/m^3}$) within the first 10 hours, followed by an increase in absolute numbers. Afterwards, the average number begins to reduce slightly over a long time. In the intermediate refilling phases, the numbers begin to

deviate from the overall declining trend but usually return to it after some time. At the end of the experiment, about 1×10^5 cells are determined inside the micromodel ($4 \times 10^{14}\,\mathrm{cells/m^3}$). The observation of the microbial density and number reveals that there is no phase indicating a relatively stable microbial number and that the values change constantly during the experiment. In the overall long-run, the growth of microbes occurs in a very small time frame and the microbes can also maintain a specific density for just a few hours. This occurs at the beginning of the experiment and is short in relation to the entire duration of the experiment. The decay is the phase that dominates the majority of the experiment. The decay occurs at a very small rate but it is the dominant phase for approximately 100 hours of the total 180 hours, nearly $75\,\%$ of the duration. The methane production is reflected in the microbial values. After increasing and reaching a stabilized maximum value after nearly 50 hours, the rest of the experiment is dominated by a decline in methane. The values begin to stabilize at a particular level and maintain this value for the rest of the experiment.
The development trends of the microbial values and methane measurements appear nearly simultaneously. An increase in the gas values occurs when the microbial values increase. The same applies to the stabilization of the two parameters and the following decline. However, the produced methane at a specific time inside the micromodel can be detected with a slight delay in the gas chromatograph. Despite the delay, the trends in the microbial and produced methane values are evident.

Experiment 3

The third experiment was carried out with the same microbial

species but at room temperature (between 23 - 25 °C). The development of the microbial cell number and the methane values are depicted in Figure 3.7.

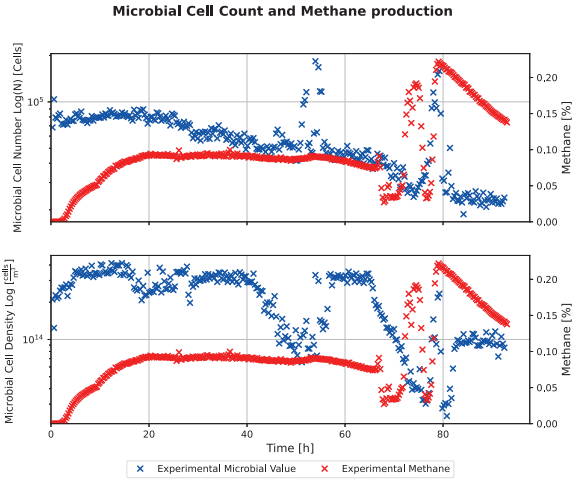

Figure 3.7: Microbial cell number and methane development at standard temperature

At the beginning of the experiment, no methane is measured for nearly 4 hours. The methane concentration increases nonlinearly and at two different slopes up to a value of nearly $0.1\,\mathrm{mol\%}$. For nearly 35 hours, CH_4 remains at this value. Afterwards, it begins to decrease very slowly over the following 20 hours. At the end of the injection, the ultimate CH_4 value is approximately $0.08\,\mathrm{mol\%}$. The slope of the methane curve after the refilling process is decreasing linearly, indicating no renewed increase in the methane trend. The analysis of the microbial number reveals that its initial increase is marginal, and the maximum number is reached after a very short

time (15 hours). Beginning at an initial value of 68000 cells (initial density $2.8 \times 10^{13}\,\mathrm{cells/m^3}$), the maximum value is nearly 80000 cells ($3.5 \times 10^{13}\,\mathrm{cells/m^3}$) after 20 hours. The remainder of the experiment is characterized by a continuous decline in values, which is temporarily interrupted by the refilling procedure between 70 and 75 hours. Ultimately, it reaches a final value of nearly $25\,000\,\mathrm{cells}$ ($1 \times 10^{13}\,\mathrm{cells/m^3}$) and maintains it.

Experiment 4

The last experiment was performed at 62 °C, which was close to the optimal microbial temperature of 65 °C. Due to technical issues with the camera, no pictures were taken of the microbes. Therefore, only the methane values were available for analysis, which are depicted in Figure 3.8.

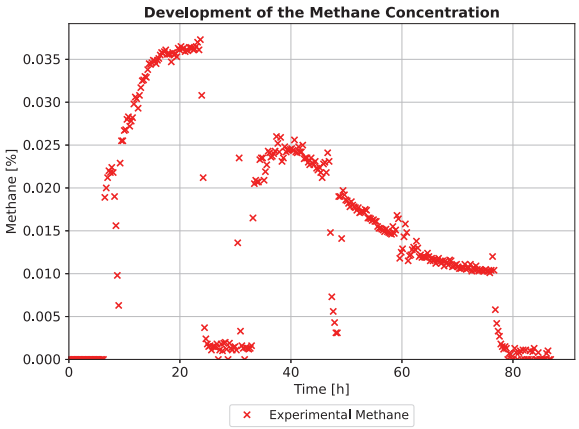

Figure 3.8: Methane concentration development at 62 °C

Initially, no methane is detected for nearly 5 hours. This period is

followed by a sharp increase in the concentration within 10 hours, reaching a maximum value of nearly $0.036\,\mathrm{mol\%}$ after about 24 hours of constant gas injection. After a refilling period of nearly 9 hours, the gas measurement resumes at a value of about $0.025\,\mathrm{mol\%}$, indicating a decline in methane and a very probable decay of microbes. During the refilling period, the probability is high that the decay of microbes begins in this phase. CH_4 continues to decline at a constant rate for approximately 25 hours. The curve begins to flatten out after approximately 62 hours, and it seems to stabilize at around $0.01\,\mathrm{mol\%}$, which was also the last value recorded during gas injection. The growth occurs at a very high rate within a short time period. The decline becomes the dominant phase shortly after reaching the maximum methane value. The decline continues for the vast majority of the experiment at an initially higher rate, ultimately leading to a flattening out of the curve.

Analysis of methane and microbial cell development

The experiments revealed a relation between microbial growth and methane production. The levels of the microbial density and absolute cell number do not merely indicate the potential of the microbes to consume hydrogen and carbon dioxide, but also the level of consumption and the probable quantities produced. At low cell and density levels, less hydrogen is consumed and the increase in microbial population begins at a low rate. When the microbes increase in population number, the consumption will rise, leading to an accelerated metabolism, and a higher amount of produced methane. The growth begins to slow down, which is marked by the reduced growth slope, a stabilization in the cell numbers, and the peak in the methane values. This peak in

methane and the stabilization imply that the microbial number has reached a maximum value and it cannot increase any further despite a continuous supply of gaseous substrates. During the time of relative stabilization in the microbial number, the quasi-stationary phase, the microbial activity seems to be declining. After transitioning from the quasi-stationary phase to the decay phase, the microbial density decreases noticeably, as does the methane. The decay behavior of the microbes appears to be steady. Despite this continuous decline, a reduced number of microbes still remain active as indicated by the measured methane. Lower microbial activity yields lower methane production. Considering the duration of the experiments, the decay phase appears to be dominant during most of the experiment. The decline in methane only appears to be linear for a relatively short period of time after the beginning of this period. In the later experimental stages, the reduction in the methane generation appears to level off and approach a stabilized value. Despite the sufficient availability of H_2 and CO_2, refilling the syringes and resuming the injection, net microbial growth is only dominant at the beginning of the experiment. A renewed injection does not increase the growth rate and does not lead to an overall net growth in population number. The injection of fresh gas rather supports the existing maintenance of the microbes and decreases the decline effect. The microbial activity is kept at a low level, leading to a longer stabilization of methane production.

One significant influencing internal factor is the quality of the microbes (indicated as density in $\mathrm{cells/m^3}$). The initially available number of cells provides a first hint at the potential microbial perfor-

mance and methane generation. When the overall initial density is in the range of 10^{13} cells/m^3, this lower cell number appears to have a brief lag phase and requires more time to trigger its metabolism and to increase its number, compared to initial values ranging from 10^{14} to 10^{15} cells/m^3. The level of this initial value also indicates the quantity of produced methane and the microbial and methane development in the early stages of the experiment. Figures 3.5 and 3.6 show the microbial data at the same temperature (40 °C). The data of the microbes in the first experiment is 10^4 and in the second experiment 10^5 cells. This difference in quality is detrimental to the methane generation, as the maximum CH_4 value in the first experiment is $0.09\,\mathrm{mol\%}$, compared to $0.32\,\mathrm{mol\%}$ in the second experiment. The second experiment has higher density and cell values, resulting in a larger and quicker growth. This leads to a higher rate in metabolism, hydrogen consumption and methane generation. Additionally, the maximum methane value is reached at a later time in the experiment.

A vital external influencing factor is the surrounding temperature. The experiments imply that the set temperature impacts the microbial activity, the level of methane production and the maximum values. The third experiment was conducted at room temperature, and the methane production stabilizes at nearly $0.09\,\mathrm{mol\%}$ and remains at this level for nearly the rest of the experiment. No net microbial growth is visible at the beginning; the entire experiment is dominated either by stabilized cell values or by microbial decay. The final microbial values are below the initial ones. When the temperature is greater than 40 °C, the growth rate is higher and the respective maximum values are reached earlier. This observation is

also noticed in the produced methane. The maximum CH_4 concentration reaches higher levels in a shorter period of time compared to the experiment at room temperature. An increase in temperature also increases the decay behavior, as indicated in the decline after reaching the maximum values. At over 60 °C, the growth rate is much higher, implying an even steeper initial microbial growth and the maximum methane values are reached earlier. On the other hand, the microbial development over time is more volatile as the temperature increases. An increase in the temperature appears to enhance the inconsistency of microbial development with time. This makes a precise estimation of the microbial number difficult.

3.4 Numerical modeling of microbial growth in micromodels

Setting up the numerical model of the microbial experiments is accomplished using the open-source numerical simulator $DuMu^X$. This model was developed in the "2pnc" model within the "porousmediumflow" path. This model contains the equations for the flow of phases through porous media. The numerical continuum two-dimensional micromodel consists of evenly discretized grid cells in the x-direction (50 cells) and y-direction (9 cells). Each grid cell has an edge length of 1 mm. The 50 cells in x-direction represent the length of 5 cm and the 9 cells in y-direction the micromodel width. The gap (thickness) of 50 μm between the two glass layers is also inserted. This one-layer, two-dimensional simulation model consists of 450 grid cells. Inside the "params.input" file, input files for porosity and permeability in x and y direction generated in

Comsol Multiphysics were inserted. Each value was assigned to an element to replicate the micromodel properties. The numerical micromodel is shown in Figure 3.9.

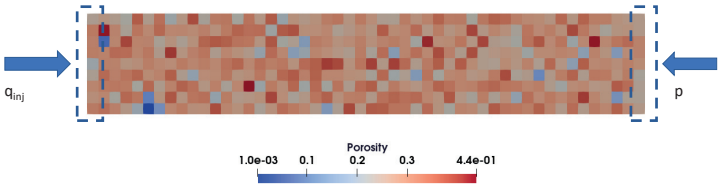

Figure 3.9: Numerical model of the linear circle microchip during the injection of the gas mixture (elements displaying the porosity ϕ)

The initial boundary conditions were set to Neumann for all boundaries of the micromodel. For the upper and lower boundary, these are designed as no-flow Neumann boundaries Γ_N, while a constant injection rate into the micromodel from the left side is set. The micromodel outlet is designated as a Neumann boundary during the flow of gas through the micromodel. At certain times during the experiments, the gas syringes had to be refilled to resume the injection procedure, making a shut-in of the micromodel unavoidable. In these phases, the valves connecting the micromodel to the syringes are closed, and the backpressure regulator did not further vent out gas. In the numerical simulation, this situation leads to the micromodel inlet side being designated as a no-flow Neumann boundary and the outlet is a Dirichlet boundary Γ_D with a constant pressure of 5 bar(g) acting on it. Each grid cell is initialized with the parameters listed in Table 3.1.

The initial water concentration (liquid and gaseous) is determined

Table 3.1: Numerically initialized parameters

Parameter	Value	Unit
Pressure (p)	500000	Pa
H_2	0.8	mole-fraction
CO_2	0.2	mol-fraction

by the thermodynamic equilibrium in DuMu^X. One additional input parameter is the initial microbial number (N_i), determined from the image analysis in each analyzed experiment.

Inflow modeling

The wet H_2-CO_2 gas mixture is injected at a constant rate into the left side of the microchip. The injection flux will spread across the height and the width of the chip so that the entire inlet area of the micromodel is flooded by gas. Each boundary element can have a locally specific injected quantity, which is dependent on the local permeability. An element with higher permeability will have a higher local flux than one with low permeability. This influx distribution is accounted for in the numerical model by defining a term called injectivity I, which is the sum of each local injectivity-element i at the inflow boundary:

$$I = \sum_i K_\mathrm{i} \cdot {\lambda_\mathrm{g}}^i \cdot A_i \tag{3.1}$$

where K is the permeability in the x-direction [m^2], λ_g is the gas

mobility [$\frac{1}{\mathrm{Pa \cdot s}}$] and A is the area [$\mathrm{m}^2$].

For the calculation of the distributed inflow of the inflowing stream, the injectivity is taken into this calculation as shown in Equation 3.2:

$$q_j^{\kappa} = \frac{c_j^{\kappa} \cdot q_{inj} \cdot K \cdot \lambda_g \cdot A_i}{I} \tag{3.2}$$

where $\mathrm{q_j^{\kappa}}$ indicates the inflow fraction of the component κ in its liquid or gaseous phase (j) [$\frac{\mathrm{mol}}{\mathrm{s}}$], $\mathrm{c_j^{\kappa}}$ stands for the fraction of the inflowing component in its respective phase, $\mathrm{q_{inj}}$ denotes the total molar inflow rate [$\frac{\mathrm{mol}}{\mathrm{s}}$] and $\mathrm{A_i}$ is the area of the element [m^2].

Outflow modeling

On the outflow side, the stream consists of liquid and vapor and three other gas components (H_2, CO_2, CH_4). The outflowing rate and the outflowing composition for each component need to be calculated at the outflow boundary through the liquid and gas flux. The gradient of the liquid and gas flux is calculated in each element separately and then accumulated ($\nabla^{\mathrm{j}}_{\mathrm{p,total}} = \sum_{\mathrm{i}} \nabla^{\mathrm{j}}_{\mathrm{p}}$). Using the gradient, the flux is calculated for every component using Darcy Law and then multiplied by the outflow area as shown in Equation 3.3:

$$q_{o,j}^{\kappa} = K \cdot \nabla_p^j \cdot \lambda_j \cdot \rho_{m,j}^{\kappa} \cdot A \tag{3.3}$$

where $\mathrm{q_{o,j}^{\kappa}}$ denotes the outflowing rate of the component κ in either liquid or gas phase j [$\frac{\mathrm{mol}}{\mathrm{s}}$], and ρ_m^j is the molar density of the outflowing phase. The result is the outflowing rate for each

phase-specific component.

Modeling of spatial limitation within the pore space and consideration of a maintenance coefficient

During growth, the microbes accumulate within the pores over time. As the growth behavior is dominant in the early experimental stages, an exponential increase in the microbial number leads to increased microbial consumption of the substrates. A higher microbial number leads to increased competition among the cells for the nutrients and substrates. As the pore space remains unchanged, the growing cell number leads to a declining spatial availability for the available microbes to grow and for new microbes to be formed. Some cells will be closer to the gas-liquid interface while others will have a further distance to it. The confined pore-space is a limiting factor that can be filled with microbes at a maximum number ($\mathrm{n_{Max}}$). When this maximum number is reached, the microbial activity would be at its highest peak. To account for this spatial restriction, a limiting function L is defined, which is a function of the current microbial (n) and the maximum microbial number ($\mathrm{n_{Max}}$) (Equation 3.4).

$$L = 1 - \left(\frac{\mathrm{n}}{\mathrm{n_{Max}}}\right)^{\mathrm{k}} \tag{3.4}$$

where k is a variable exponent that determines the shape of the curve and the range of L is

$$0 \leq L \leq 1 \tag{3.5}$$

At the beginning of the experiment, the microbial number is low. At

this stage, the limiting function will have its highest value, which would be closest to one. This makes the growth term large and dominant in the population development. The rise in the microbial population will lower the limiting function, thereby reducing the dominance of the growth function. In the simulation model, the maximum population will always remain below the inserted peak value. After attaining the peak, the cell number and cell density would remain constant for the rest of the experiment as the growth and the decay term balance each other. This limiting function is included in the growth term of the Double-Monod model (Eq. 3.6)

$$\frac{dn \cdot S_w \cdot \phi}{dt} = (L \cdot \psi_{\max}^{growth} \cdot \frac{c_w^{H_2}}{c_w^{H_2} + \alpha_{H2}} \cdot \frac{c_w^{CO_2}}{c_w^{CO_2} + \alpha_{CO_2}} - b) \cdot n \cdot S_w \cdot \phi \tag{3.6}$$

and in the bioreactive kinetic equation (Equation 2.21) for the production of methane (c.f. Equation 3.7).

$$q_{bio}^{\kappa} = \gamma^k \cdot \frac{(L \cdot \psi^{growth} + m)}{Y} \cdot n \tag{3.7}$$

The development of a linear behavior with a decay rate proportional to the microbial population has been implemented into numerical models and discussed in literature [24]. However, microbial growth and decay are incorporated in the Double-Monod model. Depending on the magnitude of the parameters, the mathematical equation can have two results: the population will permanently increase in a dominating growth rate or it will decline when the decay rate is dominant. As the timely dominance of growth and sub-

sequent decay cannot be effectively reflected in the current model, a workaround for the numerical replication of the declining cell number is necessary. A linear dry-out function for the aqueous phase containing the microbes is established to simulate an evaporation process. In the experiments, an evaporation of liquid inside the micromodel appears realistic as the elevated temperature triggers this process. Therefore, a drying-out function f_w is defined and implemented for the liquid phase in DuMu^X (Equation 3.8):

$$f_w = -e \cdot \phi \tag{3.8}$$

where f_w is the dry-out rate $[1/s]$ and e is the drying coefficient.

3.5 Results and discussion

The experiments were conducted in such a way that the micromodel had a relatively constant two-phase saturation. The analysis of the results includes evaluating the pictures taken of the entire microchip and selected positions, each with the size of a determined representative elementary area.

3.5.1. Determination of Representative Elementary Area (REA)

The assembled tiles from the five-fold magnification lens produced an image covering the entire area of the micromodel, consisting of 19826920 pixels. One single 40-fold magnification picture had a dimension of 359840 pixels. The ratio of the 40-fold picture to the entire microchip was approximately $2.8371 \times 10^{-4}\,\%$, indicating that the size of one 40-fold magnified image covered only $0.000\,283\,\%$ of

the total micromodel. As this value is an extremely small fraction of the total microchip, it increases the probability that the picture acquired at 40-fold magnification is not representative for the entire microchip. The observation at the selected position might not be similar to another one. This uncertainty required the determination of a minimum area which can be regarded as representative of the entire micromodel. The result of this process is a representative elementary area (REA). This concept is similar to the representative elementary volume for a finite volumetric sample applied to a two-dimensional picture. To determine the REA, the analysis began at a fixed point shaped as a square in the middle of the lithographic mask. In total, 50 increments of an increasing width of 100 pixels each in height and length were investigated. The boundary is the maximum height of the area of investigation (AOI) (2116 pixels), at which the mean porosity value stabilized. 9 positions were distributed across the micromodel and analyzed to obtain a REA. The development of the AOI is shown in Figure 3.10.

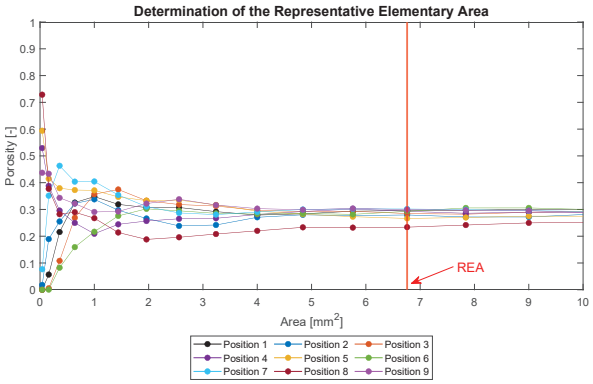

Figure 3.10: Representative elementary area of the microchip

The shape of the curve in the very small porous areas is characteristic of their macroscopic effects. In this analysis, the values stabilized at approximately $5\,\mathrm{mm}^2$. To ensure stable measurements and to further reduce the influence of heterogeneities, a slightly larger area was selected. The average porosity value stabilizes at around 0.276 at an area of approximately $6.8\,\mathrm{mm}^2$, which was selected as the REA. The dimensions of the REA are $2.6\,\mathrm{mm}$ by $2.6\,\mathrm{mm}$. The representative elementary area covers a larger area of the micromodel than the 40-fold magnified images, therefore it was more representative of the entire chip. These dimensions were used as the areas in which the microbial number developments are analyzed.

To obtain a broad number of representative areas, 15 areas with the REA dimensions across the microchip were selected. Care was taken that the areas were selected randomly, showing areas with higher and lower microbial activity. The vicinity to a gas-liquid interface was also an important factor in selecting the AOIs. An example of the visual segmentation of the microchip is depicted in Figure 3.11, indicated by the green-colored rectangles.

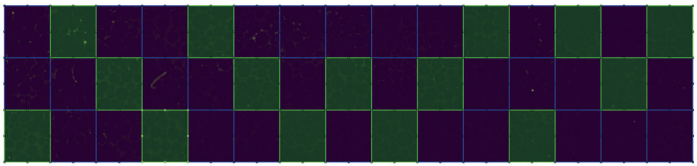

Figure 3.11: Areas of investigation (green rectangles) examined, each with the size of the representative elementary area

15 (green) out of the 45 rectangles were analyzed for the respec-

tive microbial number, this value was multiplied by a factor of 3 to project the cell number onto the total micromodel area. Previous experiments have also indicated that the determined microbial number in one position only indicated the number in the upper visible layers, which was noticed on the picture. Across the thickness of the microchip, the total cell number was nearly seven times the initial value. Therefore, the total cell number was also multiplied by a factor of 7. The size of an average microbial cell ($\sim 1 - 10\ \mu\mathrm{m}$) was an important characteristic which was considered in the calculation of the microbial number. The size of the images revealed that the size of a single pixel is nearly $5\ \mu\mathrm{m}$. The microbial observation indicated that the average size of a single cell remained stable and this facilitated the counting of the cell number. One cell fitted into one pixel. If a pixel was above the average color threshold value, described in Chapter 3.2.4, then this one pixel contained one single cell. This facilitated the cell counting process and correlated the number of cell-containing images to absolute cell numbers.

3.5.2. Correlation of experimental and simulation results

To replicate the experimental data, the simulation structure had to be adapted accordingly to achieve an acceptable match between the numerical and experimental results. The adaptable parameters in these simulations are the microbial growth parameters, which vary depending on the surrounding conditions and the microbial quality. In the course of the simulations, these parameters were tuned to achieve an acceptable match between the datasets for the microbial number and the development of the methane concentration. The calibrated parameters are presented in Chapter 3.5.3.

Experiment 1

The matched numerical representation for this experiment (T = 40 °C) is shown in Figure 3.12.

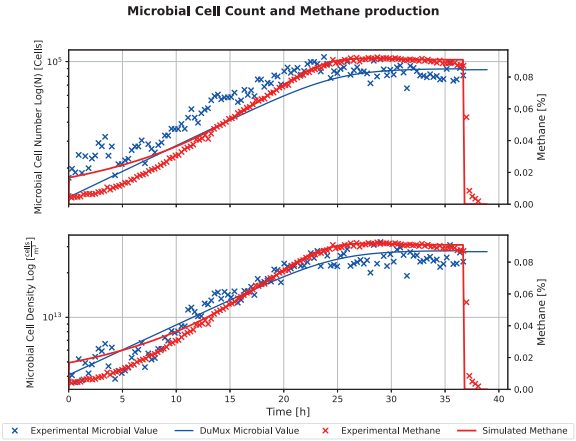

Figure 3.12: Matched experimental and numerical development of the microbial cell count and the methane production

The Double-Monod model states that microbial growth occurs in the presence of the gaseous H_2 and CO_2 substrates. This growth is governed by the maximum growth rate, the half-velocity coefficients and the initial decay rate. In the initialization of the simulation, the microbes at their initial number are inside the micromodel, and the hydrogen and carbon dioxide concentrations are also available in the ratio 4:1. In the first simulation timestep, no methane is generated. This changes with the second timestep, when the first moles of the gas are consumed, and methane is produced. The first time steps reveal the largest increase in methane production within a very short period of time. In the limit function for the bio-reactive

kinetic equation and the Double-Monod growth model, the limit function is close to the value of 1. This leads to the growth term being dominant in these early experimental stages. This explains the sharp increase in methane to approximately $0.02\,\mathrm{mol\%}$ in the first hour of the experiment. After this sharp increase, the methane curve begins to level off, the inclination is reduced and the simulated methane curve approaches the experimental values. As the values increase, the limit function becomes smaller, indicating a steadily slowed approach towards the fixed maximum values. The maximum simulated methane value of $0.09\,\mathrm{mol\%}$ is reached after nearly 26 hours. Around this maximum concentration, the limit function is approaching its lowest value, reducing and slowing down growth, eventually leading to a stabilization. Afterwards, the decrease in the simulated methane concentration becomes dominant. Analyzing the microbial values, the values start off with an uninterrupted linear increase. As the maximum value of nearly $2 \cdot 10^5\ \mathrm{cells}$ is gradually approached, the increase begins to diminish and eventually stabilizes. At the beginning of the experiment, the limit function is at its highest value, making the growth term dominant. The growth diminishes as the maximum number is gradually reached. This leads to an equilibrium between growth and decay and eventually to a dominance of decay. In both plots, the linear shape of the microbial curve reveals the exponential growth phase. The exponential growth ends and decelerates when the curve begins to flatten out, and the overall stationary phase is entered when the curve remains flat and has no slope.

Experiment 2

The same matching procedure is applied to the second experiment

which lasted longer than the first. In this case, the microbial decay and its effect on methane production are stronger. The matched simulated values and the experimental results are shown in Figure 3.13.

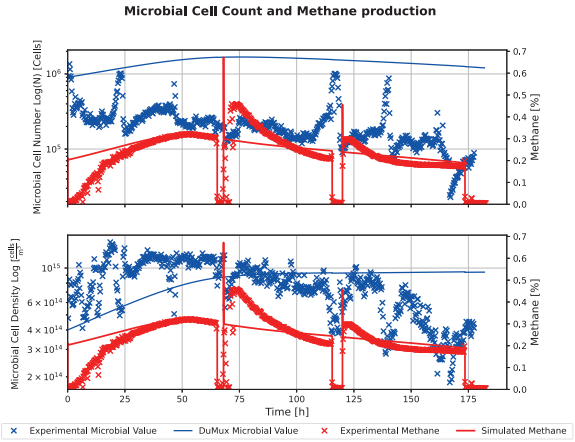

Figure 3.13: Matched experimental and numerical development of the microbial cell count and the methane production (40 °C)

The analysis of the overall microbial development indicates a large volatility in the absolute numbers and the phases are not clearly distinguishable. Only the overall trend that the microbial number declines in the long run is clearly observed in the image analysis. For these reasons, the gas chromatographic measurements are used as a primary reference for the matching procedure. Nevertheless, the simulated microbial number increases exponentially for approximately 60 hours before reaching a quasi-stationary phase lasting nearly 20 hours. During the rest of the experiment, microbial decay dominates. Similarly to the first experiment, a strong rise in

the methane concentration occurs in the first time steps before it flattens out and gradually approaches the experimental values after approximately 45 hours, reaching the peak value after nearly 50 hours. The methane values begin to decrease earlier than the microbial number. The methane peak value marks a turning point in the curve, signaling the beginning of the decline phase. With the adjusted parameters, the methane value at the end of the second and third injection phase stands at approximately $0.21\,\mathrm{mol\%}$ and at $0.18\,\mathrm{mol\%}$, respectively. These values are very close to the measured concentrations, revealing an acceptable match between those datasets. After surpassing the respective peak values, the simulated microbial number enters a continuous decline phase while the methane initially decreases sharply before leveling off.
The simulated methane was estimated at the outflowing boundary of the micromodel during the entire simulation run. During the refilling phase, the same system pressure of 5 bar(g) acted on the micromodel, leading to a temporary static condition. When the injection process resumed, the methane, which was produced in the micromodel, was transported to the outflow and measured, resulting in the brief peak in the concentration. Therefore, the simulated methane reflects the outflowing quantity at a constant system pressure during the dynamic state of the experiment.

Experiment 3

In the previous experiments, no clear microbial lag phase was noticed in the images. Simultaneously, the gas measurements recorded methane at very low values in the very early stages of the experiments. The modeled and the experimental values for the experiment at room temperature are depicted in Figure 3.14.

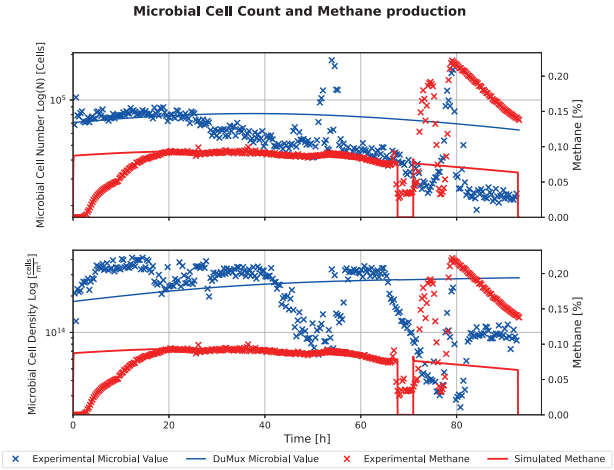

Figure 3.14: Matched experimental and numerical development of the microbial cell count and the methane measured (25 °C)

While the experimental microbial number remains relatively steady during the first 20 hours, the simulated values indicate a small linear increase in the same time period. The quasi-stationary phase is also relatively short and the subsequent decay phase is dominant for the rest of the experiment. The plot indicates that the decline is nearly exponential. The simulated microbial values decline nearly parallel to the experimental numbers and the final values are below the initial values, marking an acceptable match between simulation and experiment. The simulated methane values reveal an initial sharp increase in the concentration. It flattens out extremely quickly, and reaches the maximum value just 10 hours after the beginning of the simulation. Analogously to the previous measurements, the methane curve decreases after reaching the maximum value. This

parameter was reduced because the lower temperature limited microbial activity and methane production. This implies a slower decline and the flattening out of the curve appears to be prolonged and extended. Contrary to the previous experiments, this simulation can provide a better match between the microbial values than for the gas measurements. This match also indicates that the bioreactive kinetic equation does not accurately represent a constant maximum gas value, which is maintained for a longer period of time and occurs simultaneously with the microbial decay.

Experiment 4

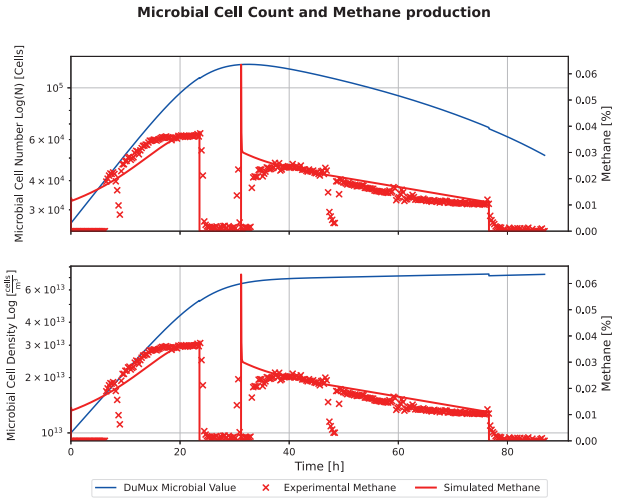

Figure 3.15: Matched experimental and numerical development of the microbial cell values and the methane production (62 °C)

In this experiment, the matching was performed solely based on the gas measurements, which is shown in Figure 3.15. The simu-

lated values demonstrate an initial strong increase in the methane concentration in the first time steps before the increase begins to slow down. The simulated curve intersects the measured values just before reaching the maximum value of nearly $0.036\,\mathrm{mol\%}$ after nearly 20 hours. The simulated and the experimental values imply a short quasi-stationary phase and a subsequent nearly linear decline. The curvature of the methane curve in the decline phase could not be completely matched but the final simulated value stands at $0.011\,\mathrm{mol\%}$ compared to the measured $0.0104\,\mathrm{mol\%}$, a deviation of about 5%. The microbial values are a best guess which were used to attain the match in the methane values. The initial exponential growth leads to a peak number within a shorter time period. The quasi-stationary phase is also significantly shorter than in the previous experiments and the following decline in both datasets has a higher magnitude as well.

3.5.3. Calibrated microbial kinetic parameters

In total, four microbial growth experiments in quasi-two-dimensional micromodels were conducted and compared to numerically developed replications of the microbial growth process and methane production. To reduce the number of variables to be matched, the half-velocity coefficients for hydrogen and carbon dioxide were taken from a subsurface hydrogen storage simulation in literature. These values were $\alpha_{\mathrm{H_2}} = 8.99 \cdot 10^{-8}$ and $\alpha_{\mathrm{CO_2}} = 5.4 \cdot 10^{-6}$ [24]. The following Table 3.2 lists the calibrated parameters, which provided the best fit with the experimental observations.

In every numerical simulation, the drying-out rate was also adjusted

Table 3.2: Matched modeled parameters for the best replication with the experimental results

Model parameter with symbol	Unit	Experiment 1 (40 °C)	Experiment 2 (40 °C)	Experiment 3 (25 °C)	Experiment 4 (62 °C)
Maximum growth rate $\psi_{\text{growth}}^{\max}$	$\frac{1}{s}$	$2.4 \cdot 10^{-5}$	$6.5 \cdot 10^{-6}$	$7.0 \cdot 10^{-6}$	$3.4 \cdot 10^{-5}$
Yield Y	$\frac{1}{\text{mol}}$	$1.77 \cdot 10^{11}$	$1.5 \cdot 10^{11}$	$4.2 \cdot 10^{10}$	$2.35 \cdot 10^{11}$
Maintenance rate m	$\frac{1}{s}$	$7.2 \cdot 10^{-5}$	$7.5 \cdot 10^{-6}$	$1.5 \cdot 10^{-5}$	$7.3 \cdot 10^{-6}$
Decay rate d	$\frac{1}{s}$	$2.0 \cdot 10^{-6}$	$3.0 \cdot 10^{-6}$	$4.7 \cdot 10^{-6}$	$1.4 \cdot 10^{-5}$

to match the microbial number during the decay phase. Assuming the extremely confined space inside the microchip and the set experimental temperature, the experimental maximum and the final microbial cell number were used as reference points for the parametrization of the drying-out rate. The matching process provided the following values for each drying-out rate of the liquid phase:

- Experiment 1: $2.0 \cdot 10^{-5}$ $1/\text{s}$
- Experiment 2: $2.1 \cdot 10^{-2}$ $1/\text{s}$
- Experiment 3: $7.0 \cdot 10^{-3}$ $1/\text{s}$
- Experiment 4: $5.2 \cdot 10^{-2}$ $1/\text{s}$

The numerical matches of the experiments conducted indicate different microbial growth behavior and methane production patterns when the surrounding temperature changes. When the temperature increases, the maximum growth rate $\psi_{\text{growth}}^{\max}$ increases as well. Comparing the four experiments to each other, $\psi_{\text{growth}}^{\max}$ at 25 °C is at its lowest value of $1.9 \cdot 10^{-5}$ $1/\text{s}$ and gradually increases to $9.8 \cdot 10^{-5}$ $1/\text{s}$ at 62 °C, a nearly five-fold increase. All the obtained

values still remain in the range of 10^{-5} 1/s. The temperature influences the level of microbial growth with a higher temperature leading to a higher growth rate and vice versa. This observation is in alignment with literature, establishing a connection between the temperature and the growth rate [91]. For the methanobacterium thermoautotrophicum, the same family as methanococcus thermolithotrophicus, the specific growth rate doubled at an increase of every 10 °C, with the highest growth rate at 65 °C. This behavior was also observed in the numerical matching process. The temperature also influences the doubling time in the microbial population. As the temperature increases from 30 to 62 °C, the hours needed for the microbes to double in population decreased from 7 to just one hour, implying that a higher temperature is of benefit to microbial growth up to its optimum temperature [44].
Besides the growth rate, the decay rate also appears to be influenced by the temperature. When the growth rate increases, one result is a higher microbial number. When the decay is proportional to the microbial number, a low microbial number results in a low decay rate. An elevated population will increase the total decay rate as a higher number of microbes are competing for the nutrients and gaseous substrates. The development of the microbial number is directly governed by the temperature-dependent growth rate. At room temperature, the matched decay rate stands at $3.0 \cdot 10^{-6}$ 1/s. Close to the optimum microbial temperature, this matched value increases to about $2.0 \cdot 10^{-5}$ 1/s. However, the decay rate cannot always be reliably matched with the experimental results, as the decay rate for the first experiment is close to the value obtained for room temperature. This implies that other factors contribute to the microbial decay or it could also be related to matching uncertainties.

In this analysis, the calibration of the drying-out rate was critical because it had the largest impact on the microbial decline. In this way, the drying-out function contributed to the microbial decay.
The yield parameter also varies in each of the four experiments. The yield states the amount of cells produced per one mole of methane formed. At room temperature, the yield stands at $4.2 \cdot 10^{10}$ $1/\mathrm{mol}$. This value increases with temperature, as the matched value attains about $1.77 \cdot 10^{11}$ $1/\mathrm{mol}$ at 40 °C and $2.35 \cdot 10^{11}$ $1/\mathrm{mol}$ at 62 °C. This behavior appears to be dependent on the temperature because the matched yield parameter increases with temperature. The yield also influences the maximum concentrations of methane. In the bio-reactive kinetic equation, the yield is in the denominator, resulting in a lower methane concentration as the yield increases and vice versa. This observation was described by Schönheit et al. (1980), in which an unlimited supply of H_2 and CO_2 for a potential unlimited methane formation resulted in an increase in the yield as temperature rose [91]. The numerically obtained values are in similar ranges as the experiments conducted in Karadagli and Rittmann (2005) and in Robinson and Tiedje (1984) at 37 °C [53, 89]. The obtained values are also close to the numerically determined yield values presented in the micromodel works of Strobel et al. (2023) [98].
No clear dependency on the temperature was noticed for the maintenance coefficient m. In previous works, this coefficient indicates the minimum level of microbial activity which the microbial culture uses for maintaining a minimum level of relevant cell functions and not for further cell development. Van Bodegom (2007) stated that the overall maintenance of microbes was influenced by the growth and decay parameters and that it was a dynamic process. Some

mentioned experiments analysis indicated that the determined yield was not constant in spite of assuming a constant maintenance [107]. This leads to a variety of remaining uncertainties surrounding the concept of microbial maintenance and the precise effect it has on the microbial cell number and potentially methane generation. However, in the performed microbial experiments, the value of microbial maintenance influences the overall level of methane generation during growth and in the subsequent stabilization. In the kinetic reaction, the maintenance coefficient will have the strongest influence in the quasi-stationary phase when no clear change in the microbial number is apparent. The maintenance value can also reduce the subsequent decay to account for the minimum required energy intake of the microbes. Nevertheless, a clear influence of temperature on the maintenance coefficient could not be drawn from the matching process.

Overall effect of temperature on growth parameters and methane development

The setting of the temperature acting on the microbial culture significantly influences the cell metabolism behavior, the growth and decay rate and the levels of cell numbers which can be attained. The velocity of the growth and the microbial numbers determine the quantities of hydrogen consumption and produced methane from cell metabolism. The numerical matching process revealed that some kinetic parameters are notably influenced by the selection of the surrounding temperature. For the growth rate, decay rate and the yield, the values are proportional to an increase or decrease in temperature. The maintenance rate and the half-velocity coeffi-

cients do not show a clear proportional behavior to the temperature. Adjusting these parameters impacts the level of produced CH_4, the time when the peak value is attained, the rate of decrease and the approximate stabilization level in the long-run when the microbial number decreases.

The temperature level influences the dry-out rates of the liquid phase in the porous media. The tendency reveals that a higher temperature leads to a higher dry-out rate and therefore a faster evaporation. When the evaporation increases, the small liquid volume will diminish, leading to a higher decline in the microbial cell number. Therefore, the decrease in the microbial cell number is the highest when the temperature is 62 °C. This also affects the methane production, as the higher cell decline results in increasingly less methane being produced. This is supported by the gas measurements which show the strongest decline at the highest temperature.

Limitations of matching process

Regarding the microbial population development, the concept of spatial limitation was introduced to account for the limited pore space in which microbes can grow. It has been observed in the experiments that the microbes grow until they attain their maximum number before beginning to decay and the overall population declines. The experiments have revealed that such maximum densities are usually attained one single time. Despite a re-injection of fresh new gas, no renewed growth was observed. This observation was supported by the continued decrease in the detected methane concentration in the gas chromatograph. Eventually, this curve began to stabilize at a long-term minimum value. The phase of stabilized gas values points towards a minimum cell number,

which consumed hydrogen and carbon dioxide as an energy source to maintain its endogenous functions and continues to produce methane as a byproduct of this process. This microbial cell number level could remain nearly unchanged for an unknown period of time and continuously produce methane without increasing neither in cell size nor in population. In this case, the gas-liquid transfer of gaseous substrates needed to be considered as another limiting factor. When the growth of the cell number reached its maximum, the gas-liquid transfer also reached its maximum. When the microbes reached their minimum level, the transfer stabilized at a minimum value. This allowed for an interface transport that was high enough to maintain a minimum metabolism function, leading to minimum methane production. These limitations in microbial growth have been mentioned previously ([91, 100]). The limitation and reduction in substrate transfer require closer examination to understand its contribution to microbial development in the future.

3.6 Summary

In this chapter, the described experimental approach and procedure enabled the observation and quantification of the microbial number inside the micromodel and the measurement of methane produced by biochemical reactions in a H_2-CO_2 environment. A numerical simulation model was established to replicate the microbial experiments using a newly introduced microbial maintenance rate and a limiting function to account for the restricted space available for microbial growth. The growth parameters were obtained by adjusting the numerical model to attain an acceptable match with the experimental microbial and methane values. The key findings of

this chapter are:

- The experimental setup was an easy-to-handle assembly that enabled a safe preparation and injection of a media-microbial mixture and the H_2-CO_2 into the micromodel in anaerobic conditions. By sterilizing the equipment and using nitrogen, the entire system was kept oxygen-free and safely pressurized. The use of the high-resolution microscopic camera and its software provided the opportunity to observe the microbial cell development with time. The assembled gas chromatograph reliably provided gas measurements of the methane during the microbial development.
- A MATLAB tool, which had been previously developed to observe waterflooding processes in oil-saturated micromodels, was adapted to assess the microbial number inside the liquid pore spaces over time and plot this development with the methane concentration. Considering the vertical microbial accumulation in the chip and the limited area analyzed, multiplication factors of 7 (depth) and 3 (areal) were used to project the cell distribution onto the entire micromodel domain.
- Four different microbial growth experiments were performed at 25, 40 and 62 °C. The microbial number was observed and the methane concentration was measured. The microbial cell development was put into context with the methane development. After an initial growth and a quasi-stationary phase, the microbial number began to decline and attained a final value. The final methane value stabilized at a respective constant value in the long run.

- A numerical simulation model was set up to replicate the microbial growth experiments at three different temperatures. An optimal match between the simulated and experimental values was attained by amending the growth and decay parameters. For some parameters, a clear dependency on the temperature was noticed while other parameters seemed to be less influenced by temperature. Already slightly elevated temperatures at approximately 25 °C revealed biochemical processes at a low magnitude.
- The concept of spatial limitation was a good method to incorporate an upper boundary for microbial growth, as the available pore space provided is limited and unlimited growth is improbable. The limitation in microbial growth also restricted the biochemical methane production as it declines after attaining its peak. In the long run, the stabilized methane indicates a constant biochemical process and microbial activity at a low level. Gas-liquid transfer can also restrict microbial growth and requires further analysis.

Chapter 4

Examination of existing subsurface natural gas and prospective hydrogen storage capacity and productivity

4.1 Aspects to consider during a conversion

The conversion of an existing underground gas storage site to a potential hydrogen storage requires a preceding precise examination and analysis of multiple characteristics and parameters. As the goal is to store hydrogen, an investigation into its compatibility with the existing technical infrastructure, the differences between natural gas (NG) and hydrogen parameters and the effects of hydrogen molecules on the storage rock and caprock is necessary. The characteristics of assessing integrity features were reviewed in Chapter 2. The suitability of storing hydrogen in the existing storage site in the future is also determined by analyzing the potential capacity and withdrawal performance.

4.2 Gas characteristics

Hydrogen has many characteristics that differ fundamentally from natural gas. As methane makes up the largest composition of natural gas and for reasons of simplification, natural gas is assumed to be 100 % methane. Some of the distinct parameters characterizing the

two gases are molar weight, calorific value, density, compressibility, viscosity and the Joule-Thomson effect. Hydrogen's energy density results in an increased amount of space to store the same amount of energy as methane. These differences lead to varying energy contents in a designed storage space. Maximum injection or production rates between hydrogen and methane (CH_4) will also have different levels. The following Table 4.1 provides a brief overview of selected parameters highlighting the differences between hydrogen and methane ([16, 60, 88, 105, 112]).

The properties of hydrogen strongly differ from the property values of methane at surface and at subsurface conditions. One of the most important parameters describing the behavior of a gas at real conditions to its ideal conditions is the compressibility factor, or z-factor. At subsurface conditions, the gas volume will be different from surface conditions, because it is subject to higher pressures and temperatures. As pressure increases and temperature changes, the increasing gas pressure results in greater densities. Describing and calculating the z-factor is usually conducted with correlations relating the pressure to the volume of gas, known as Equations of State. The Equation of State (EoS) sets up a relationship between pressure and volume by factoring in the temperature, molar volume, and gas-specific properties. One of the most commonly used methods to determine the z-factor is utilizing the Standing and Katz diagram, developed in 1944. This diagram is used to determine the z-factor of petroleum gases based on the gases' critical properties (pressure, temperature) and the parameters of the surrounding temperature and pressure conditions. Based on the Standing-and-Katz chart, the Hall-Yarborough method was derived as an iterative approach to

Table 4.1: Gaseous characteristics between hydrogen and methane

Parameters	unit	hydrogen	methane
Volumetric calorific value	[kWh/m^3]	3.13	11.1
Mass calorific value	[kWh/kg]	150000	50000
Molecular weight	$[\frac{\mathrm{g}}{\mathrm{mol}}]$	2.016	16.043
Compressibility factor	[-]	above 1	below 1
Density at standard conditions (20 °C)	[g/L]	0.0826	0.657
Viscosity at standard conditions (20 °C)	$[10^{-5}\ \mathrm{Pa \cdot s}]$	0.88	1.1
Molar heat capacity	$[\mathrm{J/(mol \cdot K)}]$	28.836	35.7
Critical temperature	K	33.24	190.85
Critical pressure	MPa	1.298	4.639

determine the z-factor for hydrocarbon gases [110]. Assuming that natural gas consists primarily of methane, the z-factor of natural gas can be calculated using the Hall-Yarborough correlation. As this method was developed based solely for hydrocarbon gases, its application is limited to this group. The z-factors for hydrogen cannot be determined with the conventional Hall-Yarborough method, unless significant reparametrization is performed due to the differences in properties. When a gas consists of a wide range of components, which might include non-hydrocarbon components, then cubic Equations of State are to be used to determine the gas density and thus the z-factor. Out of many available EoS, one of the most common EoS was developed by Peng and Robinson in 1976 [82]. It is primarily used in chemical and petroleum engineering to predict phase behavior. It is expressed in terms of the components' acentric factor and critical properties of the gas. It also takes into account binary interaction coefficients between the gas components. The equation in its standard form is shown in the following Equation 4.1.

$$p = \frac{R \cdot T}{V_m - b} - \frac{a \cdot \alpha}{V_m^2 + 2bV_m - b^2} \tag{4.1}$$

where R is the universal gas constant [$\mathrm{J}/(\mathrm{mol} \cdot \mathrm{K})$], T is the temperature [K], $\mathrm{V_m}$ is the molar volume [$\mathrm{mol}/\mathrm{m}^3$], a, b and α are model parameters. To calculate the z-factor of a gas, the EoS needs to be stated as a cubic form according to Z as it is shown in Equation 4.2:

$$Z^3 - (1 - B)Z^2 + (A - 2B - 3B^2)Z - (AB - B^2 - B^3) = 0 \tag{4.2}$$

using $A = \frac{\alpha a p}{R^2 T^2}$ and $B = \frac{bp}{RT}$ as the dimensionless parameters. Solving this cubic equation of state results in three potential values for z: one lower value, one middle value, and one upper value. Only the lowest and the highest values should be taken into consideration when determining the z-factor, as these lie within the acceptable range of the potential z-factor values.

The Peng-Robinson (PR) method has been mentioned as one of the commonly used methods and will be applied in the calculations presented in this work. The z-factors of hydrogen and methane at elevated temperatures and pressures vary significantly at subsurface storage conditions. The following Figure 4.1 depicts the z-factor curve for methane and hydrogen between 1 and 200 bar. Hydrogen's z-factors were calculated using the Peng-Robinson EoS approach [82] and the natural gas z-factors were determined with the Hall-Yarborough approach [110].

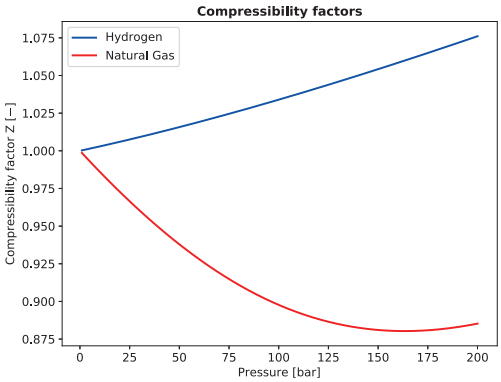

Figure 4.1: Curves of the compressibility factors for both methane and hydrogen (T = 65°C (338.15 K))

Figure 4.1 reveals differences in the behavior of the compressibility factors of methane and hydrogen. At surface pressure, both curves begin at a z-factor of 1, indicating ideal conditions. H_2 has a z-factor which remains permanently above the value of 1 as pressure increases. Its increase is slow, but it is nearly linear. The curve of the natural gas compressibility factor has a broad, asymmetrical U-shaped curve. Initially, the z-factor values are near unity, then they decrease to a minimum of nearly 0.86 at a pressure of about 160 bar before the trend reverses and the z-factor increases. The z-factor curve for natural gas indicates that the gas is more compressible. As the pressures increase, the gas is more compressed and occupies a smaller pore volume in the available space. In the case of hydrogen at higher pressures, the gas is less compressible and it does not occupy the available space as effectively. This leads to a lower volume of hydrogen being stored in the same space at the same

pressure compared to natural gas. Closer to standard conditions, the molecules in both gases are held together through weak London dispersion forces. These attractive forces form the intermolecular bonds between the molecules which keep the molecules together. Due to the weak strengths of these forces, the molecules are in a gaseous state. As the pressure increases, the molecules are forced closer together. The electron clouds of the molecules come closer together and begin to overlap, increasing the magnitude of repulsive forces. Due to the significantly smaller size of the hydrogen molecules, the extent of the molecular electron cloud is much smaller and approaches another electron cloud much quicker. This results in earlier and stronger repulsive forces and a smaller gas volume to be compressed, in particular hydrogen [15, 64].

The compressibility factors for hydrogen and natural gas have been shown to have different values and different behavior with pressure (Figure 4.1). The density and the viscosity of the gases are also properties that are dependent on pressure. Determining the viscosity and density developments with pressure is achieved using viscosity correlation models. The Lohrenz-Bray-Clark model is predominantly applied for hydrocarbon gases and their mixtures, or the Stiel-and-Thodos model is used to estimate the viscosity of non-polar, pure gases [65, 94]. Both models depict the viscosity development at medium to high pressures and require essential gas parameters, such as critical or pseudocritical properties (temperature, pressure) and the molar fractions of the components. The viscosity and density behavior for CH_4 and H_2 is shown in Figure 4.2.

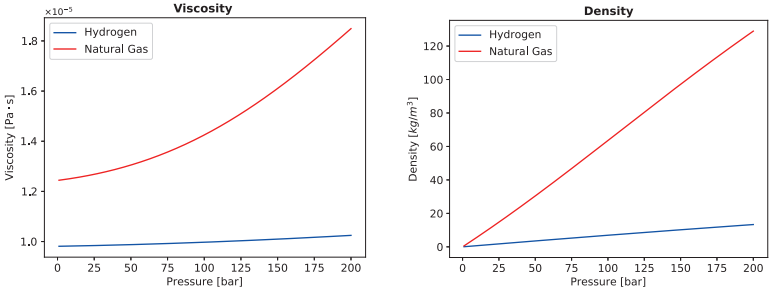

(a) Viscosity for hydrogen and natural gas dependent on pressure using the Stiel-and-Thodos and the Lorenz-Bray-Clark methods [65, 94]

(b) Density development for hydrogen (determined with the Peng-Robinson EoS) and natural gas (using Hall-Yarborough) dependent on pressure

Figure 4.2: Development of viscosity and density for hydrogen and natural gas as pressure changes (T = 65°C (338.15 K))

At atmospheric pressure, natural gas has a viscosity of about $1.25 \times 10^{-5}\,\mathrm{Pa \cdot s}$ and hydrogen approximately $0.9 \times 10^{-5}\,\mathrm{Pa \cdot s}$. As the pressure increases, the viscosity of hydrogen will increase just slightly to approximately $1.1 \times 10^{-5}\,\mathrm{Pa \cdot s}$, while the increase in the viscosity of natural gas is much steeper and reaches a value of $1.85 \times 10^{-5}\,\mathrm{Pa \cdot s}$ at 200 bar. This signals a higher dependency of natural gas viscosity on pressure than hydrogen. A similar behavior is noticed in the changes of density for both gases. At atmospheric pressure, the densities for both gases are at their standard values (ρ_{NG}=0.65 $\mathrm{kg/m^3}$, $\rho_{\mathrm{H_2}}$ = 0.0813 $\mathrm{kg/m^3}$). When the pressure increases, both densities increase linearly. At 200 bar, the hydrogen density will be approximately $16\,\mathrm{kg/m^3}$ and natural gas density at nearly $130\,\mathrm{kg/m^3}$. At 200 bar, methane has a density that is 12 times greater than hydrogen, making it a very dense gas at elevated pressures.

4.2.1. Subsurface working gas volume calculations

Knowing the compressibility factors is essential as they are critical to determining the volume of potentially stored gas. With the determined compressibility factors for hydrogen and natural gas, the working volumes for each gas can be determined. An approach to estimate available working gas volumes is based on the $\frac{p}{z}$-method. This is used in gas production to determine the gas initially in place in a reservoir by plotting the corrected pressure for z against the produced gas volume (described in [54]). The principle is that the term $\frac{p}{z}$ (for a gas at non-ideal conditions) is proportional to the amount of gas available inside the reservoir, and the extrapolation of the plot to $\frac{p}{z} = 0$ reveals the original gas quantity. To estimate the producible working gas volume, the volumes at maximum and minimum storage pressures are needed, and the respective z-factors need to be known. The $\frac{p}{z}$ method is extended with the real gas law ($\mathrm{p \cdot V = n \cdot R \cdot T \cdot z}$). Between the two pressure values, a change in the gas volume occurs that is reflected in the mole number n ($\Delta \mathrm{n}$). The real gas law is rearranged according to n and leads to $\mathrm{n = \frac{p \cdot V}{R \cdot T \cdot z}}$. As the reference values for R and T are often provided at standard conditions (T=273.15K, p=1.0135 bar), T can also be denoted as T_0. Inserting these parameters into the $\frac{p}{z}$ method results in the following Equation 4.3:

$$V_{WG} = \frac{V \cdot V_m(\frac{p_{max} - p_{min}}{z_{p,max} - z_{p,min}})}{R \cdot T_0} \tag{4.3}$$

Here, V_{WG} is the working gas volume [Sm^3], V_m is the molar volume (0.022413 $\frac{\mathrm{mol}}{\mathrm{m^3}}$), V is the effective geometrical gas-occupied pore

volume [m^3], p_{max} and p_{min} are the minimum and maximum storage pressures [Pa], R is the universal gas constant [$\frac{J}{mol \cdot K}$] and T_0 is the temperature at standard conditions [K].

Using Equation 4.3, the working gas volume of the respective gas is determined ($V_{WG,i}$). One example to demonstrate this calculation is performed for a storage site in Lower Saxony, as it is presented in [66]. The molar volume ($V_m = 0.022413 \frac{m^3}{mol}$), the universal gas constant R ($8.314 \frac{J}{mol \cdot K}$), and the temperature T are known. The gas-occupied pore volume V is constant in the storage site, and this parameter is identical for individual working gas calculations for both storage cases. As the equation can be applied for both natural gas and hydrogen, the formula can be rewritten with V as the common parameter. Using the values for both gases and considering the constant geometrical pore volume of the storage site, Equation 4.3 can be rewritten in the following form (Equation (4.4)):

$$V_{WG,H_2} = \frac{V_{WG,NG} \cdot \left(\frac{p_{max} - p_{min}}{z_{p,max,H_2} - z_{p,min,H_2}} \right)}{\left(\frac{p_{max} - p_{min}}{z_{p,max,NG} - z_{p,min,NG}} \right)} \tag{4.4}$$

The equation parameters $z_{p,max,NG}$, $z_{p,min,NG}$, z_{p,max,H_2} and z_{p,min,H_2}, which are the compressibility factors for hydrogen and methane at the maximum and minimum pressures in the storage site, are obtained by applying the respective EoS and determining these values at the respective minimum (80 bar) and maximum pressures (160 bar).

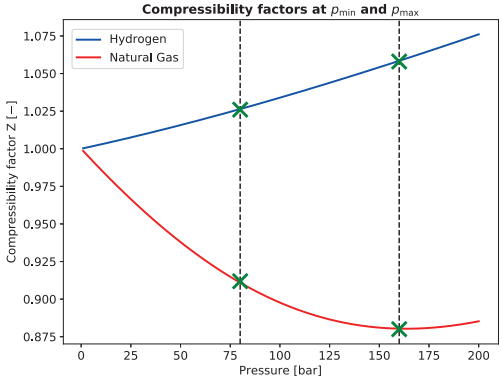

Figure 4.3: Curves of the compressibility factors for both methane and hydrogen at p_{min} = 80 bar and p_{max} = 160 bar (T=65°C (338.15 K))

Using the provided values, the total working gas volume for natural gas can be calculated with Equation 4.3. Equation 4.4 is used to estimate the hydrogen working volume. The natural gas working gas volume is about $3.9 \times 10^9\,\mathrm{Sm}^3$, compared to a H_2 working gas volume of $2.9 \times 10^9\,\mathrm{Sm}^3$, marking a reduction of nearly 25 %. Detailed calculations are shown in Lüddeke et al. (2022) [66]. Using the values for the z-factor ($z_{p,max}$, $z_{p,min}$) and the pressures, the working volumes for both cases were determined and compared.

4.2.2. Deliverability and withdrawal performance

During the preparation of a storage complex to store hydrogen, the flow behavior into and through the subsurface porous media also needs to be considered. The subsurface flow velocity and behavior of hydrogen will be different compared to natural gas through the pore channels and the tubing to the surface. For both gases,

the flow through the pipelines, tubings, and through the porous media is regarded as the main obstacle to the flow of gas, impeding and notably reducing the flux. The flow behavior is influenced by external factors, such as the geological and storage conditions. Gas properties also play a significant role in this case. In particular, the compressibility factor, the molar mass and the viscosity of the two gases have a noticeable impact on the flow behavior. The differences in these parameters characterize the gas flow rate in the early stages of the production or injection period. The production rate of gas from a storage site over time is also called the storage deliverability. As these gas characteristics are significantly different between natural gas and hydrogen, understanding and projecting their influence also needs to be known when designing a potential hydrogen storage site.

The deliverability describes the gas flow rate from a subsurface storage site per time. In this analysis, the flow of gas occurs uninterrupted, no pressure drops occur, and the flow of gas at the wellbore is identical to the flow at the wellhead. With this assumption, the resulting deliverability in terms of flow rate is equivalent to the subsurface radial inflow. It is written in the following universal way (Equation 4.5) [54]:

$$(p_{\mathrm{e}}^2 - p_{\mathrm{wf}}^2) = \frac{q\overline{\mu}Tp_{sc} \cdot \overline{Z}}{khT_{sc}}(ln\frac{r_e}{r_w} + s) \tag{4.5}$$

where p_e and p_{wf} are the storage and the bottom-hole flowing pres-

sures [Pa], q is the flow rate [$\frac{\mathrm{m}^3}{\mathrm{s}}$], μ is the viscosity [$\mathrm{Pa} \cdot \mathrm{s}$], T is the temperature [K], Z is the compressibility factor, k is the permeability [m^2], h is the perforation height [m], r_e and r_w and the external and wellbore radius [m] and s is the skin factor. During the injection and production phases between the surface and the subsurface, the turbulent flow regime acts differently than the laminar and uniform flow pattern. A non-Darcy flow regime is the governing flow type in the near wellbore area [90], requiring an additional friction factor in the deliverability equation. This frictional fraction accounts for these additional flow obstacles, and it is written in the following Equation 4.6:

$$(p_{\mathrm{e}}^2 - p_{\mathrm{wf}}^2) = \frac{q \cdot \overline{\mu} \cdot T \cdot p_{sc} \cdot \overline{Z}}{k \cdot h \cdot T_{sc}} \cdot (ln\frac{r_e}{r_w} + s)q + \frac{\overline{\mu}\overline{Z}Tp_{sc}D}{khT_{sc}}q^2 \quad (4.6)$$

where D is the individual non-Darcy additional friction factor. The input parameters vary and change during the production or injection phase, leading to different volumetric flow rates. Considering the volumetric flow rate changes requires the use of a molar conversion which leads to a deliverability function in the shape of molar flow. Assuming that the radial inflow in the subsurface is equivalent to the deliverability, the molar density ρ_{m} [$\frac{\mathrm{mol}}{\mathrm{m}^3}$] is used to generate molar flow rates [$\frac{\mathrm{mol}}{\mathrm{s}}$] for an incompressible flow as shown in 4.7.

$$q = \frac{2\pi\rho_m kh}{\mu(\ln(\frac{r_e}{r_w}) + s)} \cdot (p_e - p_{wf}) \quad (4.7)$$

The flow rate q is influenced by p_{wf}, p_e, k, μ, and temperature. The gas properties are dependent on the pressure difference between the storage and the bottom-hole flowing pressure. With time, these values change and influence the development of the deliverability flow rate q. The following Figure 4.4 is a modification which shows the exemplary deliverability graph of a producing well from an underground storage site.

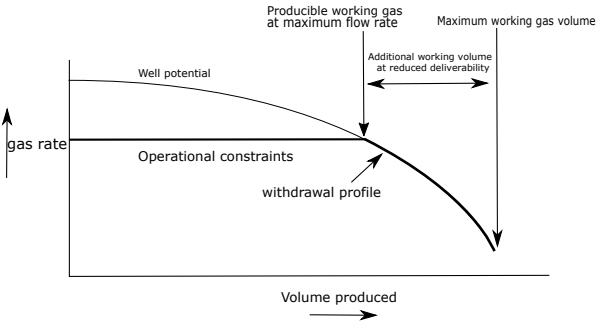

Figure 4.4: Storage deliverability profile of an exemplary subsurface gas storage site (adapted from Plaat, 2009 [84])

Figure 4.4 depicts the development of gas rates as a function of the produced gas amount with time. Initially, the storage site is entirely filled with gas and is at its maximum storage pressure. To begin the extraction of gas, the well is opened, and a bottom-hole flowing pressure (p_{wf}) is set. This set pressure is below the storage pressure, which enables the gas flow towards and into the well. At the beginning of the production, this pressure difference is at a

very high level, which results in an extremely high flow rate, equal to a maximum deliverability. This maximum deliverability is an ideal value, as it describes the extraction rate that can be attained assuming no restrictions in surface facilities or within the well apply. However, the surface facilities, such as gas separators or pipeline diameters, are obstacles that impede flow process. For these reasons, the theoretically maximum deliverability value at the beginning of the production process is not achieved, and the gas flows at a manually fixed maximum flow rate (q_{max}). When the well produces at q_{max}, the well is rate-controlled until the "producible working gas at maximum flow rate" is reached. This marks the last stage at which q_{max} is achieved. From this point, the governing flow conditions of the well change and the well is controlled by the differential pressure between the minimum bottom-hole flowing pressure ($p_{wf,min}$) and the storage pressure (p_e). The flow rate begins to decrease constantly. This decrease gains traction as the storage pressure decreases much faster compared to the initial stages. Less gas expands and occupies the pore volume, which leads to a quicker pressure decrease. The produced volume amount continues to increase, but at a reduced rate. The extraction process of gas continues until all working gas volume has been produced. According to Flanigan, to reach a balance between deliverability potential, processing and demand capacity, a mean of 50 % of the maximum deliverability is regarded as an optimal compromise. If the deliverability of a well is operated according to this philosophy, initially, a lower-than-ideal deliverability is attained. As this value is regulated, it can be maintained for a longer period of time. Most of the time, this value is kept until approximately 50 % of the working gas has been produced [29].

4.3 Static model description and storage pressure calculations

The differences in deliverability between natural gas and hydrogen is examined with the open-source numerical simulator DuMu^{X}. Two storage cases were defined, one natural gas (assuming $100\,\%$ methane) and one hydrogen storage case. A compositional fluid model with two phases and an adaptable number of components was defined. For each storage case, one single component was initialized; either methane or hydrogen, each at $100\,\%$. For each simulation case, a time-limited production period of six months was defined with an individual molar production rate of $900\,\mathrm{mol/s}$. This corresponds to a volumetric value of nearly $72\,635\,\mathrm{Sm^3/h}$. This value is averaged based on the maximum production rate from a storage site in Northern Germany provided in the Gas Infrastructure Europe (GIE) Database [33].

The grid model used for the simulation is a semi-artificial porous reservoir rock depicting a sandstone formation in Northern Germany. It consists of 44652 grid cells. Each grid cell has a length of 50 meters. The covered area is 3 x 3 km^2 and the average total height is about 101 meters. This model has closed, impermeable boundaries (no-flow Neumann boundaries) and no aquifer influence. The overall parameters of this storage site are shown in the following Table 4.2 [41].

Table 4.2: Storage site model geological parameters

Parameter	Symbol	Value	Unit
average vertical permeability	k_z	3	mD
average horizontal permeability	k_x	143	mD
average porosity	ϕ	15	%
average thickness	h	105	m
connate water saturation	S_{wc}	0.2	[-]
effective gas-occupied pore volume	V_g	$3.12 \cdot 10^7$	m^3
perforation interval	p_d	20	m
depth gas-water contact	GWC	1210	m
initial average pressure	p_i	120	bar
wellbore radius	r_w	0.1	m
reservoir temperature	T_{res}	65	°C

The initialization of the static model was performed for two cases. The first one considered a natural gas storage operation (assuming 100 % of methane) and the second case considered the storage site to be filled with 100 % of hydrogen. The following Table 4.3 shows the initial values of pressure, working gas and cushion gas volume for both storage cases.

Table 4.3: Initial states of the site for each storage case

Parameter	Symbol	Value	Unit
pressure at maximum stored natural gas	$p_{max,NG}$	120	bar
pressure at maximum stored hydrogen	p_{max,H_2}	120	bar
natural gas cushion gas pressure	$p_{CG,NG}$	55	bar
hydrogen cushion gas pressure	p_{CG,H_2}	51	bar
natural gas working gas volume	$V_{WG,NG}$	$2.43 \cdot 10^9$	Sm^3
natural gas cushion gas volume	$V_{CG,NG}$	$0.67 \cdot 10^9$	Sm^3
hydrogen working gas volume	V_{WG,H_2}	$2 \cdot 10^9$	Sm^3
hydrogen cushion gas volume	V_{CG,H_2}	$0.65 \cdot 10^9$	Sm^3

The storage layer of this model (excluding the impermeable caprock) is depicted in Figure 4.5.

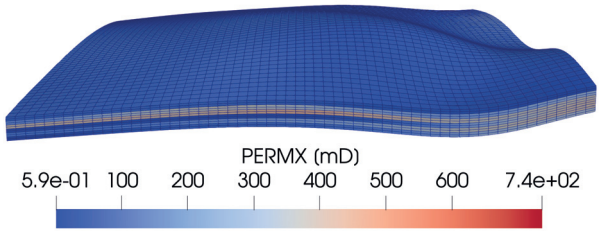

Figure 4.5: Overview of the porous storage layer (indicated permeability in x direction)

Five wells were distributed symmetrically across the grid model in order to cover a large area of the storage site. The locations of the production wells are shown in Figure 4.6.

The wells have equal distances in the horizontal and vertical directions. All of them have an identical wellbore radius (0.1 m) and perforation intervals (20 meters).

The volume of stored gas needs to be clearly defined. The total stored volume inside the porous media is considered the total gas (TG). This total stored volume contains the producible working gas and the unrecoverable cushion gas, which remains inside the storage site and maintains a minimum required storage pressure. The total stored gas was determined in DuMu^{X} for both cases and yielded the following values: $TG_{H2} = 2.6 \times 10^9\,\mathrm{Sm}^3$, $TG_{NG} = 3.1 \times 10^9\,\mathrm{Sm}^3$. The minimum required storage pressure is defined as a combination of influencing factors which are of subsurface and surface origin. The most important factors are the pressures.

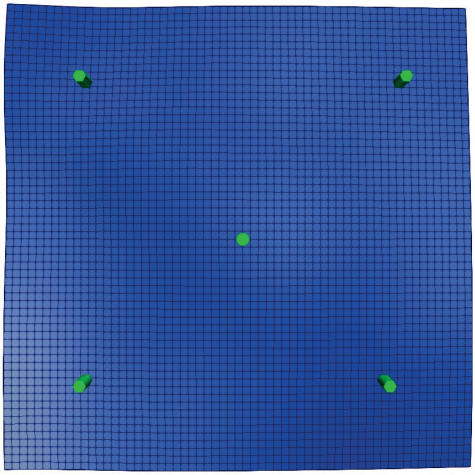

Figure 4.6: Locations of the storage wells (top view)

The surface pressure is the average pressure at which all surface facilities operate and inject the produced gas into the pipelines, forming the gas grid. In these simulations, the surface pressure is at a level at which the surface facilities operate without any additional compressors and remains unchanged during the simulation procedures. This value is set to 50 bar. When all working gas has been extracted and only cushion gas remains, the respective minimum storage pressure is equal to the minimum bottom-hole flowing pressure $p_{wf,min}$. $P_{wf,min}$ is estimated by calculating the pressure of the gas that fills the well using the hydrostatic column and the respective equation. For methane, the density stands at nearly $26\,\mathrm{kg/m^3}$, and hydrogen's density is nearly $4\,\mathrm{kg/m^3}$. Assuming constant surface pressure and the depth of the well

(1210 meters), the pressure difference for methane will be nearly 4 bar, and for hydrogen it will be 1 bar. Adding these two values individually to the surface pressure, the $p_{\mathrm{wf,min,NG}}$ will be 55 bar and nearly 51 bar for hydrogen. This approach was described by Katz and Lee (1990) to determine the bottom-hole pressure in preparation of gas withdrawal [54]. The use of 55 bar as a minimum bottom-hole flowing pressure for natural gas is also in alignment with two further studies that used this value to study the effect of gas processing on the selection of production technology and comparing the storage performance of natural gas to hydrogen [9, 52].

Using these values for $p_{wf,min}$, the z-factor values for both gases are calculated at these pressures as shown in Figure 4.3 and inserted into Equation 4.4. The results provide the initial working gas volumes for hydrogen and natural gas in the storage site. Subtracting the respective working gas volumes from the determined total gas values provides the cushion gas volumes for hydrogen and natural gas. In each case, it is assumed that the storage site is initially entirely filled with the respective gas, e.g. the subsurface natural gas storage case assumes that the stored gas is 100% methane. This pertains to the cushion and the working gas. In the hydrogen storage case, the cushion gas and working gas are 100% hydrogen. For each case, a single withdrawal procedure is simulated and no injection is considered.

4.4 Results and discussion

The results of the working gas volume calculations and the deliverability development for both cases showed noticeable differences between hydrogen and natural gas. The determined quantities of available working gas have different levels, leading to different energy contents that can be stored in the identical pore space. The analysis of the deliverability profiles indicate different durations of the maximum plateau rate and varying flow rate values at which the individual well flow rates change.

4.4.1. Storage capacities between an existing UGS compared to a prospective UHS

The differences in the z-factors of natural gas and hydrogen at identical pressures provide a first hint that the initially stored volumes of both gases in the subsurface storage site will differ significantly from each other. The initial working gas volumes, the total stored volumes and the energy contents for both gases are shown in the following graphs in Figure 4.7.

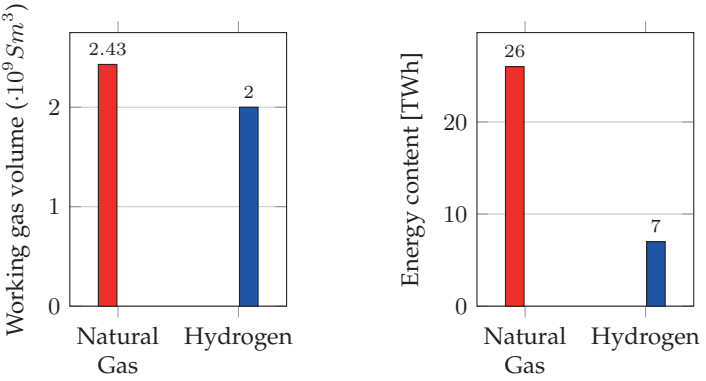

Figure 4.7: Comparison of stored working gas volumes and respective energy content (adapted after Lüddeke et al. (2026) [68])

The comparison of the working gas volumes (natural gas = $2.43 \times 10^9\,\mathrm{m}^3$, hydrogen = $2 \times 10^9\,\mathrm{m}^3$) reveals a larger natural gas volume that can be stored. The hydrogen working gas volume is approximately $18\,\%$ lower than natural gas, similar to the total stored hydrogen. Taking into account the calorific values for both gases, a greater decrease in stored energy is revealed. The working gas energy content of H_2 stands at $7\,\mathrm{TWh}$ compared to $26\,\mathrm{TWh}$ for natural gas, marking a decrease in the aforementioned storage site by nearly $75\,\%$. These findings align with values previously determined and published in literature [66]. These significant decreases in volume and energy indicate that nearly three-quarters less energy can be stored in a potential hydrogen storage complex compared to an existing natural gas facility. A future hydrogen storage site will be capable of storing a lesser energy content and therefore a smaller energy is available for withdrawal.

4.4.2. Natural gas and hydrogen deliverability

As the working gas volumes differ for each storage case, these differences also affect the respective deliverability. In terms of some gas properties, such as z-factor, molar mass and viscosity, these characteristics are different for both gases. In addition to that, every change in pressure will impact the aforementioned characteristics. A closer analysis of the parametric influence on the deliverability was accomplished through two individual simulation cases, one for hydrogen and one for natural gas. These were developed to examine the development of the withdrawal rates from the storage site. The extraction period is fixed at 180 days. The upper flow rate limit of $72\,635\,\mathrm{Sm^3/h}$ per well is applied and the respective $p_{wf,min}$ for natural gas and hydrogen applies. For five wells, the development of the flow rates with time and with cumulative produced working gas volume are shown in Figure 4.8.

Natural gas maintains a plateau rate for approximately 58 days while the hydrogen plateau lasts for nearly 70 days (Figure 4.8a). After reaching the end of the respective plateau rates, the production curves begin to decline. The beginning of the decline marks the first noticeable change in a well's production rate when it no longer exceeds the individual maximum level of $72\,618\,\mathrm{Sm^3/h}$. The decline slope for hydrogen is much greater than for natural gas. The second change in the production rates occurs after 90 days in both cases and at a rate of nearly $340\,000\,\mathrm{Sm^3/h}$. Afterwards, the hydrogen production decreases much faster and its respective slopes increase more. When natural gas is produced, the subsequent changes in the

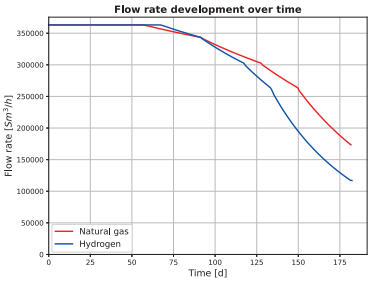

(a) Development of flow rates versus time

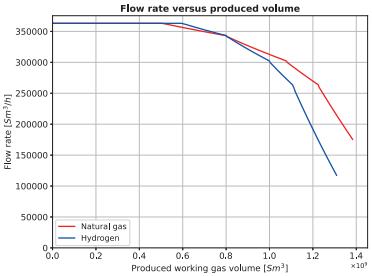

(b) Development of flow rates with cumulative produced working gas volumes

Figure 4.8: Storage deliverability of natural gas and hydrogen and produced cumulative working gas volume over time [68]

individual well rates occur after 128 and 150 days, and it reaches a final cumulative production rate of nearly $175\,000\,\mathrm{Sm}^3/\mathrm{h}$ at the end of the production period. The changes in the hydrogen production curve occur after 118, 130, and 179 days and reach an end production rate of approximately $120\,000\,\mathrm{Sm}^3/\mathrm{h}$. Towards the end of the production period, the hydrogen production curve does not have a linear decline, but it begins to flatten out, leading to a reduced decline. The difference between the hydrogen and natural gas flow rate curve increases and reaches a maximum at the end of the production phase.

The withdrawn volumes of the respective working gas also exhibit different behaviors during the production. During the respective plateau withdrawal time, a constant volume of working gas is produced at the same maximum rate. When the natural gas flow rate begins to decline, nearly $5 \times 10^8\,\mathrm{Sm}^3$ of working gas has been produced, while this value is at $6 \times 10^8\,\mathrm{Sm}^3$ for hydrogen. As the

production rates decline further, the cumulative produced volumes increase at a slower rate which is dependent on the production rate at the specific time. The produced volume slopes for natural gas are less steep compared to hydrogen. This is the same performance that was noticed in the development of the flow rates. The changes in the decline slopes occur simultaneously when the governing flow conditions in the wells change. At the end of the production process, nearly $1.3 \times 10^9\,\mathrm{Sm}^3$ of hydrogen working gas compared to $1.39 \times 10^9\,\mathrm{Sm}^3$ of natural gas have been produced. This indicates a larger withdrawn volume of natural gas but also a greater amount of it still remains inside the porous media. The following Figure 4.9 shows the flow rate as a function of the produced working gas volume.

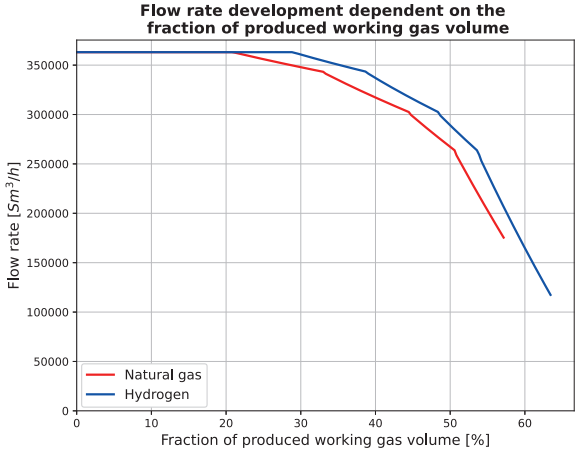

Figure 4.9: Fraction of produced working gas volumes for hydrogen and natural gas [68]

The increase in the produced volumes and the corresponding ratios of the respective gases has similar shapes as the production is underway. At the end of the respective plateau withdrawals, about 28 % of recoverable hydrogen working gas was produced, compared to about 22 % of natural gas. As the production rates decline, the increase in the respective working gas volumes also reduces, just like the increase in the fractions. The slopes in Figure 4.9 are almost parallel to each other, and the relative difference between the two curves remains constant. The ratio-values indicate a steadily declining increase in the recovered working gas amounts. Overall, the withdrawn ratio for natural gas remains below the level for hydrogen. Each change in the withdrawal rate occurs at identical rates, but at lower ratios for natural gas. At the end of the production period, nearly 57 % of natural gas and nearly two-thirds of hydrogen were recovered. In both cases, more than half of the available working gas volumes were recovered.

During the production from an underground storage site, the withdrawal of the stored volumes leads to a depletion and a decrease in pressure. Considering the differences in gas characteristics between hydrogen and natural gas, the gas properties do not just influence the development of the rates but also the decrease in the respective storage pressures. The storage pressure during the production period is shown in Figure 4.10.

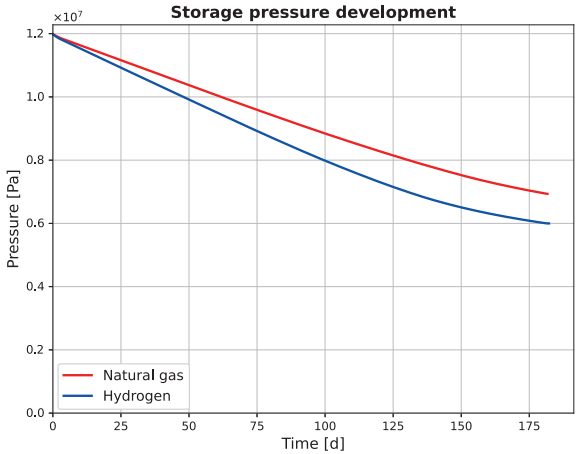

Figure 4.10: Pressure development during the seasonal production process for both storage cases

When the production begins, both storage cases are at the initial and maximum storage pressure of 120 bar. Over time, the pressure in the natural gas storage will decline at a lesser degree compared to hydrogen. Natural gas pressure maintains a steady linear decline and begins to minimally flatten out after nearly 130 days, and reaches a final storage pressure value of 70 bar. The hydrogen storage pressure declines at a higher degree, and its curve has a greater curvature towards the end of the production process, and it reaches a final storage pressure of 60 bar.

Sensitivity analyses of varying maximum storage pressures

So far, the analysis of the flow rates has been performed under the assumption that the initial storage pressures for both cases were at

120 bar. The initial storage pressures are dependent on the deliverability demand and the needed storage quantities, resulting in potential varying maximum storage pressure values. As the subsurface radial inflow of the stored gas is dependent on the pressure difference, a different maximum storage pressure will influence the differential pressure, thereby impacting the development of the flow rates. To examine the influence of various maximum storage pressures, the cases in which the storage pressure is 120 bar are named "base case" and a sensitivity analysis of two different storage pressure levels (100 bar, 150 bar) are performed. The results of the sensitivity analysis are compared to the base cases, which is depicted in Figure 4.11.

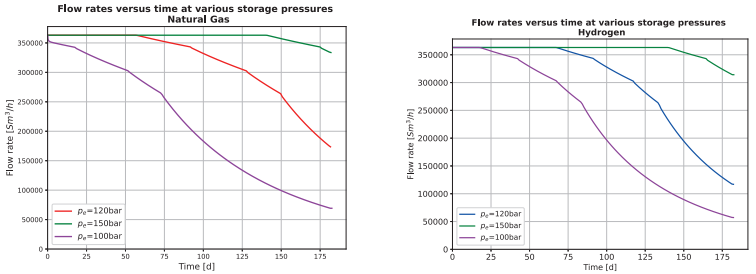

(a) Influence of varying storage pressures on the natural gas flow rates

(b) Influence of varying storage pressures on the hydrogen flow rates

Figure 4.11: Sensitivity analyses of different storage pressures on the withdrawal rates [68]

Figure 4.11 reveals that higher storage pressures result in a longer plateau withdrawal duration and lower storage pressures reduce the plateau length. At a storage pressure of 150 bar, the plateau withdrawal rates reach 135 days for natural gas and hydrogen. Lower

storage pressures reduce the hydrogen plateau duration to 20 days, while natural gas maintains a plateau level for only a couple of hours. The natural gas flow rate remains in decline throughout nearly the entire production period. At higher storage pressure, the changes in the flow rates occur at the same production values, only at different points in time. Analogous to the plateau duration, the changes in the flow rates occur earlier at lower pressures, while higher storage pressure levels delay those changes. The rate of decline also differs slightly depending on the storage pressure. When the storage pressure is higher, the decline slope is slightly flatter compared to the decline slopes at lower storage pressures for natural gas and hydrogen. The flow rates at lower storage pressure for both cases indicate that a reduction in the decline begins after about 74 and 80 days respectively. The decline is not anymore linear, but the curve begins to form a round shape. The decline reduces and begins to flatten out towards the end of the production period. Lower final production values are noticed at lower storage pressures compared to higher pressure levels. Table 4.4 provides an overview of the final flow rates for both storage scenarios and the respective storage pressures.

Table 4.4: Final flow rates in $\mathrm{Sm^3/h}$ in a natural gas and a hydrogen scenario at various storage pressures

Storage case	$p_e = 100\,\mathrm{bar}$	p_e = base case	$p_e = 150\,\mathrm{bar}$
Hydrogen	60000	120000	320000
Natural gas	75000	175000	330000

The various maximum storage pressures revealed differences in the final extraction rates at the end of the production period. The development of the flow rates and their magnitudes also affect the cumulative withdrawal volume in each case as shown in Table 4.5.

Table 4.5: Cumulative withdrawn volumes in 10^9 Sm^3 in a natural gas and a hydrogen scenario at various storage pressures

Storage case	p_e = 100 bar	p_e = base case	p_e = 150 bar
Hydrogen	0.97	1.31	1.56
Natural gas	0.92	1.39	1.57

Sensitivity analyses of different bottom-hole flowing pressures

Analogous to the storage pressure, the bottom-hole flowing pressure is dependent on the demand and operational conditions. The performed withdrawal simulations have assumed a constant $p_{wf,min}$ during the entire production period for every storage case. As the bottom-hole flowing pressure values can have various levels depending on the production conditions, this pressure will impact the pressure difference and thus also the radial inflow of gas and the production rates. To examine the impact of various p_{wf}, the original values used for the simulations ($p_{wf,NG}$ = 55 bar, p_{wf,H_2}=51 bar) are referred to as "base case". Another sensitivity analysis is performed with a p_{wf} of 60 bar and with 40 bar for each storage scenario. The sensitivity analysis of varying $p_{wf,min}$ is shown in Figure 4.12.

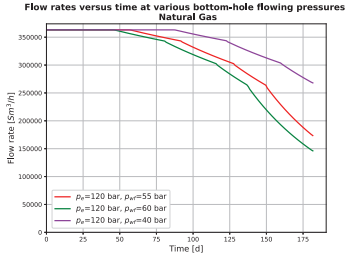

(a) Influence of varying bottom-hole flowing pressures on the natural gas flow rates

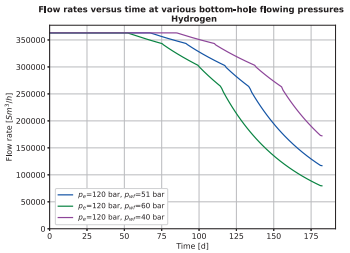

(b) Influence of varying bottom-hole flowing pressures on the hydrogen flow rates

Figure 4.12: Sensitivity analyses of different bottom-hole pressures on the withdrawal rates [68]

The selection of a bottom-hole flowing pressure distinctly influences the development of the flow rates for natural gas and hydrogen. A higher p_{min} leads to a reduced pressure difference between p_e and p_{wf}, resulting in lower flow rates and a shorter plateau duration. A p_{min} of $60\,\mathrm{bar}$ reduces the natural gas plateau duration from 60 to 48 days and the hydrogen plateau length from 70 to 53 days. A lower p_{min} extends the natural gas and hydrogen plateau duration to nearly 85 days. Not only does a lower p_{min} result in a longer plateau duration, the decline in the flow rates also occurs much later at identical flow rates for both cases, respectively. Table 4.6 provides an overview of the ultimate flow rates at the end of the production period.

Table 4.6: Final flow rates in $\mathrm{Sm^3/h}$ at various bottom-hole flowing pressures

Storage case	p_{wf} = 40 bar	p_{wf} = base case	p_{wf} = 60 bar
Hydrogen	175000	120000	80000
Natural gas	270000	175000	145000

Analogous to the sensitivity analyses of the maximum storage pressure on the cumulative withdrawn volumes, different bottom-hole flowing pressures will also influence the volumes of the extracted gas. The cumulative volumes produced at different p_{wf} are shown in Table 4.7.

Table 4.7: Cumulative withdrawn volumes in 10^9 $\mathrm{Sm^3}$ at various bottom-hole flowing pressures

Storage case	p_{wf} = 40 bar	p_{wf} = base case	p_{wf} = 60 bar
Hydrogen	1.43	1.31	1.19
Natural gas	1.50	1.39	1.33

The final flow rates are at overall higher levels when the p_{min} is at lower values. The plateau duration is prolonged and the decline in the flow rates occurs at a later time. At higher p_{wf}, the changes in flow rates occur earlier. In general, the selection of the p_{wf} has an effect on the time-dependent changes in the flow rates. The shapes of the flow curves are not affected by the pressure difference,

indicating that the gas properties impact the shape of the respective flow curves.

Influence of skin on the flow rates

So far, the withdrawal development has been analyzed considering an unobstructed inflow of gas into the well and production, assuming ideal operating conditions. However, subsurface flow restrictions have to be taken into account, especially in the near-wellbore area. A positive skin factor of 2 was defined and the skin-influenced withdrawal processes were compared to the unobstructed base cases for both gases as shown in Figure 4.13.

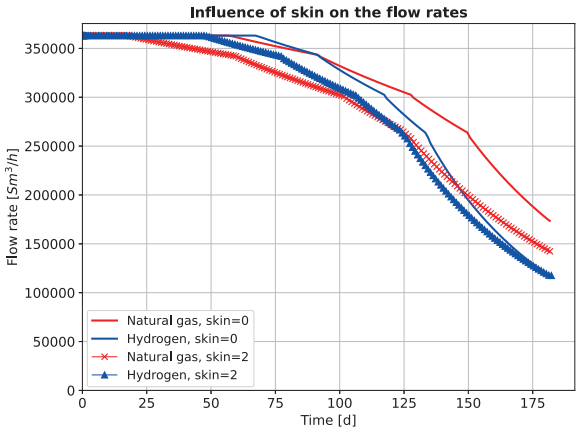

Figure 4.13: Influence of skin (2) on the flow rates [68]

The analysis of the skin-factor indicates a noticeable influence on the development of the flow rates for hydrogen and natural gas. A

positive skin factor reduces the plateau duration of natural gas from previously 60 to nearly 23 days and from 67 to about 50 days for hydrogen. The decline in the skin-impeded curve for natural gas is nearly parallel to the unobstructed flow. After nearly 125 days, the decline is not anymore linear and it slowly begins to flatten out, reaching a final flow rate of nearly $140\,000\,\mathrm{Sm^3/h}$, compared to $175\,000\,\mathrm{Sm^3/h}$ in ideal withdrawal conditions. In the case of hydrogen, initially the decline of the restricted flow is also nearly parallel to the unobstructed flow. After 175 days, the skin-restricted flow curve also begins to flatten out and the decrease is reduced. The ultimate flow rate value overlaps with the ideal flow rate value at $125\,000\,\mathrm{Sm^3/h}$. The skin factor is regarded as an additional zone in the near wellbore area, which increases the pressure drop between the external boundary and the wellbore radius, restricting the inflow of gas into this area. The skin factor reduces the plateau rate for both gases and induces an earlier decline in pressure, leading to earlier changes in the flow rate and a slower depletion of the storage site.

Influence of gas characteristics on the flow rate development

The behavior of natural gas and hydrogen during production shows some very distinguishable differences. At the given conditions for a hypothetical hydrogen and natural gas storage site, the stored hydrogen volume will decrease by more than $18\,\%$ compared to natural gas, more than half of the available H_2 working gas will be produced, the storage pressure will decrease at a relatively higher rate and reach a lower level at the end of the production process. The final production value for hydrogen will also be below the

value of natural gas and the deliverability duration for hydrogen is slightly longer than for natural gas. The differences in this behavior are attributed to the varying gas characteristics that influence the gas behavior. Some of the key characteristics are the compressibility factor, molar mass and viscosity. Natural gas and hydrogen have different compressibility factors ($z_{NG} \leq 1$, $z_{H_2} \geq 1$), resulting in different stored volumes at identical elevated pressures and in different plateau durations. The differences of the mentioned characteristics combined impact the production curves and the storage pressure decline. To examine the influence of the parameters, a pseudo gas in the compositional fluid system was defined. In the subsequent simulation runs, one property of the pseudo gas was changed and its influence on the deliverability and production was analyzed. In the first run, the z-factor behavior of hydrogen was implemented, while viscosity and molar mass of natural gas remained unchanged. In the second run, the molar mass was changed and in the last run the viscosity was altered. The same production parameters apply to both cases (180 days, $p_{wf,min}$= 55 bar, q_{max}=72 618 Sm^3/h). The withdrawal curves of the pseudo gas were compared to the production curves of hydrogen and natural gas, as they are shown in the following Figure 4.14.

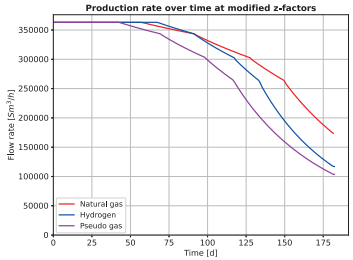

(a) Pseudo gas production curve with the compressibility factor behavior of hydrogen

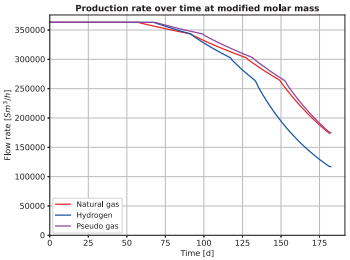

(b) Pseudo gas production curve with the molar mass of hydrogen

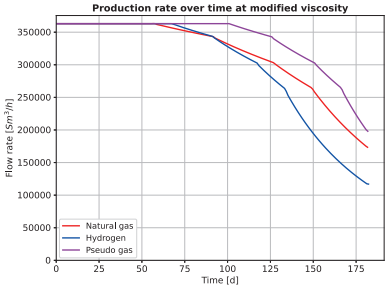

(c) Pseudo gas production curve with the viscosity of hydrogen

Figure 4.14: Production curves of the pseudo gas at altered gas characteristics [68]

Figures 4.14 a to c reveal that the analyzed characteristics have distinct influences on the shape of the pseudo gas's production curve. They affect the length of the plateau level, the inclination of the slopes, the cumulative rates and points in time when the individual well rates fall below the maximum flow rate and change from a rate-controlled to a pressure-controlled method. The characteristics and their impact are discussed in the following paragraphs.

Z-factor

When the pseudo gas has the z-factor behavior of hydrogen, the plateau duration is significantly shortened to 43 days. Once the maximum withdrawal rate is no longer exceeded, the production curve begins to decline, and it behaves similarly to the decline of the hydrogen curve. The two curves are nearly parallel from the beginning of the decline until the 100^{th} production day. Afterwards, the gap between the hydrogen and the pseudo gas curves decreases. 120 days after production began, the pseudo gas curve begins to flatten out, and it flattens out more noticeably than the hydrogen flow curve. The higher z-factors also induce an earlier change in the respective individual well flow rates. The final production value of the pseudo gas reaches $105\,000\,\mathrm{Sm}^3/\mathrm{h}$, which is the lowest value compared to hydrogen and natural gas (125000 and $175\,000\,\mathrm{Sm}^3/\mathrm{h}$, respectively).

The z-factor of hydrogen is constantly above 1 and has a slight linear increase as pressure increases. When the pressure decreases, hydrogen's z-factor decreases, resulting in a decompression of the gas. The z-factor greater than one indicates that the gas is not able to sustain the pressure as effectively as natural gas, leading to a significantly quicker decline in storage pressure. At higher pressures, the difference in the z-factors between p_e and p_{min} is greater. However, at higher pressures, a smaller volume can be effectively compressed in the available pore space and the effect of the z-factor is larger. At lower storage pressures, the difference between the z-factors is less; the $z_{p,max}$ is closer to the $z_{p,min}$. The z-factors have a stronger impact on the subsurface volume and flow behavior at larger pressure differences.

The lower hydrogen compressibility is one major factor contributing to a larger decline in the production values and storage pressure. The higher z-factor of hydrogen shapes the production curve of the pseudo gas significantly and makes it resemble the shape of the hydrogen flow curve. Another similarity is the noticeably large change in the flow rates with time. The higher compressibility factor considerably induces a shorter plateau withdrawal period, shifting the production flow curve towards the left. The decline in the individual well flow rates increases with every further change and occurs at an earlier point in time.

The effect of the z-factor appears to decrease as the storage pressure declines. The z-factor approaches the value of 1 when the pressures decrease, indicating an ideal gas behavior. As the z-factor decreases, its effect on the gas production performance decreases. Simultaneously, the decline in storage pressure reduces. The lower compressibility of hydrogen also cannot sustain the storage pressure as effectively as natural gas is capable of doing. As a lower H_2 volume is compressed, the decompression will be quicker, affecting the storage pressure quicker. The lower compressibility factor of natural gas reveals the gas's higher compressibility, which leads to the gas occupying a larger storage volume more effectively at higher pressures. For hydrogen, a larger volume of gas does not occupy a larger pore space and the intermolecular forces (London dispersion forces) become stronger. In turn, a reduction in pressure will lead to a shorter pressure sustainment and a quicker depletion in a hydrogen storage case. These effects underscore the importance of the z-factor on the production behavior of a gas from the subsurface.

Molar Mass

To modify the density of the pseudo gas, the molar mass is changed. In this case, the molar mass of hydrogen (m=$2\,\mathrm{g/mol}$) is used. At a lower molar mass, the plateau withdrawal time lasts for about 70 days, matching the length of the hydrogen plateau duration. When the production rates decline, the slope of the production curve is very similar to the natural gas curve. The pseudo gas curve is nearly parallel to the natural gas flow curve up to 135 days after production began but its overall flow values are greater. After 135 days, the pseudo gas flow curve begins to approach the natural gas flow curve, the two curves nearly overlap and approach an identical final production value of approximately $175\,000\,\mathrm{Sm^3/h}$.

Figure 4.2b depicts that the densities of hydrogen and natural gas are dependent on the pressure, with the pressure exerting a greater influence on the natural gas density than on hydrogen. A decrease in pressure from 200 bar to atmospheric pressure will result in larger density changes of natural gas. Natural gas has a higher pressure gradient as the depth varies, while the hydrogen gradient changes at a smaller degree. Therefore, pressure changes will have smaller effects on its density. At the gas-water-contact, the pressures of natural gas and hydrogen are at the same level. Assuming a reference depth of 1200 meters inside the gas zone of the presented storage model, the natural gas pressure would be lower than for hydrogen, due to the respective pressure gradients. The slightly higher hydrogen pressure leads to theoretical flow rate values that are greater than the theoretically determined values for natural gas. The greater hydrogen flow rate values lead to a longer-lasting plateau rate for hydrogen and an increased slope in the flow rate decline. During

the decline of the production curve, the hydrogen density is minimally affected. This results in a stable decline between each change in the well's governing parameters. The molar mass reveals that its effect is contrary to the effect of the compressibility factor by prompting a longer plateau withdrawal time.

Viscosity

Figure 4.2a unveils the influence of the storage pressure on the respective viscosity. At a storage pressure of 200 bar, μ_{NG} will be nearly 1.8 times greater than μ_{H_2}. With a lower viscosity, the pseudo gas plateau withdrawal lasts about 100 days before the flow rate values begin to decrease, similarly to the hydrogen storage case. The changes in each well's individual flow rate occur much later, and the slope of the pseudo gas curve remains linear until it reaches a final production rate value of $195\,000\,\mathrm{Sm^3/h}$, which is the highest value. The last slope in the pseudo gas curve is the steepest one, indicating the strongest decline in the cumulative flow rates.

The viscosity fundamentally impacts the mobility of a gas, which determines the flow behavior of a gas at various pressures. The low hydrogen viscosity results in high gas mobility, which facilitates the easier flow of hydrogen through the reservoir rock. The quasi-steady hydrogen viscosity results in even slope shapes of the hydrogen and of the pseudo gas curves. The higher gas mobility also counters the effect of the compressibility factor by leading to a longer plateau withdrawal time and shifting the production curve of the pseudo gas towards the left.

Parametric effects on the flow rate development

The flow rate development is dependent on a variety of factors, namely the acting storage and bottom-hole flowing pressure and the z-factor, molar mass and viscosity of the respective gas. The z-factor has the largest influence on the shape of the production curves with a lower z-factor reducing the decline in the flow rates and resulting in later changes in the individual maximum flow rates. A higher z-factor also results in a quicker depletion of the storage site and reduction in storage pressure. The longer plateau duration of hydrogen can be attributed to the lower viscosity value, leading to a higher mobility and facilitating the flow of gas through the porous media. The higher mobility also induces a steeper decline in flow rates, accelerating the depletion of the storage site. A lower molar mass also induces a longer plateau duration and a later beginning in the decline of flow rates. While the z-factor appears to exert the strongest influence on the shapes and the development of the flow curves, the viscosity and molar mass appear to influence the time development of the rates. The minimum and maximum pressures contribute to the withdrawal progress and influence the rate development with higher storage and lower bottom-hole flowing pressures leading to longer plateau durations and a later decline in the flow rates. As an additional pressure drop layer in the near wellbore area, the skin factor limits the gas inflow into the wellbore and the production.

4.5 Conclusions

In this chapter, an overview of the general geological, technical, and physical challenges facing the conversion of an existing subsurface natural gas to a hydrogen storage site were analyzed and discussed. Available and potential volume storage calculations, and numerical production simulations were performed to determine recoverable working gas volumes and the corresponding energy content. The key findings of this chapter are:

- Hydrogen and natural gas (assuming $100\,\%$ methane) have different gas properties, which play a significant role in the gas behavior at storage conditions and during the production from the subsurface. Hydrogen has a smaller molecular weight, size and a smaller volumetric energy content than natural gas. It also has a compressibility factor that is greater than 1 and a much lower density and viscosity. Those properties determine each individual gas's characteristic at standard and at elevated pressures.
- The higher compressibility factor, the lower viscosity and density of hydrogen significantly reduce the potentially stored gas volume inside a porous formation. At elevated pressures, the reduction in the stored volume could reach up to $25\,\%$. When the energy content is calculated, a significant decrease is the result. Not only can a smaller volume of hydrogen be stored, but the total stored energy content is also heavily diminished.
- By defining a pseudo gas with changing characteristics, the in-

fluence of the compressibility factor, density and viscosity on the production rates has been analyzed. The compressibility factor has the strongest influence on the plateau duration and the shape of the pseudo gas. The density and viscosity parameters predominantly influence the length of the deliverability level and mostly counter the effect of the compressibility factor by leading to a longer duration and a later beginning in the production decline. The analysis of the most important gas characteristics is key to understanding the flow and the production behavior from the subsurface.

- The volumetric quantities of each storage case were defined by the stored gas type and the storage conditions. Natural gas had a larger stored volume than hydrogen. This affected the volumes of working and cushion gas for each gas, with larger working and cushion gas volumes for natural gas. After determining the total stored volume in DuMu^{X} and the respective working gas volume using the respective minimum and maximum pressures and the corresponding compressibility factors, the cushion gas was calculated from the difference between the total and the working gas for each gas type.
- The storage and production pressure conditions influenced the extraction process and the withdrawal volumes for each storage case. As the pressure difference between the storage and the bottom-hole flowing pressure is a key element in the calculation of the inflow rate, this value influenced the produced amount at the end of the withdrawal period. When the bottom-hole flowing pressure increased, the cumulative withdrawn volumes were lower. With regard to varying storage

pressure, higher storage pressures lead to larger cumulative produced volumes at the end of the production period.

Chapter 5

Simulation of the conversion of an existing UGS to a prospective UHS

Preparing an existing subsurface porous storage site for a conversion process requires a detailed plan of an implementation procedure. The hydrogen availability, the demand for it are essential driving factors in a storage conversion process. The analysis of the geological properties regarding their hydrogen suitability is a time-consuming procedure, and the projected hydrogen demand influences the duration of the conversion process. As existing subsurface storage sites are actively operating as storage facilities, implementing the conversion procedure has to be done during each site's storage cycle for a couple of years. Risk factors, for instance microbial consumption of hydrogen, mixing processes between gases and impurities in the produced gas, could impact this process.

The semi-artificial subsurface storage site presented in Chapter 4 and its properties are used to simulate a conversion process from a natural gas storage site to a hydrogen storage site within 10 years and a following one-year hydrogen storage cycle. The operation schedule is based on a forecast of hydrogen demand within the following 20 years and the hourly injection/production rates necessary to meet the expected demand. Two storage conversion scenarios are simulated: (I) a sterile conversion from natural gas to hydrogen assuming no hydrogenotrophic biochemical reactions, and (II) a

conversion process considering microbial consumption processes at growth parameters determined from the micromodel experiments in Chapter 3.

5.1 Simulation approach

DuMu^{X} was applied to model and simulate the field-scale storage scenario. The initialization of the gas composition in the storage site was assumed to be $98.5\,\%$ CH_4 and $1.5\,\%$ CO_2. An isothermal case is assumed ($T_i = 65$ °C). Like in Chapter 4, the gas behavior at real conditions ($p_i = 120$ bar) was modeled with the Peng-Robinson Equation of State. The same five wells were used for this conversion process with every well being either an injecting or a producing well, depending on the scheduled rate. The total rate is divided equally for all five wells, so that one well injects one-fifth of the scheduled injection flux. Each well penetrated the storage formation in many grid cells, with each grid cell having different geological properties. Permeability and porosity varied for each grid cell, and this heterogeneity lead to a division of the injection flux for each grid cell. For the penetrated grid cells, the total mobility λ_{total} was calculated by summing up the individual cell-specific mobilities for gas and liquid (λ_j^κ) by calculating (c.f. Equation 5.1):

$$\lambda_{total} = \sum_{i,j} \frac{\sqrt{k_{xx,i} \cdot k_{yy,i}} \cdot h_i}{\mu_j} \tag{5.1}$$

where k_{xx} and k_{yy} are the local permeabilities in x and y direction, h_i is the height of the grid cell and μ_j^κ is the phase-specific mobility. The injection flux for each grid cell was calculated as:

$$q_{inj}^{\kappa} = q_{inj} \cdot \frac{\lambda_j^{\kappa}}{\lambda_{total}} \tag{5.2}$$

with q_{inj} being the total well inflow rate [$\frac{\mathrm{mol}}{\mathrm{s}}$].

In the production phase, the necessary rates were provided. This value was also distributed evenly among all five wells, so that each well contributed an equal share to the total production rate. The production of the components was influenced by the respective concentrations in the storage site, making it impossible to deliberately control the composition of the outflowing flux. The composition of the total production flux is also controlled by the mobilities and the respective composition, as shown in Equation 5.3

$$q_{prod}^{\kappa} = q_{prod} \cdot \sum_i \frac{\lambda_j \cdot c_j^{\kappa}}{\lambda_{total}} \tag{5.3}$$

with c_j^{κ} as the liquid or gaseous concentration of a component κ.

For each well, the same maximum molar flow rate of $900\,\mathrm{mol/s}$ was applied which defined the upper injection and production limit value. However, these values were never exceeded, and all wells remained rate-controlled during the entire conversion process.

The initialization of the storage parameters was performed assuming hydrostatic and thermodynamic equilibrium. Nearly the entire storage site is assumed to be inside the gaseous zone ($S_g = 0.8, S_w = 0.2$), with a small area at the boundary inside the water zone ($S_g = 0.05, S_w = 0.95$). Separating these two zones is a transition zone, in which the gas and liquid saturations are determined by the capillary pressure between the two phases.

Based on the thermodynamic equilibrium, the concentrations of the components in the gas and water zone are identical and this is modeled with the fugacity coefficient, along with the other initial parameters:

$$p_w = p_{ref} - \rho_g \cdot (d_{ref} - d) \tag{5.4}$$

$$c_w^\kappa = c_g^\kappa \cdot (1 - \varphi_{H_2O} \frac{p_w}{p_g}) \frac{p_g}{\varphi_g^\kappa p_w} \tag{5.5}$$

with $\mathrm{p_{ref}}$ as the reference pressure $120\,\mathrm{bar}$, $\mathrm{d_{ref}}$ the reference depth $1200\,\mathrm{m}$, d is the depth of every element, $\mathrm{p_g}$ and $\mathrm{p_w}$ are the liquid and the gas pressures [bar] and $\varphi_\mathrm{g}^\kappa$ is the liquid fugacity coefficient of each component. The gas compositional initialization was fixed at 98% CH_4, 1.5% CO_2 and the rest was nitrogen. The small carbon dioxide fraction was initialized to replicate a fraction of the natural gas composition in a storage site and to provide the energy source for the microbial conversion in a biochemical case.

5.1.1. Development of subsurface storage conversion schedule

The framework for the development of a hydrogen storage site is strongly influenced by the forecasted hydrogen demand in the vicinity of the storage site, the immediate hydrogen availability and the quantities that could be delivered. A hydrogen demand projection was established through energy system analysis in the interdisciplinary project H_2 Guide Lower Saxony between 2021 and 2024 [62]. In this work, a constant development of renewable energies and carbon neutrality was assumed in Germany by 2045. The chain of the

energy system analyzed the import, production and consumption of hydrogen for private and corporate purposes, including the usage of storage capacities to balance the daily demand and availability. In Lower Saxony, these parameters were analyzed for every county separately to obtain a precise distribution of the local total daily demands.
Based on the energy storage analysis, a regional annual storage quantity of $802.7\,\mathrm{GWh}$ was determined for the storage site analyzed in the following paragraphs. The apparent injectivity/deliverability was provided for every hour. Porous storage sites are originally intended to serve a constant daily demand or uptake, and changing between injection and production methods requires a prolonged period of stabilization. Therefore, switching within a short period of time between production and injection is a technical and numerical challenge. To establish an annual schedule consisting of daily constant rates, the method of the moving average was implemented in Python. The overall formula of the moving average is shown in Equation 5.6:

$$MA = \frac{1}{k} \sum_{i=n-k+1}^{n} p_i \tag{5.6}$$

with i being the index position in the dataset, n is the index of the current data point, and k is the window size, which is currently being averaged.

The hourly injection and production energies were accumulated and a total daily energy was determined for each day of the year. The daily values switched often between injection and production. After

determining the moving average, the averages were rearranged in such a way that the production values were in subsequent order, followed by the injection values. Considering that the first months fall into the withdrawal season, the production values are split between the first four and the last four months of the year. The injection period falls right in between the production time. The schedule for one year is depicted in Figure 5.1.

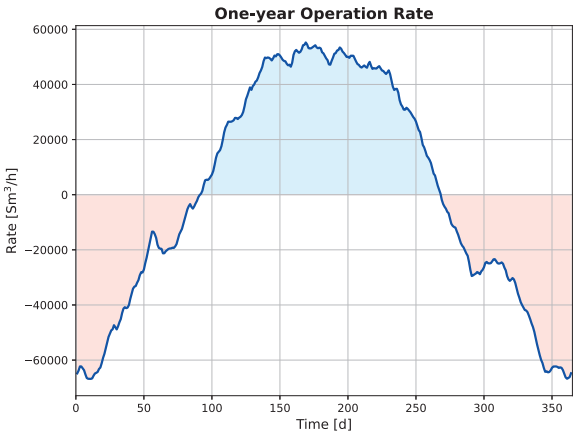

Figure 5.1: Operational rates spanning one year (injection = 100% hydrogen, production = stored gas)

As mentioned, the first four months of the year begin with the production season, which is followed by an injection period of nearly four months as well. The last four months mark the production season again (c.f. Figure 5.1). This annual cycle forms the groundwork for the replacement schedule and the one-year storage operation. Every year has the same injection/production pattern as shown in Figure 5.1. Projecting this arrangement onto a time span of 11 years,

a completed conversion and a one-year cycle is obtained (c.f. Figure 5.2).

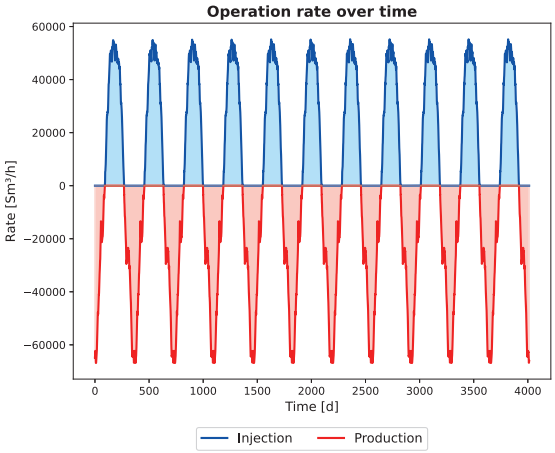

Figure 5.2: 11-year schedule (Ten-year replacement and one subsequent storage cycle)

During the conversion and subsequent storage operation, the wells follow a constant injection/production pattern to ensure a continuous storage operation procedure, performing the conversion process and simultaneously meeting the required demands. Using all wells would enable to maximize the extraction and the replacement potential of the entire storage site. Therefore, the daily injection/production rates are divided evenly over all available wells.

5.2 Results and discussion

The scheduled replacement was set to ten years and the following year represented the first full storage cycle after complete carbon

neutrality was achieved in 2045. The absence or presence of microbial activity could have a long-lasting impact on the overall hydrogen concentration. This is investigated in an abiotic and in a biochemical case with certain kinetic parameters determined in the micromodel experiments in Chapter 3.

5.2.1. Conversion and a one-year storage operation without microbial activity

After a ten-year conversion period and a one-year regular scheduled subsurface storage cycle without considering methanogenic activity, the distribution of hydrogen and natural gas are depicted in Figure 5.3.

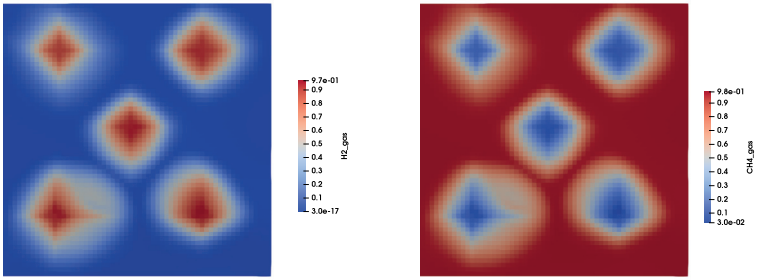

(a) H_2 distribution in the subsurface storage site after 11 years

(b) CH_4 distribution in the subsurface storage site after 11 years

Figure 5.3: Distribution of hydrogen and methane fractions after completion of the schedule

After the conversion process and the designed operational cycle, the highest hydrogen and lowest natural gas concentrations are detected in the vicinity of the wellbores. Over time, the concentrations develop in a nearly circular pattern around the well with

hydrogen concentration decreasing as the distance from the well increases. Nearly $98\,\%$ of hydrogen is in the immediate vicinity of the well, while the other gas components remain extremely low. Within the 11 years, no hydrogen front from one particular well has reached another well. Many areas of the storage site remain unaffected by the conversion process, with methane still present in these areas. Methane concentration is the lowest in the near-wellbore areas, and it increases with distance (c.f. Figures 5.3a and 5.3b). The results indicate that the storage site is not entirely occupied by hydrogen, and that a significant amount of methane remains. Due to the operational well structure, the possibility of producing additional methane from the storage site is reduced significantly. In subsequent production phases, the largest fraction of the produced gas is hydrogen, while the fractions of other components are decreasing (CH_4) or would be nearly negligible. By the end of the 11 years, the energy content of hydrogen and methane would be $1.56\,\mathrm{TWh}$ and $28.78\,\mathrm{TWh}$, respectively. The methane content would decrease by nearly $16\,\%$, and the final hydrogen-methane volume ratio is nearly $6\,\%$.

The development of the fluxes supports the trend that with every subsequent cycle, less remaining methane is produced. As the methane production values continuously decline, the hydrogen production increases with every further cycle. This also indicates that the conversion process slowly reduces in its efficiency (c.f. Figure 5.4). This is also reflected in the composition of the produced gas stream (c.f. Figure 5.5).

In the first extraction period, natural gas and carbon dioxide are the only two gases that are extracted in high quantities. After each

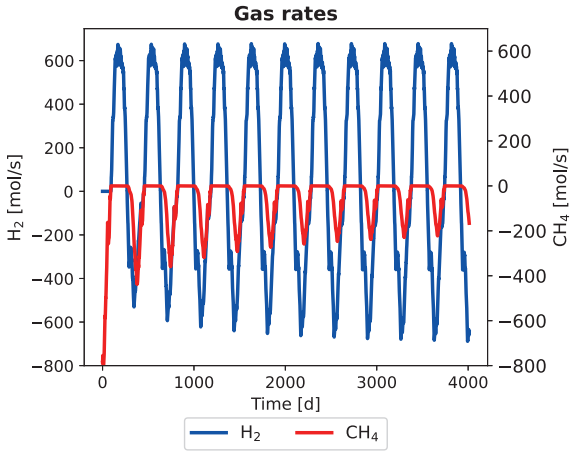

Figure 5.4: H_2 and CH_4 flux development

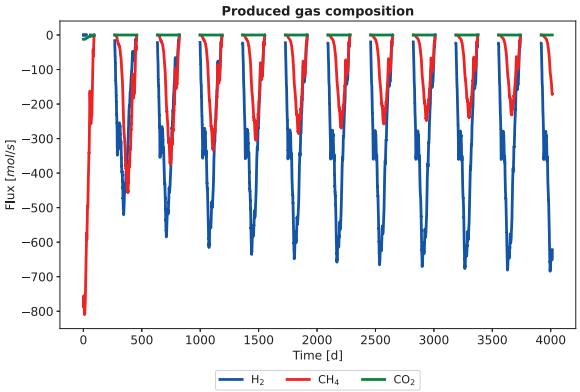

Figure 5.5: Produced gas stream composition

following hydrogen injection period, the produced methane concentration successively reduces and the hydrogen fraction continuously increases. Due to the increased hydrogen concentration in the near-wellbore area, the methane will be displaced, reducing the methane concentration, leading to a decreased methane and an increased hydrogen extraction.

The composition of the stored gas (working and cushion gas) will change with every subsequent conversion cycle. Hydrogen is injected and introduced into the stored gas. The residual methane and carbon dioxide will slowly decrease. The development of the stored gas composition is depicted in Figure 5.6.

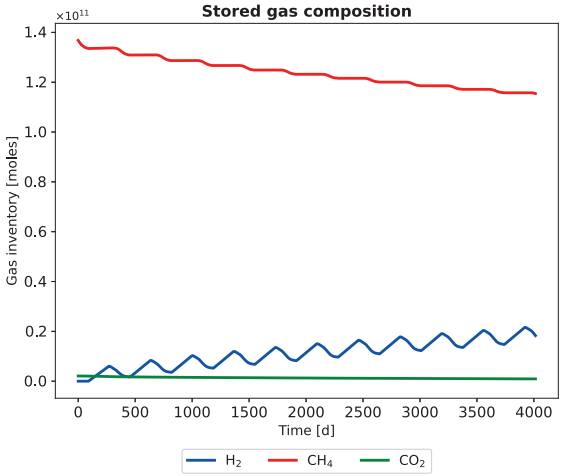

Figure 5.6: Composition of the stored gas

The largest changes in the stored gas occur in the first cycles of the operation. The methane content decreases the most, while hydrogen

increases significantly when it is injected into the subsurface. In the subsurface, it will mix with methane and carbon dioxide and the majority of hydrogen accumulates in the near-wellbore area. In each subsequent production process, the largest amount of produced gas is hydrogen and the produced methane and carbon dioxide fractions continuously decline at a much lower rate. This is reflected in the stored gas composition, as hydrogen will reach a new level after each production period. The amount of hydrogen in the working gas continues to increase slowly but it hardly appears to have any effect on the cushion gas. Methane continues to dominate the working and the cushion gas.

5.2.2. Conversion and a one-year storage operation considering biochemical reactions

The biochemically active case considers the consumption of hydrogen and the simultaneous production of methane by methanogenesis. The local methanogenic activity is dependent on the substrate concentrations in each grid cell and the microbial density within the available pore space. The input microbial kinetic parameters are:

$$\begin{aligned}
\psi_{\text{max}}^{\text{growth}} &= 1.91 \cdot 10^{-5}\ 1/\text{s}, \\
\alpha_{\text{H}_2} &= 8.9 \cdot 10^{-8}, \\
\alpha_{\text{CO}_2} &= 5.4 \cdot 10^{-6}, \\
m &= 7.5 \cdot 10^{-6}\ 1/\text{s}, \\
d &= 2 \cdot 10^{-7}\ 1/\text{s}, \\
Y &= 2.45 \cdot 10^{11}\ 1/\text{mol}.
\end{aligned}$$

These parameters were obtained from the micromodel experiment conducted at room temperature. For the initial and maximum microbial density, the following parameters were selected: $N_{Mi} = 1 \cdot 10^7$, $N_{Max} = 2 \cdot 10^{14}$ cells/m^3.

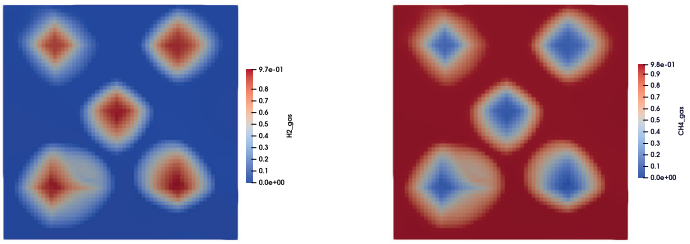

(a) H_2 distribution in the subsurface storage site after 11 years

(b) CH_4 distribution in the subsurface storage site after 11 years

Figure 5.7: Distribution of hydrogen and methane fractions after completion of the schedule

Similar to the abiotic case, the largest concentrations of hydrogen are in the near-wellbore areas, displacing the methane further into the storage site. The flow patterns of hydrogen and the concentration of methane are very similar to the sterile case. The concentration distributions have similar circular shapes as compared to the abiotic case. The microbial reactions occur in the elements where both hydrogen and carbon dioxide are present (c.f. Figures 5.7a and 5.7b).

The microbial activity occurs in the pore spaces, in the presence of hydrogen, carbon dioxide and liquid, which form a ring around each well. When the hydrogen is injected into the formation, the microbial activity begins in the near-wellbore area and gradually

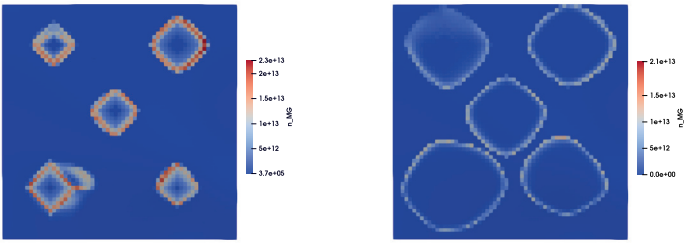

(a) Peak microbial density values (after 1 year)

(b) Microbial density within the storage site after 11 years

Figure 5.8: Microbial density at its peak value and after 11 years

spreads out into the storage site. In every additional grid element, into which hydrogen flows, the microbial number increases. The largest microbial number is attained during the first hydrogen injection period, which is completed after 1 year. The continuing permeation of hydrogen shifts the highest microbial activity areas further into the storage site. In each grid element, the microbial value attains its peak value, followed by a decrease in the microbial number. That is why in the grids, in which the peak microbial numbers have already been surpassed, microbial decay is the dominating factor. This explains the declining microbial number in the vicinity of the well shortly after the first injection cycle has ended. The microbes are already in their permanent decline, resulting in decreased activity and metabolism. As the hydrogen reaches its ultimate extent after 11 years (Figure 5.7a), a further expansion of the hydrogen gas front is very unlikely. Therefore, only the remnants of microbes with reduced metabolism continue consuming the substrates. The highest microbial activity is achieved at the end

of the first injection/production cycle, with the highest amounts of hydrogen consumed and converted to methane. With time, the overall consumption rate will decrease. Temporarily short increases in the consumption rate are noticed simultaneously with a brief increase in microbial density. In the long-run, microbial activity will decrease to a minimum (Figure 5.8b).

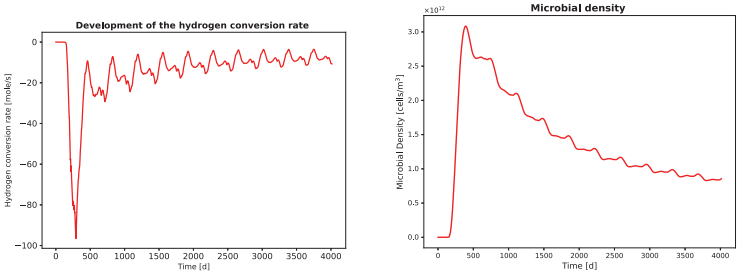

(a) Hydrogen consumption rate

(b) Microbial density development

Figure 5.9: Hydrogen consumption rate and microbial density during the conversion schedule

The conversion rate of hydrogen peaks after the end of the first injection period and strongly decreases in the subsequent production phase. The conversion rate increases with every injection phase and subsequently decreases. Over time, the magnitude of the conversion rates declines, gradually stabilizing. This constant fluctuation is caused by the quantities of hydrogen in the storage site at the respective times. When hydrogen is injected, microbial reactions are triggered. When the gas is removed, the reactions and consumption rates decline (c.f. Figure 5.9a). The conversion rates correlate to the microbial density in the storage formation. The average maximum

density is attained at the end of the first injection period. At this point, the maximum cell number in a grid cell is reached, ceasing any further growth. In the following injection phases, the hydrogen front will be driven further into the formation. Less hydrogen permeates into the grid cells which are further away from the injection well. In contact with the carbon dioxide, the consumption rates and microbial growth are reduced. The cells located closer to the well will have barely any reaction because the carbon dioxide substrate is not sufficient for microbial growth and renewed cell increase and growth after a fresh injection is highly improbable.

5.2.3. Volumetric comparison of the two storage cases

The comparison of the ten-year replacement process and the subsequent one-year storage cycle is presented in this paragraph. The development of the stored gas volumes during abiotic and biochemical reactions is of significant interest.

The hydrogen development in both storage cases shows a similar pattern, influenced by the injection and production phases. A momentarily maximum concentration is reached after each injection phase. When the ensuing production phase begins immediately afterwards, this concentration decreases. After the end of the second production phase, the biochemical hydrogen content is already significantly below the abiotic case by about 30%. The microbial impact is clearly visible as the hydrogen concentration in the biochemically-active case constantly remains below the abiotic. After the first injection period, the difference between the two cases is very small but this difference increases with every further injection phase. The methane concentrations decline only during production phases. In

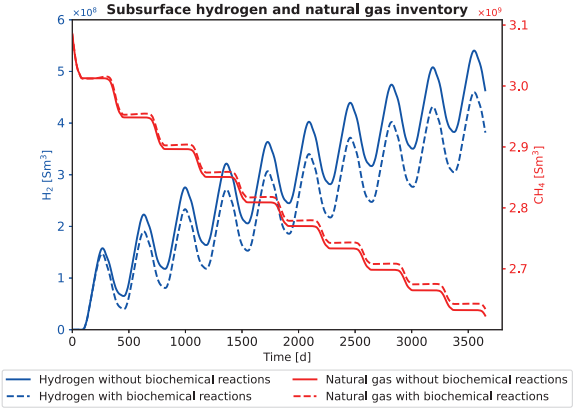

Figure 5.10: Ten-year replacement schedule considering the presence and the absence of microbial reactions

the injection phases, the natural gas concentration remains stable in the abiotic case, while a slight increase is noticed in the biochemical scenario. During the injection periods, the only noticeable increase in natural gas concentration results from the microbial activity. In the first injection phase, the microbial activity appears to be strongest, leading to a notable increase in the methane volume. In the subsequent injection phases, this increase diminishes and flattens out. After the replacement schedule, almost $4.6 \times 10^8\,\mathrm{Sm}^3$ and $3.8 \times 10^8\,\mathrm{Sm}^3$ (abiotic and biochemical) of hydrogen are inside the porous media. Simultaneously, natural gas is at $2.62 \times 10^9\,\mathrm{Sm}^3$ and $2.63 \times 10^9\,\mathrm{Sm}^3$. At the end of the biochemical conversion schedule, nearly 8% less hydrogen is stored. Simultaneously, nearly $0.4\,\%$ more natural gas will be inside the storage site (c.f. Figure 5.10).

In the one-year operation cycle, the hydrogen in the biochemical sce-

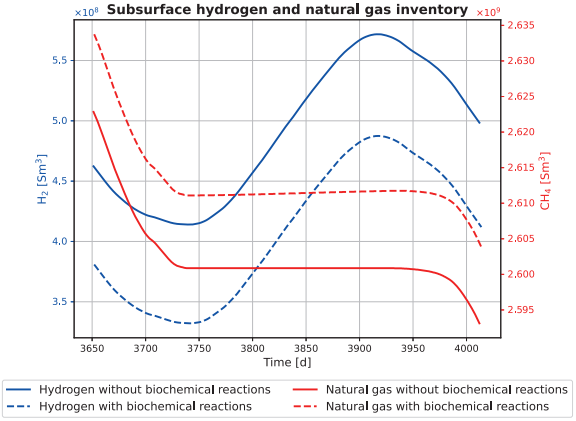

Figure 5.11: One-year subsurface operation cycle

nario permanently remains below the abiotic storage cycle. During the production and injection phases, both curves have a nearly parallel trend, although the biochemical curve has a minimally smaller slope. The abiotic methane concentration has a steeper decline in the production phases. As the first production period continues, the decline begins to flatten out. The natural gas in the biochemical scenario indicates that microbial activity at a large scale leads to an increase in the natural gas storage volume. This serves as a clear indicator of the microbial influence on the hydrogen consumption and methane production (c.f. Figure 5.11). During the injection phase, no additional influx of methane into the storage site occurs. As the methane already stored remains nearly unchanged, the slight increase in the concentration is attributed to the microbial activity and it is clearly noticed during the injection phase. The final hydrogen volumes without and with microbial activity are close to

$5.0 \times 10^8\,\mathrm{Sm}^3$ and $4.1 \times 10^8\,\mathrm{Sm}^3$, respectively. The final natural gas volumes for both cases are $2.592 \times 10^9\,\mathrm{Sm}^3$ and $2.604 \times 10^9\,\mathrm{Sm}^3$ (c.f. Figure 5.11).

5.2.4. Impact of microbial kinetic parameters

The kinetic values drive the metabolism of the methanogenic archaea and the intensity of the hydrogen consumption. Parameters, such as maximum growth rate, half-velocity constants, yield, maintenance and decay rates, influence cell growth, the maximum attainable cell number, the level of methane production and decline rate. Transferring the lab-scale to a field requires reliable upscaling methods and the consideration of various peripheral factors. One evident difference are the two system pressures: the micromodel is operated at 5 bar and the field has an initial pressure of 120 bar and a maximum value of $125\,\mathrm{bar}$. In the micromodel, the intrinsic permeability is nearly $6\,\mathrm{D}$. The field has an element-varying intrinsic permeability ranging up to $740\,\mathrm{mD}$. The field permeability is lower by a factor of 8 to the micromodel permeability. This implies that the liquid containing microbes are restricted in their flow and their distribution in the porous media. The lower pore space in the field provides less space for microbial growth, thus restricting the growth rate much earlier and more profoundly. The system pressure governs the dissolution of gaseous substrates into the liquid phase, initially resulting in an increased gas solubility at higher pressures. However, higher pressures reduce microbial mobility and can confine microbes to a limited space, reducing growth potential. The reduced mobility of the microbes limits the consumption of the dissolved substrates by newly developed cells.

The gas solubility is influenced by the temperature and pressure level. According to Henry's Law, its constant describes the solubility of gas in a liquid as a function of the partial gaseous pressure acting on it. As pressure increases, the solubility of gas into the liquid also increases. This leads to a higher amount of dissolved substrates within the liquid phase for microbial consumption. The pressure increase can support higher microbial reaction rates up to nearly $50\,\mathrm{MPa}$ and at a temperature of 65 °C, as it has been observed in stirred-batch experimental literature. Nevertheless, elevated pressures and temperatures increase the likelihood of cell degradation, which can offset the increased microbial growth rates [6]. The effects of higher temperatures and pressures in porous rocks require further investigation. In addition to these mentioned effects, the accumulation of microbes inside the pores of the porous rocks is dependent on the sizes of the pores. Considering that a methanogenic cell has a diameter of 2 $\mu\mathrm{m}$, pore diameters below this threshold value would be inaccessible for the cells. In the micromodel experiments in Chapter 3, all pores and throats were large enough so that the microbes could enter all of them. The permeability in the field model is significantly lower, thereby implying that some pores might be too small for microbes to enter. Experiments by Khajooie have revealed decreasing microbial consumption rates of hydrogen as the pore volume of rock decreases. The reaction rate was tied to the flux of mass-transfer across the gas-liquid interface which appears to decrease with lower pore-volume. Restrictions in diffusion across the gas-liquid interface contribute to lower reaction rates, providing another explanation for the lower reaction rates at the field scale [56].

Another factor is the different composition of the injection flux

between the micromodel experiments and the field scale. At the laboratory scale, a constant influx of hydrogen and carbon dioxide at a constant ratio was ensured, which provided unlimited amount of substrates. In the field-scale storage simulation, pure hydrogen was injected and the only source of carbon dioxide was the remaining quantity present inside the storage formation. The ratio of the two gases are not at a constant ratio, further contributing to lower microbial reaction rates. The repeated injection of pure hydrogen into the storage formation continuously decreases the carbon dioxide fraction, reducing the overall hydrogen consumption in the long-run. The differences in rock properties and the environmental conditions reduce the direct transferability of the experimentally determined micromodel parameters to the field scale. Adequate upscaling techniques to reliably project these kinetic parameters are necessary. To address this mismatch, a selection of parameters considered most transferable was supplemented with three other factors obtained from literature. The latter ones were the initial and maximum microbial values and the substrate half-velocity constants. The remaining kinetic parameters from the micromodel experiment conducted at 25 °C were transmitted directly to the field scale.

5.3 Summary

In this chapter, the grid model presented in Chapter 4 was initialized with methane and carbon dioxide. An injection/production schedule was applied to this storage site to simulate a 10-year conversion and a subsequent one-year operation cycle with hydrogen. Two cases were analyzed: one case assuming no microbial reactions and one considering methanogenic processes with parameters deter-

mined in Chapter 3. The development of the volumes of hydrogen and methane for both cases were compared. The key findings of this chapter are:

- The presence or the absence of microbial reactions had an evident influence on the concentrations of hydrogen and methane. Assuming active microbes, the stored volume of hydrogen was slightly lower than in the abiotic case (by approximately 15%). In the abiotic case, methane had a slightly lower value than in the biochemical scenario.
- All kinetic parameters determined in the micromodel experiments in Chapter 3 could not be directly transferred to the field-scale simulation model. These parameters had to be significantly reduced and adjusted to achieve a stable simulation process. For instance, the numerically determined simulation values for the micromodel experiment at 62 °C did not last for the entire field-scale simulation. Reducing the maximum growth rate, adjusting the microbial density numbers, and applying parameters from the experiment conducted at a lower temperature provided more reliable results.
- The injection and production pattern used for the field conversion and storage cycle resulted in a very small amount of natural gas that was replaced. This ratio stood at 6%, making this operation methodology ineffective. For a more efficient replacement and operation scenario, a different pattern should be selected. A system in which the hydrogen is injected via designated injection wells and displaces the already stored gas towards producing wells is preferable.

- During the conversion and subsequent storage operation, microbial reactions can have a vital influence on the development of the storage volumes. Biochemical reactions lead to a reduction in the total hydrogen storage quantities, effectively reducing the storage efficiency. To assess a storage formation's feasibility and its potential biochemical reactions, each storage site requires a detailed microbial analysis.

Chapter 6

Conclusion

In this PhD work, the importance of hydrogen for the energy transition and future energy supply as well as the potential to store large quantities of it in existing subsurface storage facilities is evaluated. The effects of hydrogen characteristics on the gas withdrawal process from the subsurface storage site, and its susceptibility to biochemical reactions are vital considerations that need to be addressed when an existing storage site is repurposed to store hydrogen. These aspects were examined by performing an analytical withdrawal comparison of a hypothetical underground natural gas and hydrogen storage site. Methanogenic reactions in quasi-two-dimensional micromodels, the relevant kinetic parameters obtained through numerical simulations and an assessment of the microbial influence on a long-term subsurface storage conversion process were compared. The most important findings are the following:

- The characteristics of natural gas and hydrogen are very different. That affects not only the total volume to be stored inside the subsurface storage formation but also the extraction behavior of the respective gases. The introduced analytical approach provided a unique in-depth method to quantitatively assess the effect of gas properties on the withdrawal behavior by modifying individual gas parameters. This assessment revealed that the compressibility factor, the molar mass and the viscosity were the most influential properties on

the withdrawal rate. The differences in those properties result in a stored volume of natural gas which is nearly three times larger than that of hydrogen. Taking into consideration the calorific values for each gas, the energy content of hydrogen is decreased by almost three-quarters. When a well produces at its maximum limit, this maximum rate can be sustained longer for a natural gas subsurface storage site than for hydrogen. After the bottom-hole flowing pressure falls below its minimum value, the production rates begin to decline stepwise according to the pressure difference between p_{wf} and p_e. Hydrogen withdrawal rates decline quicker and at a steeper rate than those for natural gas. Not only does the pressure difference have an impact, gas parameters and well skin factors are also contributing.

- The microfluidic experimental concept to examine methanogenic archaea in a hydrogen-carbon dioxide environment accomplished two objectives: the visual observation of the microbial density and the simultaneous gas analysis of the biochemical reactions. According to the author's knowledge, this is the first approach of this kind ever conducted. This method developed a direct, quasi-simultaneous correlation between the microbial number and the produced methane. It also provided a unique insight into real subsurface microbial behavior. The maximum microbial density was only attained once in the experiment, and that occurred in the first injection phase of hydrogen and carbon dioxide. Subsequent renewed phases of gas injection did not trigger any farther increase in the microbial number. This observation correlated with

the produced methane. This peak was attained once and after a period of decrease, the methane appeared to stabilize at a minimum value. The growth rate of microbes, the consumption speed and the microbial decay are directly influenced by temperature.

- The simulation revealed that microbial development and methane generation were influenced by the available pore space and by the maximum attainable microbial number. Implementing the limiting function term in the growth and bioreactive kinetic equation reliably replicated the experimental microbial density and produced methane values. This implementation is a vital addition to the understanding of limits in biochemical processes.
- The implementation of obtained values from the micromodel into the field-scale storage site requires a precise selection of parameters that can be directly transferred. Restrictions and intrinsic differences between the two scales limited the transferability between the scales. Some differences were the spatial distribution of the pore spaces (artificial linear circle and real heterogeneous grains) as well as the operating pressures. Due to the non-uniform pore shapes in the real rock, high pressures can develop. Limitations in mass transfer via the gas-liquid interface and gas dissolution were likely to substantially influence the parameters between the scales.
- In the storage site conversion and annual operational cycle, the microbial activity had a long-lasting impact on the stored gas' quantity and quality. Depending on the environmental

conditions and the microbial species, the biochemical effects on a subsurface hydrogen storage operation could be quite significant. The susceptibility of a storage site to microbial reactions needs to be evaluated on a site-specific basis. To better predict the field-scale microbial impact on a hydrogen conversion scenario, this model requires parameter calibration using operational field data. The conversion of an existing gas storage considering flow physics and subsurface microbiology site can be effectively and successfully performed using an efficient well injection/production strategy, enabling the maximization of the available storage space for hydrogen storage in the future.

Bibliography

[1] A. Aftab, A. Hassanpouryouzband, Q. Xie, L. L. Machuca, and M. Sarmadivaleh. "Toward a Fundamental Understanding of Geological Hydrogen Storage". In: *Industrial & Engineering Chemistry Research* 61.9 (Mar. 2022), pp. 3233–3253. ISSN: 0888-5885, 1520-5045. DOI: 10.1021/acs.iecr.1c04380. URL: https://pubs.acs.org/doi/10.1021/acs.iecr.1c04380 (visited on 11/06/2025).

[2] K. Alms, M. Berndsen, A. Groeneweg, M. Graf, M. Nehler, and B. Ahrens. "Underground Hydrogen Storage in the Bunter Sandstone Formation in the North German Basin: Capacity Assessment and Geochemical Modeling". In: *Energy Technology* 13.2 (Feb. 2025), p. 2300847. ISSN: 2194-4288, 2194-4296. DOI: 10.1002/ente.202300847. URL: https://onlinelibrary.wiley.com/doi/10.1002/ente.202300847 (visited on 11/06/2025).

[3] S. Bauer. *Underground Sun Storage*. Final Report. Vienna, Austria: RAG-Austria, Oct. 31, 2017, p. 187.

[4] BDEW. *Welche Rolle Wasserstoff künftig spielen wird*. URL: https://www.bdew.de/energie/erneuerbare-energien/wasserstoff-energieerzeugung/ (visited on 03/17/2026).

[5] R. C. Beaver and J. D. Neufeld. "Microbial Ecology of the Deep Terrestrial Subsurface". In: *The ISME Journal* 18.1 (Jan. 8, 2024), wrae091. ISSN: 1751-7362, 1751-7370. DOI: 10.1093/ismejo/wrae091. URL: https://academic.oup.com/ismej/

article/doi/10.1093/ismejo/wrae091/7680289 (visited on 04/10/2025).

[6] G. Bernhardt, R. Jaenicke, H.-D. Lüdemann, H. König, and K. O. Stetter. "High Pressure Enhances the Growth Rate of the Thermophilic Archaebacterium *Methanococcus Thermolithotrophicus* without Extending Its Temperature Range". In: *Applied and Environmental Microbiology* 54.5 (May 1988), pp. 1258–1261. ISSN: 0099-2240, 1098-5336. DOI: 10.1128/aem.54.5.1258-1261.1988. URL: https://journals.asm.org/doi/10.1128/aem.54.5.1258-1261.1988 (visited on 03/12/2026).

[7] E. C. Boersheim, V. Reitenbach, D. Albrecht, D. Pudlo, and L. Ganzer. "Experimental Investigation of Integrity Issues of UGS Containing Hydrogen". In: *SPE Europec Featured at 81st EAGE Conference and Exhibition*. London, England, UK: SPE, June 2019, D041S008R001. DOI: 10.2118/195555-MS. URL: https://onepetro.org/SPEEURO/proceedings/19EURO/19EURO/D041S008R001/217950 (visited on 11/06/2025).

[8] M. Bouteldja, T. Acosta, B. Carlier, A. Reveillere, H. Jannel, and C. Fournier. *Definition of Selection Criteria for a Hydrogen Storage Site in Depleted Fields or Aquifers*. Mar. 5, 2021. URL: https://hystories.eu/wp-content/uploads/2021/05/D1.1-0-Selection-criteria-for-H2-storage-sites.pdf (visited on 03/19/2026).

[9] V. Brkić, I. Zelenika, P. Mijić, and I. Medved. "Underground Gas Storage Process Optimisation with Respect to Reservoir Parameters and Production Equipment". In: *Energies* 14.14 (July 2021), p. 4324. ISSN: 1996-1073. DOI: 10.3390/

en14144324. URL: https://www.mdpi.com/1996-1073/14/14/4324 (visited on 10/26/2025).

[10] H. Bültemeier, B. Keßler, J. Hüttenrauch, J. Sperlich, M. Kühn, M. Schlichtenmayer, T. Wagler, O. Kruck, G.-S. Schneider, C. Abdel Haq, T. Bayer, K. Faatz, T. Faber, A. Frommhold, D. Miersch, M. Schwabe, L. Städtke, and J. Zemke. "Wasserstoff speichern - soviel ist sicher". In: *DVGW Deutscher Verein des Gas- und Wasserfaches e.V.* (June 2022). URL: https://www.dvgw.de/medien/dvgw/forschung/berichte/g201926-kurzfassung-transformation-ugs.pdf (visited on 05/15/2026).

[11] Bundesverband der Deutschen Industrie. *Klimapfade 2.0 – Ein Wirtschaftsprogramm für Klima und Zukunft*. Ed. by Bundesverband der Deutschen Industrie. URL: https://bdi.eu/publikation/news/klimapfade-2-0-ein-wirtschaftsprogramm-fuer-klima-und-zukunft/.

[12] F. Buzek, V. Onderka, P. Vancura, and I. Wolf. "Carbon Isotope Study of Methane Production in a Town Gas Storage Reservoir". In: *Fuel* 73.5 (May 1994), pp. 747–752. ISSN: 00162361. DOI: 10.1016/0016-2361(94)90019-1. URL: https://linkinghub.elsevier.com/retrieve/pii/0016236194900191 (visited on 03/18/2026).

[13] *BVEG Leitfaden Bohrungsintegrität*. July 2021. URL: https://www.bveg.de/wp-content/uploads/2021/09/BVEG-Leitfaden-Bohrungsintegritaet_Technische-Regel.pdf.

[14] A. Cavanagh, H. Yousefi, M. Wilkinson, and R. Groenenberg. *Hydrogen Underground Storage in Porous Reservoirs - Hydrogen*

storage potential of existing European gas storage sites in depleted gas fields and aquifers. 2022.

[15] S. P. Chan, M. Ji, X. G. Gong, and Z. F. Liu. "Pressure-Driven Confinement of Hydrogen Molecules between Graphene Sheets in the Regime of van Der Waals Repulsion". In: *Physical Review B* 69.9 (Mar. 2004), p. 092101. ISSN: 1098-0121, 1550-235X. DOI: 10.1103/PhysRevB.69.092101. URL: https://link.aps.org/doi/10.1103/PhysRevB.69.092101 (visited on 11/05/2025).

[16] Concoa. *Hydrogen properties*. 2023. URL: https://www.concoa.com/hydrogen_properties.html.

[17] H. Cypionka. *Grundlagen Der Mikrobiologie*. Springer-Lehrbuch. Berlin, Heidelberg: Springer Berlin Heidelberg, 2010. ISBN: 978-3-642-05095-4 978-3-642-05096-1. DOI: 10.1007/978-3-642-05096-1. URL: http://link.springer.com/10.1007/978-3-642-05096-1 (visited on 04/04/2026).

[18] P. Deng, Z. Chen, X. Peng, S. Zhu, B. Liu, X. Lei, and C. Di. "Converting Underground Natural Gas Storage for Hydrogen: A Review of Advantages, Challenges and Economics". In: *Renewable and Sustainable Energy Reviews* 213 (May 1, 2025), p. 115438. ISSN: 1364-0321. DOI: 10.1016/j.rser.2025.115438. URL: https://www.sciencedirect.com/science/article/pii/S136403212500111X (visited on 04/04/2026).

[19] *DIN EN 1918-1:2016-11, Gasinfrastruktur_- Untertagespeicherung von Gas_- Teil_1: Funktionale Empfehlungen Für Die Speicherung in Aquiferen; Deutsche Fassung EN_1918-1:2016*.

DOI: 10.31030/2350410. URL: https://www.dinmedia.de/de/-/-/240619276 (visited on 11/06/2025).

[20] *DIN EN 1918-2:2016-11, Gasinfrastruktur_- Untertagespeicherung von Gas_- Teil_2: Funktionale Empfehlungen Für Die Speicherung in Öl- Und Gasfeldern; Deutsche Fassung EN_1918-2:2016*. DOI: 10.31030/2350411. URL: https://www.dinmedia.de/de/-/-/240619313 (visited on 11/06/2025).

[21] *DIN EN 1918-3:2016-11, Gasinfrastruktur_- Untertagespeicherung von Gas_- Teil_3: Funktionale Empfehlungen Für Die Speicherung in Gesolten Salzkavernen; Deutsche Fassung EN_1918-3:2016*. DOI: 10.31030/2350412. URL: https://www.dinmedia.de/de/-/-/240619344 (visited on 11/06/2025).

[22] H. J. Doddema and G. D. Vogels. "Improved Identification of Methanogenic Bacteria by Fluorescence Microscopy". In: *Applied and Environmental Microbiology* 36.5 (Nov. 1978), pp. 752–754. ISSN: 0099-2240, 1098-5336. DOI: 10.1128/aem.36.5.752-754.1978. URL: https://journals.asm.org/doi/10.1128/aem.36.5.752-754.1978 (visited on 02/24/2026).

[23] DVGW. *Wasserstoffspeicher: Potenziale, Herausforderungen Und Ausblick - Eine Kurzstudie*. Oct. 22, 2025. URL: https://www.dvgw.de/medien/dvgw/leistungen/publikationen/kurzstudie-wasserstoffspeicher-dvgw.pdf (visited on 05/15/2026).

[24] A. Ebigbo, F. Golfier, and M. Quintard. "A Coupled, Pore-Scale Model for Methanogenic Microbial Activity in Un-

derground Hydrogen Storage". In: *Advances in Water Resources* 61 (Nov. 2013), pp. 74–85. ISSN: 03091708. DOI: 10.1016/j.advwatres.2013.09.004. URL: https://linkinghub.elsevier.com/retrieve/pii/S0309170813001565 (visited on 02/19/2026).

[25] N. Eddaoui, M. Panfilov, L. Ganzer, and B. Hagemann. "Impact of Pore Clogging by Bacteria on Underground Hydrogen Storage". In: *Transport in Porous Media* 139.1 (Aug. 2021), pp. 89–108. ISSN: 0169-3913, 1573-1634. DOI: 10.1007/s11242-021-01647-6. URL: https://link.springer.com/10.1007/s11242-021-01647-6 (visited on 04/07/2026).

[26] A. J. Effiong, B. Nojabaei, and R. Pandey. "Coupled Methanogenesis and Sulfate Reduction Reactions: Implications for Underground Hydrogen Storage Stability". In: *Gas Science and Engineering* 149 (May 2026), p. 205864. ISSN: 29499089. DOI: 10.1016/j.jgsce.2026.205864. URL: https://linkinghub.elsevier.com/retrieve/pii/S2949908926000282 (visited on 04/07/2026).

[27] S. T. O. R. A. G. ETZEL. *H2CAST Grüner Wasserstoff – Speicherung in Etzel*. June 21, 2022. URL: https://www.storag-etzel.de/speicher/wasserstoff-h2cast (visited on 03/30/2026).

[28] Facts about Germany. *Energy Transition – A Project for Generations*. 12.06.2023. URL: https://www.tatsachen-ueber-deutschland.de/en/climate-and-energy/energy-transition-project-generations.

[29] O. Flanigan. *Underground Gas Storage Facilities: Design and Implementation*. Houston: Gulf Pub. Co, 1995. ISBN: 978-0-88415-204-0.

[30] *Forschungsplattform Geoenergiesysteme - EFZN*. URL: https://www.efzn.de/ten/geoenergiesysteme (visited on 03/19/2026).

[31] L. Ganzer, V. Reitenbach, B. Hagemann, G. Strobel, R. Peitz, C. Boersheim, J. Oppelt, and I. o. S. E. S. Technische Universität Clausthal. *Verbundvorhaben HyINTEGER: Untersuchungen Zur Integrität von Bohrungen Und Technischen Materialien in Geologischen H2-Untergrundreservoiren; Teilprojekt: Experimentelle Und Numerische Untersuchungen Der Technischen Integrität von UGS-Bohrungen (TP2, TP4, TP6) : Abschlussbericht HyINTEGER : Berichtszeitraum: 01.01.2016-30.09.2019*. Clausthal-Zellerfeld, 2019. DOI: 10.2314/KXP:1736133926.

[32] C. L. Gaol, J. Wegner, and L. Ganzer. "Real Structure Micromodels Based on Reservoir Rocks for Enhanced Oil Recovery (EOR) Applications". In: *Lab on a Chip* 20.12 (2020), pp. 2197–2208. ISSN: 1473-0197, 1473-0189. DOI: 10.1039/D0LC00257G. URL: https://xlink.rsc.org/?DOI=D0LC00257G (visited on 02/24/2026).

[33] *GIE AGSI - Aggregated Gas Storage Inventory*. May 2025. URL: https://agsi.gie.eu/.

[34] *Global Energy Perspective 2023: Hydrogen Outlook | McKinsey*. URL: https://www.mckinsey.com/industries/oil-and-gas/our-insights/global-energy-perspective-2023-hydrogen-outlook (visited on 05/15/2026).

[35] T. Groß, P. Dunkel, D. Franzmann, H. Heinrichs, J. Linßen, and D. Stolten. *Report on H2 Supply from Renewable Energy Sources, H2 Demand Centers and H2 Transport Infrastructure*. 2022.

[36] B. Hagemann. "Numerical and Analytical Modeling of Gas Mixing and Bio-Reactive Transport during Underground Hydrogen Storage". PhD thesis. MyCoRe Community, 2018. DOI: 10.21268/20180116-085820. URL: https://dokumente.ub.tu-clausthal.de/receive/clausthal_mods_00000546 (visited on 11/08/2025).

[37] C. Hebling, M. Ragwitz, T. Fleiter, U. Groos, D. Härle, A. Held, M. Jahn, N. Müller, T. Pfeifer, P. Plötz, O. Ranzmeyer, A. Schaadt, F. Sensfuß, T. Smolinka, and M. Wietschel. *Eine Wasserstoff-Roadmap Für Deutschland*. Karlsruhe and Freiburg: Fraunhofer-Institut für System- und Innovationsforschung ISI, Karlsruhe; Fraunhofer-Institut für Solare Energiesysteme ISE, Freiburg, Oct. 2019. URL: https://www.ise.fraunhofer.de/de/veroeffentlichungen/studien/wasserstoff-roadmap-deutschland.html.

[38] N. Heinemann, J. Alcalde, J. M. Miocic, S. J. T. Hangx, J. Kallmeyer, C. Ostertag-Henning, A. Hassanpouryouzband, E. M. Thaysen, G. J. Strobel, C. Schmidt-Hattenberger, K. Edlmann, M. Wilkinson, M. Bentham, R. S. Haszeldine, R. Carbonell, and A. Rudloff. "Enabling Large-Scale Hydrogen Storage in Porous Media – the Scientific Challenges". In: *Energy & Environmental Science* 14.2 (Feb. 23, 2021), pp. 853–864. ISSN: 1754-5706. DOI: 10.1039/D0EE03536J. URL: https:

//pubs.rsc.org/en/content/articlelanding/2021/ee/d0ee03536j (visited on 03/19/2026).

[39] S. Hogeweg. "Numerical Investigations of Reactive Transport Processes during the Storage of Hydrogen in the Porous Subsurface". MyCoRe Community, July 15, 2024. DOI: 10.21268/20240603-0. URL: https://dokumente.ub.tu-clausthal.de/receive/clausthal_mods_00002649 (visited on 04/04/2026).

[40] S. Hogeweg, J. Michelsen, B. Hagemann, and L. Ganzer. "Empirical and Numerical Modelling of Gas–Gas Diffusion for Binary Hydrogen–Methane Systems at Underground Gas Storage Conditions". In: *Transport in Porous Media* (Dec. 1, 2023). ISSN: 0169-3913, 1573-1634. DOI: 10.1007/s11242-023-02039-8. URL: https://link.springer.com/10.1007/s11242-023-02039-8 (visited on 12/02/2023).

[41] S. Hogeweg, G. Strobel, and B. Hagemann. "Benchmark study for the simulation of Underground Hydrogen Storage operations". en. In: *Computational Geosciences* 26.6 (Dec. 2022), pp. 1367–1378. ISSN: 1420-0597, 1573-1499. DOI: 10.1007/s10596-022-10163-5. URL: https://link.springer.com/10.1007/s10596-022-10163-5 (visited on 01/09/2025).

[42] *Home | Underground Sun Storage 2030*. URL: https://www.uss-2030.at/en (visited on 03/19/2026).

[43] *HPC Krummhörn | Uniper*. URL: https://www.uniper.energy/de/hydrogen-pilot-cavern (visited on 03/30/2026).

[44] H. Huber, M. Thomm, H. König, G. Thies, and K. O. Stetter. "Methanococcus Thermolithotrophicus, a Novel Ther-

mophilic Lithotrophic Methanogen". In: *Archives of Microbiology* 132.1 (July 1982), pp. 47–50. ISSN: 0302-8933, 1432-072X. DOI: 10.1007/BF00690816. URL: http://link.springer.com/10.1007/BF00690816 (visited on 02/19/2026).

[45] A. Hussain, H. Al-Hadrami, H. Emadi, F. Altawati, S. R. Thiyagarajan, and M. Watson. "Experimental Investigation of Wellbore Integrity of Depleted Oil and Gas Reservoirs for Underground Hydrogen Storage". In: *Day 2 Tue, May 03, 2022*. OTC, 5022022. DOI: 10.4043/32003-MS.

[46] *HyStorage | Uniper*. URL: https://www.uniper.energy/de/hystorage (visited on 03/30/2026).

[47] M. Ibukun, E. Elyan, M. Amish, J. Njuguna, and G. F. Oluyemi. "A Review of Well Life Cycle Integrity Challenges in the Oil and Gas Industry and Its Implications for Sustained Casing Pressure (SCP)". en. In: *Energies* 17.22 (Nov. 2024), p. 5562. ISSN: 1996-1073. DOI: 10.3390/en17225562. URL: https://www.mdpi.com/1996-1073/17/22/5562 (visited on 10/04/2025).

[48] IEA. *Global Hydrogen Review 2022*. Ed. by IEA. Paris, 2022. URL: https://www.iea.org/reports/global-hydrogen-review-2022.

[49] IEA. *World Energy Outlook 2025*. Tech. rep. Paris, 2025. URL: https://www.iea.org/reports/world-energy-outlook-2025 (visited on 03/17/2026).

[50] A. Jahanbakhsh, A. Louis Potapov-Crighton, A. Mosallanezhad, N. Tohidi Kaloorazi, and M. M. Maroto-Valer. "Underground Hydrogen Storage: A UK Perspective". In:

Renewable and Sustainable Energy Reviews 189 (Jan. 1, 2024), p. 114001. ISSN: 1364-0321. DOI: 10.1016/j.rser.2023.114001. URL: https://www.sciencedirect.com/science/article/pii/S1364032123008596 (visited on 03/19/2026).

[51] E. C. Jian Jun, H. C. Y. Foo, H. K. Ben Mahmud, L. S. Wei, and Z. Bennour. "Cement Integrity Challenges Associated with Underground Hydrogen Storage: A Review of Geochemistry and Microbial Activity". In: *Renewable and Sustainable Energy Reviews* 228 (Mar. 2026), p. 116567. ISSN: 13640321. DOI: 10.1016/j.rser.2025.116567. URL: https://linkinghub.elsevier.com/retrieve/pii/S1364032125012407 (visited on 04/07/2026).

[52] J. Juez-Larré, C. Gonçalves Machado, R. M. Groenenberg, S. S. Belfroid, and S. H. Yousefi. "A Detailed Comparative Performance Study of Underground Storage of Natural Gas and Hydrogen in the Netherlands". In: *International Journal of Hydrogen Energy* 48.74 (Aug. 2023), pp. 28843–28868. ISSN: 03603199. DOI: 10.1016/j.ijhydene.2023.03.347. URL: https://linkinghub.elsevier.com/retrieve/pii/S0360319923014933 (visited on 01/09/2025).

[53] F. Karadagli and B. E. Rittmann. "Kinetic Characterization of Methanobacterium Bryantii M.o.H." In: *Environmental Science & Technology* 39.13 (July 1, 2005), pp. 4900–4905. ISSN: 0013-936X. DOI: 10.1021/es047993b. URL: https://doi.org/10.1021/es047993b (visited on 04/07/2026).

[54] D. L. V. Katz and R. L. Lee. *Natural Gas Engineering: Production and Storage*. McGraw-Hill Chemical Engineering Series.

New York St. Louis San Francisco [etc.]: McGraw-Hill, 1990. ISBN: 978-0-07-033352-9.

[55] G. Kaya and A. Dahi Taleghani. "Integrity Issues for Underground Gas Storage Wells". In: *ASME Open Journal of Engineering* 4 (Jan. 2025), p. 040804. ISSN: 2770-3495. DOI: 10.1115/1.4067764. URL: https://asmedigitalcollection.asme.org/openengineering/article/doi/10.1115/1.4067764/1212696/Integrity-Issues-for-Underground-Gas-Storage-Wells (visited on 11/10/2025).

[56] S. Khajooie, G. Gaus, T. Seemann, J. Klaver, H. Claes, M. Nehler, B. Ahrens, and R. Littke. "Methanogenic Activity in Water-Saturated Reservoir Analogues for Underground Hydrogen Storage: The Role of Surface Area". In: *International Journal of Hydrogen Energy* 90 (Nov. 2024), pp. 171–190. ISSN: 03603199. DOI: 10.1016/j.ijhydene.2024.09.395. URL: https://linkinghub.elsevier.com/retrieve/pii/S0360319924041211 (visited on 03/12/2026).

[57] M. Kruse and J. Wedemeier. "Potenzial grüner Wasserstoff: langer Weg der Entwicklung, kurze Zeit bis zur Umsetzung". In: *Wirtschaftsdienst* 101.1 (2021), pp. 26–32. ISSN: 0043-6275. DOI: 10.1007/s10273-021-2821-9.

[58] G. Lackey, G. M. Freeman, T. A. Buscheck, F. Haeri, J. A. White, N. Huerta, and A. Goodman. "Characterizing Hydrogen Storage Potential in U.S. Underground Gas Storage Facilities". In: *Geophysical Research Letters* 50.3 (2023), e2022GL101420. ISSN: 1944-8007. DOI: 10.1029/2022GL101420. URL: https://onlinelibrary.wiley.com/doi/abs/10.1029/2022GL101420 (visited on 04/04/2026).

[59] Landesamt für Bergbau, Energie und Geologie. *Erdöl Und Erdgas in Der Bundesrepublik Deutschland 2024*. June 2025. DOI: 10.48476/GEOBER_49_2025. URL: https://nibis.lbeg.de/doi/DOI.aspx?doi=10.48476/geober_49_2025 (visited on 02/20/2026).

[60] A. Levikhin and Boryaev. "Physical Properties and Thermodynamic Characteristics of Hydrogen". In: *Heliyon* 10.17 (Sept. 2024), e36414. ISSN: 24058440. DOI: 10.1016/j.heliyon.2024.e36414. URL: https://linkinghub.elsevier.com/retrieve/pii/S2405844024124450 (visited on 10/03/2025).

[61] Q. Li, I. D. Gates, and S. H. Hejazi. "Experimental Investigation of Caprock Sealing Capacity for Underground Hydrogen Storage". In: *International Journal of Hydrogen Energy* 165 (Sept. 5, 2025), p. 150858. ISSN: 0360-3199. DOI: 10.1016/j.ijhydene.2025.150858. URL: https://www.sciencedirect.com/science/article/pii/S0360319925038583 (visited on 05/15/2026).

[62] A. Lindermeir, ed. *H2-Wegweiser Niedersachsen: Energiesystemanalyse zur technischen, wirtschaftlichen und gesellschaftlichen Integration, Speicherung und Konversion von Wasserstoff in Niedersachsen: Schlussbericht: Laufzeit des Verbundprojektes: 01.05.2024 bis zum 31.08.2024*. 1. Auflage. Schriftenreihe des Energie-Forschungszentrums Niedersachsen (EFZN) Band 83. Göttingen: Cuvillier Verlag, 2024. ISBN: 978-3-68952-945-1.

[63] N. Liu, A. R. Kovscek, M. A. Fernø, and N. Dopffel. "Pore-Scale Study of Microbial Hydrogen Consumption and Wettability Alteration during Underground Hydrogen Storage".

In: *Frontiers in Energy Research* 11 (Feb. 6, 2023), p. 1124621. ISSN: 2296-598X. DOI: 10.3389/fenrg.2023.1124621. URL: https://www.frontiersin.org/articles/10.3389/fenrg.2023.1124621/full (visited on 03/19/2026).

[64] Z. Liu, Y. Liu, and Z. Wang. "Comparative Study of Temperature and Pressure Variation Patterns in Hydrogen and Natural Gas Storage in Salt Cavern". In: *Applied Sciences* 14.19 (Oct. 2024), p. 9005. ISSN: 2076-3417. DOI: 10.3390/app14199005. URL: https://www.mdpi.com/2076-3417/14/19/9005 (visited on 11/05/2025).

[65] J. Lohrenz, B. G. Bray, and C. R. Clark. "Calculating Viscosities of Reservoir Fluids From Their Compositions". In: *Journal of Petroleum Technology* 16.10 (Oct. 1964), pp. 1171–1176. ISSN: 0149-2136, 1944-978X. DOI: 10.2118/915-PA. URL: https://onepetro.org/JPT/article/16/10/1171/160011/Calculating-Viscosities-of-Reservoir-Fluids-From (visited on 09/05/2025).

[66] C. T. Lüddeke, B. Hagemann, and L. Ganzer. "Conversion of Underground Gas Storages to Hydrogen: Impact on Storage Integrity, Capacity and Deliverability". In: *EAGE GET 2022* 2022.1 (2022), pp. 1–5. ISSN: 2214-4609. DOI: 10.3997/2214-4609.202221056. URL: https://www.earthdoc.org/content/papers/10.3997/2214-4609.202221056.

[67] C. T. Lüddeke, C. L. Gaol, G. J. Strobel, and L. Ganzer. "Experimental and Analytical Investigation of an Immiscible Displacement Process in Real Structure Micromodels". In: *Energies* 15.18 (Sept. 2022), p. 6741. ISSN: 1996-1073. DOI:

10.3390/en15186741. URL: https://www.mdpi.com/1996-1073/15/18/6741 (visited on 02/24/2026).

[68] C. T. Lüddeke, B. Hagemann, and L. Ganzer. "Subsurface Gas Storage in Porous Reservoirs: A Comparison of Working Gas Capacity, Deliverability and Production between Hydrogen and Natural Gas". In: *Frontiers in Energy Research* 13 (Jan. 2026), p. 1704183. ISSN: 2296-598X. DOI: 10.3389/fenrg.2025.1704183. URL: https://www.frontiersin.org/articles/10.3389/fenrg.2025.1704183/full (visited on 02/16/2026).

[69] M. T. Madigan, K. S. Bender, D. H. Buckley, W. M. Sattley, and D. A. Stahl. *Brock Biology of Microorganisms*. Sixteenth edition, global edition. Harlow: Pearson Education Limited, 2022. 1 p. ISBN: 978-1-292-40506-3.

[70] M. T. Madigan, K. S. Bender, D. H. Buckley, W. M. Sattley, and D. A. Stahl. *Brock Biology of Microorganisms*. Fifteenth edition. NY, NY: Pearson, 2018. 1022 pp. ISBN: 978-0-13-426192-8.

[71] P. Miga. "Methanogenic Bacteria as a Key Factor Involved in Changes of Town Gas Stored in an Underground Reservoir". In: *FEMS Microbiology Letters* 73.3 (Apr. 1990), pp. 221–224. ISSN: 03781097. DOI: 10.1016/0378-1097(90)90733-7. URL: http://doi.wiley.com/10.1016/0378-1097(90)90733-7 (visited on 03/18/2026).

[72] J. Monod. "THE GROWTH OF BACTERIAL CULTURES". In: *Annual Review of Microbiology* 3.1 (Oct. 1949), pp. 371–394. ISSN: 0066-4227, 1545-3251. DOI: 10.1146/annurev.mi.03.100149.002103. URL: https://www.annualreviews.org/

doi / 10.1146 / annurev.mi.03.100149.002103 (visited on 01/11/2026).

[73] E. M. Murphy and T. R. Ginn. "Modeling Microbial Processes in Porous Media". In: *Hydrogeology Journal* 8.1 (Mar. 13, 2000), pp. 142–158. ISSN: 1431-2174, 1435-0157. DOI: 10.1007/s100409900043. URL: http://link.springer.com/10.1007/s100409900043 (visited on 04/04/2026).

[74] *National Hydrogen Strategy Update*. 2023. URL: https://www.bundeswirtschaftsministerium.de/Redaktion/EN/Publikationen/Energie/national-hydrogen-strategy-update.html (visited on 03/17/2026).

[75] Nationaler Wasserstoffrat. *Treibhauseinsparungen und der damit verbundene Wasserstoffbedarf in Deutschland*. Ed. by Nationaler Wasserstoffrat. 2023. URL: https://www.wasserstoffrat.de/fileadmin/wasserstoffrat/media/Dokumente/2023/2023-02-01_Grundlagenpapier_H2-Bedarfe_1.pdf.

[76] U. Nations. *Paris Agreement*. Konferenzvereinbarung. Dec. 2015. URL: https://treaties.un.org/pages/ViewDetails.aspx?src=TREATY&mtdsg_no=XXVII-7-d&chapter=27&clang=_en (visited on 03/17/2026).

[77] E. R. Okoroafor, N. Nazari, T. W. Kim, H. Y. Watkins, S. D. Saltzer, and A. R. Kovscek. "Assessment of Hydrogen Storage Potential in Depleted Gas Fields and Power-to-Hydrogen Conversion Efficiency: A Northern California Case Study". In: *International Journal of Hydrogen Energy* 71 (June 19, 2024), pp. 982–998. ISSN: 0360-3199. DOI:

10.1016/j.ijhydene.2024.05.239. URL: https://www.sciencedirect.com/science/article/pii/S0360319924019360 (visited on 04/04/2026).

[78] M. Olivarius, R. Weibel, M. L. Hjuler, L. Kristensen, A. Mathiesen, L. H. Nielsen, and C. Kjøller. "Diagenetic Effects on Porosity–Permeability Relationships in Red Beds of the Lower Triassic Bunter Sandstone Formation in the North German Basin". In: *Sedimentary Geology* 321 (May 2015), pp. 139–153. ISSN: 00370738. DOI: 10.1016/j.sedgeo.2015.03.003. URL: https://linkinghub.elsevier.com/retrieve/pii/S003707381500069X (visited on 11/06/2025).

[79] P. G.
bibinitperiod Optik. *ITO-Beschichtungen Auf Glas*. URL: https://www.pgo-online.com/de/ito.html.

[80] *Organismal Biology*. Apr. 10, 2025. URL: https://organismalbio.biosci.gatech.edu/biodiversity/prokaryotes-bacteria-archaea-2/.

[81] N. Parker, M. Schneegurt, A.-. T. Tu, B. M. Forster, and P. Lister. *Microbiology*. Houston, Texas: OpenStax College, Rice University, 2016. ISBN: 978-1-947172-23-4.

[82] D.-Y. Peng and D. B. Robinson. "A New Two-Constant Equation of State". In: *Industrial & Engineering Chemistry Fundamentals* 15.1 (Feb. 1976), pp. 59–64. ISSN: 0196-4313, 1541-4833. DOI: 10.1021/i160057a011. URL: https://pubs.acs.org/doi/abs/10.1021/i160057a011 (visited on 09/02/2025).

[83] A. Pérez, E. Pérez, S. Dupraz, and J. Bolcich. “Patagonia Wind - Hydrogen Project: Underground Storage and Methanation”. In: . *Zaragoza* (2016).

[84] H. Plaat. “Underground Gas Storage: Why and How”. In: *Geological Society, London, Special Publications* 313.1 (Jan. 2009), pp. 25–37. ISSN: 0305-8719, 2041-4927. DOI: 10.1144/SP313.4. URL: https://www.lyellcollection.org/doi/10.1144/SP313.4 (visited on 01/09/2025).

[85] *Polyetheretherketon (PEEK)*. URL: https://www.kern.de/de/technisches-datenblatt/polyetheretherketon-peek?n=1701_1 (visited on 04/06/2025).

[86] PricewaterhouseCoopers. *Green hydrogen economy - predicted development of tomorrow*. PwC. URL: https://www.pwc.com/gx/en/industries/energy-utilities-resources/green-hydrogen-cost.html (visited on 05/15/2026).

[87] K. Reinicke and C. Fichter. “Measurement strategies to evaluate the integrity of deep wells for CO2 applications”. In: *Underground Storage of CO2 and Energy* 67 (2010).

[88] V. Reitenbach, L. Ganzer, D. Albrecht, and B. Hagemann. “Influence of Added Hydrogen on Underground Gas Storage: A Review of Key Issues”. In: *Environmental Earth Sciences* 73.11 (June 2015), pp. 6927–6937. ISSN: 1866-6280, 1866-6299. DOI: 10.1007/s12665-015-4176-2. URL: http://link.springer.com/10.1007/s12665-015-4176-2 (visited on 10/03/2025).

[89] J. A. Robinson and J. M. Tiedje. “Competition between Sulfate-Reducing and Methanogenic Bacteria for H2 under Resting and Growing Conditions”. In: *Archives*

of Microbiology 137.1 (Jan. 1984), pp. 26–32. ISSN: 0302-8933, 1432-072X. DOI: 10.1007/BF00425803. URL: http://link.springer.com/10.1007/BF00425803 (visited on 04/07/2026).

[90] Schlumberger Energy Glossary. *non-Darcy flow*. URL: https://glossary.slb.com/terms/n/non-darcy_flow.aspx.

[91] P. Schönheit, J. Moll, and R. K. Thauer. "Growth Parameters (K_s, μ_{Max}, Y_s) of Methanobacterium Thermoautotrophicum". In: *Archives of Microbiology* 127.1 (Aug. 1980), pp. 59–65. ISSN: 0302-8933, 1432-072X. DOI: 10.1007/BF00414356. URL: http://link.springer.com/10.1007/BF00414356 (visited on 02/19/2026).

[92] A. Shojaee, S. Ghanbari, G. Wang, and E. Mackay. "Interplay between Microbial Activity and Geochemical Reactions during Underground Hydrogen Storage in a Seawater-Rich Formation". In: *International Journal of Hydrogen Energy* 50 (Jan. 2024), pp. 1529–1541. ISSN: 03603199. DOI: 10.1016/j.ijhydene.2023.10.061. URL: https://linkinghub.elsevier.com/retrieve/pii/S0360319923051273 (visited on 04/07/2026).

[93] A. Soares, A. Edwards, D. An, A. Bagnoud, J. Bradley, E. Barnhart, M. Bomberg, K. Budwill, S. M. Caffrey, M. Fields, J. Gralnick, V. Kadnikov, L. Momper, M. Osburn, A. Mu, J. W. Moreau, D. Moser, L. Purkamo, S. M. Rassner, C. S. Sheik, B. Sherwood Lollar, B. M. Toner, G. Voordouw, K. Wouters, and A. C. Mitchell. "A Global Perspective on Bacterial Diversity in the Terrestrial Deep Subsurface". In: *Microbiology* 169.1 (Jan. 17, 2023). ISSN: 1350-0872, 1465-2080. DOI: 10.1099/mic.0.001172. URL: https://www.microbiologyresearch.org/

content/journal/micro/10.1099/mic.0.001172 (visited on 04/10/2025).

[94] L. I. Stiel and G. Thodos. "The Viscosity of Nonpolar Gases at Normal Pressures". In: *AIChE Journal* 7.4 (Dec. 1961), pp. 611–615. ISSN: 0001-1541, 1547-5905. DOI: 10.1002/aic.690070416. URL: https://aiche.onlinelibrary.wiley.com/doi/10.1002/aic.690070416 (visited on 09/02/2025).

[95] G. Strobel, M. Wirth, B. Hagemann, and L. Ganzer. "Utilization of Microfluidics to Investigate Microbial Activity in Underground Hydrogen Storage". In: *2nd Geoscience & Engineering in Energy Transition Conference*. Online, European Association of Geoscientists & Engineers, 2021, pp. 1–5. DOI: 10.3997/2214-4609.202121039. URL: https://www.earthdoc.org/content/papers/10.3997/2214-4609.202121039 (visited on 02/24/2026).

[96] G. Strobel, B. Hagemann, T. M. Huppertz, and L. Ganzer. "Underground Bio-Methanation: Concept and Potential". In: *Renewable and Sustainable Energy Reviews* 123 (May 2020), p. 109747. ISSN: 13640321. DOI: 10.1016/j.rser.2020.109747. URL: https://linkinghub.elsevier.com/retrieve/pii/S1364032120300411 (visited on 03/19/2026).

[97] G. Strobel, B. Hagemann, C. T. Lüddeke, and L. Ganzer. "Coupled Model for Microbial Growth and Phase Mass Transfer in Pressurized Batch Reactors in the Context of Underground Hydrogen Storage". In: *Frontiers in Microbiology* 14 (Apr. 2023), p. 1150102. ISSN: 1664-302X. DOI: 10.3389/fmicb.2023.1150102. URL: https://www.frontiersin.org/articles/10.3389/fmicb.2023.1150102/full (visited on 02/24/2026).

[98] G. Strobel, J. Zawallich, B. Hagemann, L. Ganzer, and O. Ippisch. “Experimental and Numerical Investigation of Microbial Growth in Two-Phase Saturated Porous Media at the Pore-Scale”. In: *Sustainable Energy & Fuels* 7.16 (2023), pp. 3939–3948. ISSN: 2398-4902. DOI: 10.1039/D3SE00037K. URL: https://xlink.rsc.org/?DOI=D3SE00037K (visited on 02/24/2026).

[99] M. Talukdar, P. Blum, N. Heinemann, and J. Miocic. “Techno-Economic Analysis of Underground Hydrogen Storage in Europe”. In: *iScience* 27.1 (Jan. 2024), p. 108771. ISSN: 2589-0042. DOI: 10.1016/j.isci.2023.108771. URL: https://www.sciencedirect.com/science/article/pii/S2589004223028481 (visited on 03/17/2026).

[100] G. T. Taylor and S. John Pirt. “Nutrition and Factors Limiting the Growth of a Methanogenic Bacterium (Methanobacterium Thermoautotrophicum)”. In: *Archives of Microbiology* 113.1-2 (1977), pp. 17–22. ISSN: 0302-8933, 1432-072X. DOI: 10.1007/BF00428574. URL: http://link.springer.com/10.1007/BF00428574 (visited on 02/23/2026).

[101] M. R. Tek. *Natural Gas Underground Storage: Inventory and Deliverability*. Tulsa, Okla: PennWell Pub, 1996. 433 pp. ISBN: 978-0-87814-614-7.

[102] E. M. Thaysen, S. McMahon, G. J. Strobel, I. B. Butler, B. T. Ngwenya, N. Heinemann, M. Wilkinson, A. Hassanpouryouzband, C. I. McDermott, and K. Edlmann. “Estimating Microbial Growth and Hydrogen Consumption in Hydrogen Storage in Porous Media”. In: *Renewable and Sustainable Energy Reviews* 151 (Nov. 2021), p. 111481. ISSN: 13640321.

DOI: 10.1016/j.rser.2021.111481. URL: https://linkinghub.elsevier.com/retrieve/pii/S1364032121007620 (visited on 03/18/2026).

[103] The Federal Government. *The National Hydrogen Strategy (Nationale Wasserstoffstrategie)*. Ed. by Federal Ministry for Economic Affairs and Energy Public Relations Division. 2020. URL: https://www.bmbf.de/bmbf/de/forschung/energiewende-und-nachhaltiges-wirtschaften/nationale-wasserstoffstrategie/nationale-wasserstoffstrategie_node.html.

[104] P.-M. Trimi, S. Bellas, I. Vakalas, R. Gholami, V. Gaganis, E. Gontikaki, E. Stamatakis, and I. V. Yentekakis. "A Review of Caprock Integrity in Underground Hydrogen Storage Sites: Implication of Wettability, Interfacial Tension, and Diffusion". In: *Hydrogen* 6.4 (Dec. 2025), p. 91. ISSN: 2673-4141. DOI: 10.3390/hydrogen6040091. URL: https://www.mdpi.com/2673-4141/6/4/91 (visited on 05/15/2026).

[105] E. R. Ugarte and S. Salehi. "A Review on Well Integrity Issues for Underground Hydrogen Storage". In: *Journal of Energy Resources Technology* 144.4 (2022). ISSN: 0195-0738. DOI: 10.1115/1.4052626.

[106] United States Department of Labor Occupational Safety and Health Administration. *Hydrogen Sulphide*. URL: https://www.osha.gov/hydrogen-sulfide/hazards.

[107] P. Van Bodegom. "Microbial Maintenance: A Critical Review on Its Quantification". In: *Microbial Ecology* 53.4 (May 2007), pp. 513–523. ISSN: 0095-3628, 1432-184X. DOI: 10.1007/

s00248-006-9049-5. URL: https://link.springer.com/10.1007/s00248-006-9049-5 (visited on 02/23/2026).

[108] Vanessa S. Iorio, Federico Cracolici, Fabio Parrozza, Luigina M. F. Sabatino, Elisabetta Previde Massara, Alberto Consonni, Chiara Tritto, and Michela De Simoni. "Cement to Safeguard the Wells Integrity in Underground Hydrogen Storage: an Experimental Investigation". In: *Chemical Engineering Transactions* 96 (2022), pp. 307–312. ISSN: 2283-9216. DOI: 10.3303/CET2296052. URL: https://www.cetjournal.it/index.php/cet/article/view/CET2296052.

[109] J. Wang, Q. Zhang, Z. Song, X. Liu, X. Wang, and Y. Zhang. "Microstructural Variations and Damage Evolvement of Salt Rock under Cyclic Loading". In: *International Journal of Rock Mechanics and Mining Sciences* 152 (Apr. 1, 2022), p. 105078. ISSN: 1365-1609. DOI: 10.1016/j.ijrmms.2022.105078. URL: https://www.sciencedirect.com/science/article/pii/S1365160922000466 (visited on 05/15/2026).

[110] L. Yarborough and K. Hall. "How to Solve Equation of State of Z-factors". In: *Oil and Gas Journal* 72.7 (1974), pp. 86–88.

[111] J. Zhou, X. Qiao, R. Wang, X. Yin, J. Cao, B. Cao, Y. Lei, K. Tian, Z. Zhao, and B. Zhugeng. "Effective Reservoir Development Model of Tight Sandstone Gas in Shanxi Formation of Yan'an Gas Field, Ordos Basin, China". In: *Journal of Natural Gas Geoscience* 7.2 (Apr. 2022), pp. 73–84. ISSN: 2468256X. DOI: 10.1016/j.jnggs.2022.04.003. URL: https://linkinghub.elsevier.com/retrieve/pii/S2468256X22000165 (visited on 11/06/2025).

[112] D. Zivar, S. Kumar, and J. Foroozesh. “Underground Hydrogen Storage: A Comprehensive Review”. In: *International Journal of Hydrogen Energy* 46.45 (July 2021), pp. 23436–23462. ISSN: 03603199. DOI: 10.1016/j.ijhydene.2020.08.138. URL: https://linkinghub.elsevier.com/retrieve/pii/S0360319920331426 (visited on 10/03/2025).

Appendix

Appendix A.1: Sketch of the micromodel heating device, components and connections

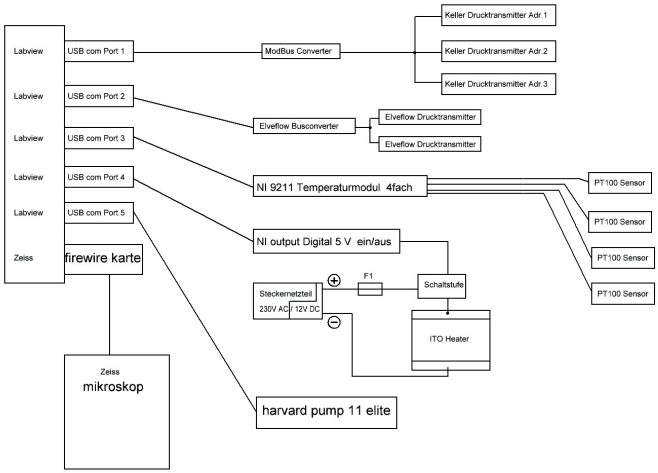

Figure A.1: Setup of the heating device, the used components and the used component-computer communication ports (COM)

Appendix A.2: LabView image of the executed script to monitor and save experimental data

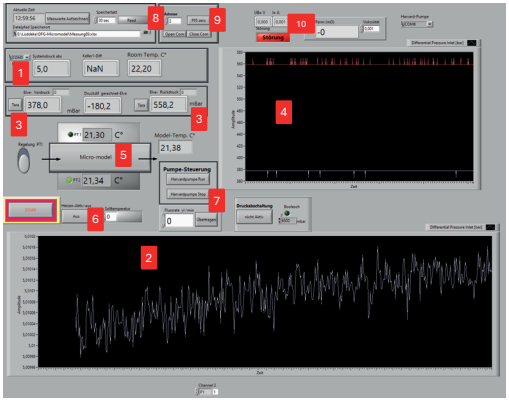

1. Measured backpressure (bar)
2. Measured backpressure (graphical depiction)
3. Elveflow in- and outlet pressure (mbar)
4. Inlet (red) and outlet (white) pressure
5. Measured ITO-plate temperature above and below the microchip (°C)
6. Heating regulator with temperature input
7. Harvard pump digital control panel
8. Data acquisition file path and reading pattern
9. Available COM-ports and respective address
10. Voltage, electricity amplitude and malfunction indicator

Figure A.2: Digital interface of the LabView control panel to insert and control temperature, observe dynamic parameters and to record them into a specific file